2013

Rapid assessment of paint coatings by micro and nano indentation methods

Siu Wah Wai
University of Wollongong

2013

Rapid assessment of paint coatings by micro and nano indentation methods

Siu Wah Wai
University of Wollongong

School of Mechanical, Materials and Mechatronic Engineering

Rapid Assessment of Paint Coatings by Micro and Nano Indentation Methods

Siu Wah Wai

"This thesis is presented as part of the requirements for the award of the Degree of Philosophy of the University of Wollongong"

April 2013

ABSTRACT

Paint coatings/films having pigments/filler particles, in general, are of technological importance because of their wide usage. Traditional quality control testing methods used in industry, such as tensile tests on bulk paint samples, and quick tests such as pencil scratch test, often could not predict coating performance during usage. Coating performance includes strength of adherence, scratch/mar resistance, erosion resistance, formability, colour fastness and gloss retention. Of particular interest in this thesis, is the determination of the elastic modulus of the coatings, since it can be linked to the cross-linking density and hence to the performance of the paint. The best way to evaluate performance are laboratory simulation tests and field exposure tests, but these tests often take weeks or years (in the latter case) to generate meaningful results, thus are not suitable for quality control (QC) purposes. It is therefore imperative to develop an improved quality control tool for quick assessment of pigmented paint coatings suitable for use in the industrial environment. Unlike unpigmented paint coatings, such as automotive top coats, pigmented coats have an inherent roughness imparted by the colour pigments and filler particles which makes determination of the paint matrix by indentation methods difficult. Three-body abrasion, caused by the dislodgment of these hard particles, also adds to the difficulties of interpreting scratch test results.

The relationship between crosslink density in paint matrix and mechanical properties, such as ductility, is known [1], and can be correlated to scratch resistance. However, such correlation was difficult to establish in pigmented paint coatings as dislodgement of pigments during scratch tests sometimes led to accelerated wear.

Indentation testing would yield information on paint properties, such as elastic modulus and hardness, without causing the dislodgement of pigments. Each indentation test typically takes a few minutes, making it an ideal candidate as a rapid quality control tool. The major drawback in using indentation techniques on soft, compliant materials such as polymers which make up the paint matrix are the time-dependent response (creep at fixed load or stress relaxation on fixed displacement), leading to steeper and even negative unloading slopes and hence inaccurate modulus values.

The literature review briefly covers some of the commonly used testing methods employed in industry for polymer coatings. Micro- and nano-indentation methods for the determination of elastic modulus are covered in detail. The effect of creep pertaining to indentation testing, and the treatment thereof, is also reviewed. The experimental work firstly examined the applicability of commercial micro-indentation equipment as QC tools. The results showed that these instruments could qualitatively differentiate the elastic modulus between paint coatings having different degrees of curing (hence differing crosslink densities and resultant mechanical properties), as well as different pigment/filler types and contents. However, creep affected the calculated values of the elastic modulus. Mechanical models using springs and dashpots to estimate elastic modulus values from the creep response were investigated, as were analytical methods to nullify the effect of creep in the unloading response. From this work it was proposed that the Boltzmann superposition principle (where strain response to a complex stress history for a linear viscoelastic material resulting from a complex loading history, is the algebraic sum of the strains due to each individual step in load) be used to extrapolate and then

‘subtract’ the creep displacement response during unloading to yield a more accurate value for the elastic modulus. This contribution provides the groundwork for possible future development of a rapid QC tool for industrial use.

ACKNOWLEDGEMENTS

I thank Bluescope Steel for the scholarship funding and for the use of their facilities for sample preparations, as well as for their technical input, in particular, I would like to thank Dr. Evan Evans for supervising this project.

Thanks are also due to the Australian government for the Australian Post-doctorate Research (Industrial) scholarship awarded towards this project.

I especially thank my family as well as my colleagues and friends at the University of Wollongong for all their support and encouragement. In particular, a special thanks to my supervisors Prof. Geoff Spinks and Prof. Hugh Brown.

TABLE OF CONTENTS

LIST OF FIGURES

LIST OF TABLES

LIST OF SYMBOLS AND ACRONYMS

List of acronyms

AFM	Atomic force microscope
DMA	Dynamic mechanical analysis
DSI	Depth sensing indentation
MMR	Micro mar resistance
O&P	Oliver and Pharr
JKR	Johnson, Kendall and Roberts
PCM	Pre-painted coil material
PZT	Piezo transducer
QC	Quality control
SEM	Scanning electron microscopy
SPM	Scanning probe microscopy
UMIS	Ultra-micro indentation system

List of Symbols

a	Radius of contact circle	ε	Geometric constant (O&P)
A	Contact area	v	Poissons ratio
E^*	Reduced elastic modulus		
E'	Storage modulus		
E''	Loss modulus		
G	Complex shear modulus		
h	Vertical displacement of indenter		
K	Force constant in Hooke's law		
k	Cantilever stiffness		
P	Vertical indenter load		
S	Slope of the unloading P-h curve		
T	temperature		
t	time		
α	Opening angle of indenter tip		
δ	Indenter depth (Hertzian, elastic)		

1 INTRODUCTION

Paint coatings having pigments/filler particles, in general, are of technological importance because of their wide usage. Mechanical properties, such as ductility and elastic modulus can be directly correlated to crosslink density of the paint coatings. Crosslink density of the paint coatings can in turn be related to the degree of cure which is dependent on production parameters. Thus elastic modulus can be used in QC to predict unacceptable variations in the performance of production batches, in terms of scratch/mar resistance, erosion resistance and formability. Currently in industry, accurate and rapid quantitative methods for measuring the mechanical properties of pigmented paint coatings do not exist. Field exposure tests may take several months to yield meaningful results while quick laboratory tests, such as the pencil scratch test, are empirical in nature and operator sensitive. The development of different types of instrumented scratch tests has removed the problem of operator sensitivity. These machines attempt to simulate forming and handling of pre-painted metal sheets and their results show that scratch resistance increased with increasing ductility of the coating, which also correlated to a decrease in crosslink density in the polyester paint matrix [1]. However, the results on pigmented paint coatings were ambiguous as dislodgement of pigment particles sometimes contributed to accelerated wear by means of three body abrasion [1]. These results are significant to the current research work, since a pre-painted metal sheet is essentially a paint coating on a metal substrate, and since the coatings in the current work were made from crosslinked polyester paints as well. These results indicated that scratch tests are often not sufficiently sensitive to isolate production problems of pigmented paint coatings that might result in inferior performance. In addition, film properties cannot

be derived directly from those of the bulk material, as constraints imposed by the substrate play an important role in the observed properties [2]. It is therefore imperative to develop a quality control (QC) tool for quick assessment of pigmented paint films in the industrial environment. It is preferable that the method provide accurate information on the basic mechanical properties, such as elastic modulus, rather than indirect properties, such as scratch resistance. Indentation testing would allow the determination of the elastic modulus, thus revealing information on degrees of curing in paint systems, without causing dislodgement of pigments. Hence it would be a suitable candidate for a rapid non-destructive means for modulus determination.

Recently depth sensing indentation techniques were used as a quick online screening tool, to speed up the development of new formulations for polyurethane elastomers [3]. In this work the preparation and testing of 40 samples could be completed in a few hours. In comparison the preparation of conventional tensile specimens was found to be a bottleneck in the process, although the elastic modulus values obtained were more accurate. The inaccuracies in the determination of the elastic modulus values were largely due to creep during unloading, as well as due to material pile up around the indentation. These problems are described in more detail below. Despite the inaccuracies, it was found that the same trends in modulus values existed for the different formulations tested using both conventional testing and indentation techniques. This finding further illustrates the potential of indentation techniques as a rapid, non-destructive QC tool, capable of determining elastic modulus values. However, the accurate determination of elastic modulus requires that the ‘creep’ response during unloading can be nullified, and accurate determination of contact area could be established.

Depth-sensing indentation (DSI) techniques, or indentation tests, in which the load and displacement are recorded during contact of an indenting probe onto a material surface, are used routinely to measure mechanical properties in hard materials. From the load and displacement data, load-displacement traces showing elastic-plastic regimes are generated. Existing data analysis methods are used to deconvolute elastic-plastic load-displacement traces to obtain values or ratios of material modulus, *E*, and hardness, *H*. These methods will be covered in more detail in section 2.4. Commercial instruments exists which makes use of these analysis methods for micro- and nano-indentations. Each indentation test would only take a few minutes, thus making these techniques attractive for testing the mechanical properties of stiff and hard materials, often in the form of thin films [3-10]. The major drawback in using these techniques on soft, compliant materials such as polymers and biological materials is the time-dependent response (creep at fixed load or stress relaxation on fixed displacement), leading to inaccuracies in the displacement data since the creep component is significant. This in turn will lead to inaccurate calculations of the elastic modulus.

The broad objective of this thesis is to investigate experimental and analysis methods to allow for the accurate determination of the elastic modulus of polymers and pigmented paint coating using indentation methods. The literature review briefly covers some of the commonly used testing methods employed in industry for polymer coatings. Micro- and nano-indentation methods for the determination of elastic modulus are covered in detail. The effect of creep pertaining to indentation testing, and the treatment thereof, is also reviewed. These background studies

provide the framework against which the thesis aims can be specified. The literature results will also be used in comparison with the experimental findings of this thesis.

The aim of the experimental work is to firstly examine the applicability of commercial depth sensing indentation (DSI) equipment as a QC tool in providing elastic modulus values of different types of paint coatings. Experimental work on micro-indentation testing was carried out on a commercially available system, the UMIS-2000, using a pointed Berkovich as well as spherical indenters. Polystyrene was used as reference sample, to examine the repeatability of the technique, as well as to examine the effect of surface roughness. The latter is important, as the surfaces of the industrial paint coatings being examined would be inherently rough, in the micro-meter scale. The feasibility of using a commercial atomic force microscope (AFM) and a home-built 'force-rig' for the nano-indentation work was also examined. It is expected that micro-indentations would only yield average values, as the indentations would occur on both the pigment particles as well as in the paint matrix. In addition, surface roughness of the paint layer would result in scatter in the resultant materials property values. Nano-indentations, however, may have the advantage of selectively isolating and probing the different components in the paint layer; thereby the individual properties of the various components could be studied. Also, the effect of surface roughness might be negligible at the nanometre scale. High-temperature indentation work was carried out on bulk polystyrene using a commercial dynamic mechanical analyzer (DMA), to examine the applicability of the indentation technique at temperatures close to the glass transition temperature (T_g).

Existing mechanical models for creep using springs and dashpots which would yield values for elastic modulus were evaluated. Analytical methods such as those used by Feng and Ngan [11, 12] to further remove the effect of creep in the unloading response, was also investigated. The Boltzmann superposition principle (where strain response to a complex stress history for a linear viscoelastic material resulting from a complex loading history, is the algebraic sum of the strains due to each individual step in load) was used to extrapolate and 'subtract' the creep displacement response during unloading to yield a more accurate value for the elastic modulus. This work lays the groundwork for possible future development of a rapid QC tool for industrial use.

2 LITERATURE REVIEW

2. 1 Characteristics of polymeric materials

Polymers can be characterised by their mechanical properties, which include the deformation of the polymers or their surfaces, the resistance to deformation, and the ultimate failure, all under static or dynamic loads. Deformations can be caused by drawing, shearing, compression, bending, and/or torsion; they may be reversible or irreversible. Reversible deformations of materials are due to the presence of elasticity. Irreversible deformations are caused by viscous flow, plasticity, phase transformations, craze formations, cracking, viscoelasticity, viscoplasticity, etc. These terms are briefly defined below.

Elasticity is a material response in which the material strains/deforms instantaneously upon loading but returns to its original state just as quickly when the load/stress is removed. Viscous flow occurs when a material exhibits fluid like characteristics under stress and its rate of deformation increases with increasing applied stress. There is also a characteristic time delay between the applied maximum stress and the resultant maximum strain. Under a sufficiently large stress beyond its yield stress, a material may undergo permanent and time independent plastic deformation. Temperature (and sometimes pressure) change may cause phase transformations in a material. The associated shape/volume change brought about by the new phase causes stress and deformation within the material. Thermal or cyclic stresses on the surface of a brittle material such as ceramic may cause fine craze cracks on the surface. Beyond its yield point, further bond breaking in a materials internal structure under higher stresses may result in micro-cracking and finally visible cracks and fracture, especially in brittle materials. Time delayed elasticity and plasticity (when a material exhibits fluid like or viscous responses) are termed viscoelasticity and viscoplasticity, respectively.

For clarity, it should be noted that depth-sensing indentations, due to the small scale indentations involved (often in nanometres scales), are commonly referred to as nano-indentation in the literature, of which the bulk of the work is carried out on metals and ceramics. However, for compliant materials such as polymers, the indentations can reach micro-meters and in this work, only the work carried out using AFM (atomic force microscope) type equipment are referred to as nano-indentation. In addition, the term ‘creep’ in nano-indentation is commonly used to

describe the delayed response to an applied stress or strain and usually encompasses both viscoelastic and viscoplastic deformation.

Polymers begin to exhibit viscous flow when stressed at temperatures below but close to their T_g. The viscous behaviour is also amplified as stress rate decreases. In general, the faster the stress rate and the lower the temperature, the larger will be the elastic response and the smaller the viscous component. On the other hand, viscoelasticity is amplified as temperature increases and the stress rate is decreased.

Mechanical properties such as tensile strength, impact strength, hardness and elastic modulus, as well as other properties such as erosion, scratch and mar resistance, formability, UV resistance and solvent resistance can be evaluated for polymeric materials. In addition, viscous properties such as loss modulus and tan delta are commonly evaluated. In section 2.3, general testing methods applicable to paint coatings are briefly described.

2. 2 Paint coating systems

Paint coatings are formulated according to their functional and decorative requirements. Critical properties of most coatings relate to their ability to withstand use without damage. These properties include mechanical integrity, exterior durability, adhesion, and corrosion protection. For example, the coating on the outside of an automobile should have good abrasion resistance to withstand scratches and be sufficiently tough to withstand rupture when hit by flying gravel. It must also have good exterior durability so that it does not discolour or embrittle too rapidly from exposure to sunlight. A more relevant example is paint films on pre-painted

steel sheets or pre-painted coil metals (PCMs) or coil-coating paints. PCMs are used in many fields such as building materials (panels and guttering), as well as home appliances. For these applications, abrasion resistance is important. Also, as PCMs are formed into corrugated (and other) profiles after painting, formability is another crucial requirement. Generally, forming modes are bending and deep drawing, and cracks as well as delaminations arising from these forming processes are of serious industrial concern. Since formability is optimal just below T_g, but abrasion resistance decreases with increasing temperature, a balance between these properties is achieved by formulating the coil-coating paints such that the T_g is just above ambient.

Polymeric paint coatings typically consist of a matrix resin or binder, with dispersed pigments for colour, inert/flatting pigments to control gloss, as well as other additives to achieve specific characteristics or properties, such as to improve flow or reduced viscosity.

The typical polyester used in the matrix of the paint coatings is amorphous, branched and cross-linkable, with a weight average molecular weight (M_w) of 2000-4000 [13]. It is made from a mixture of diols, triols, and diacids. The choice of polyester components is usually made according to the desired properties of the final coating. In general, the ratio of aromatic to aliphatic diacids is the principal factor controlling the glass transition temperature (T_g) of the final coating. T_g will also be affected by polyol structure. The use of predominately aliphatic diacids leads to soft, flexible coatings with low damage resistance. On the other hand, increasing the amount of aromatic diacids improves damage resistance at the expense of flexibility [13]. Also,

the ratio diol/triol controls the molecular weight distribution, and ultimately affects the potential crosslink density after cure, thus affecting T_g and elastic modulus values [14].

Finally, the incorporation of pigments and flattening agents also affects the property of the coating, mainly by acting as stiffeners, but also by imparting its own properties into the coating. Pigments are insoluble, fine particle size materials used to provide colour, to hide substrates, to modify the application and/or the performance properties of the coating, and/or to reduce costs. In general terms, pigments are divided into four broad classes: white, colour, inert, and functional pigments. In general, a large fraction of all coatings contain a white pigment. White pigments are used not only in white coatings but also in other pigmented coatings to give a lighter colour than would be obtained using colour pigments alone. Furthermore, many colour pigments give transparent films, and the white pigment provides a major part of the hiding power of the coating, due to its high scattering coefficient. The most widely used white pigment is titanium oxide. With the exception of black pigments, which are mainly carbon blacks (carbon particles imparting a black colour), the colour pigments can be either organic or inorganic. Typical examples of yellow and red pigments are the various types of iron oxides, while ferric ammonium ferrocyanide is an example of a blue or green pigment. Inert pigments and flatting pigments are used primarily to adjust the rheological properties of the fluid coatings, as well as the gloss and mechanical properties of the coating film [14].

2. 3 Paint testing

Although extensive testing is employed in the industry to ensure adequate mechanical properties of paint coatings, these tests are often empirical and qualitative in nature, as they are operator sensitive. Traditional methods such as tensile testing are sometimes employed on bulk paint samples made by casting or from free standing paint films, but the results obtained often do not reflect the properties of paint coatings due to differences in curing that may occur during the preparation of the free-standing film (it is often not possible to detach the paint from the substrate without damage). In addition, the preparation of thin films is difficult and imperfections are common leading to premature failure and large errors in the test results. Pigments in free standing films can sometimes act as defects, causing cracking and low tensile strengths.

2.3.1 Testing of free standing films or bulk polymer samples

2.3.1.1 Tensile testing

Tensile testing is commonly carried out using commercially available tensile testers. Essentially, a sample is mounted between two jaws which are then moved apart at a specific rate, thus pulling the sample at a constant strain rate. The yield strength, tensile strength and elongation can be obtained. Elastic modulus can also be obtained from the slope of the initial straight portion of the stress vs. strain curve. On a smaller scale when thin films are used, a dynamic mechanical analyser (DMA) can be used.

Due to the viscoelastic nature of polymers, deformation is very dependent on temperature and the time over which a stress is applied. If the rate of stress application is rapid, the material response can be primarily elastic. In this case the viscous component is suppressed. On the other hand, if the stress rate is low, the viscous component of the response can be amplified and the elastic response will be relatively small. Similarly, if the temperature is low, the response can be mainly elastic in nature, whereas at a higher temperature, the viscous response will be proportionally greater.

2.3.1.2 Dynamic mechanical analysis

Dynamic mechanical analysis (DMA) has the advantage over stress-strain curves that the elastic and viscous components of a modulus can be separated, by applying an oscillating strain (usually a sine wave) at a specific frequency. The disadvantage is that only small-strain properties are measured. No information is provided regarding yield or fracture. In the DMA test, the stress and the phase angle difference between applied strain and resultant measured stress are determined. Small strains are used to prevent plastic or permanent deformation. For an ideal elastic material, there is no phase shift since there is an instantaneous stress response to the applied strain. For a Newtonian fluid, there would be a phase shift of 90^{o}. Viscoelastic materials, on the other hand, tend to show an intermediate response. The phase shift, δ, along with the maximum applied strain, ε^{0}, and the maximum measured stress, σ^{o}, are used to calculate the dynamic properties.

The *storage* or *elastic modulus*, which is a measure of the elastic response, is given by:

$$E^{'} = \left(\frac{\sigma^0}{\varepsilon^0}\right)\cos\delta \qquad (2.1)$$

The *Loss modulus* is a measure of the viscous response, and is given by:

$$E^{''} = \left(\frac{\sigma^0}{\varepsilon^0}\right)\sin\delta \qquad (2.2)$$

The ratio $\left(E^{''}/E^{'}\right)$ is called the *loss tangent*, commonly referred to as *tan delta*, since

$$\frac{E^{'}}{E^{''}} = \frac{\sin\delta}{\cos\delta} = \tan\delta$$

Commercial DMAs can operate in different modes: tensile, compression and flexural (three-point bend, single cantilever and dual cantilever), over several decades of frequencies, and with temperature control. The most typical experiment involves a temperature ramp such that the T_g can be identified, as shown in Figure 2.1 from a sudden decrease in $E^{'}$ or $E^{''}$ and by a peak in tan δ.

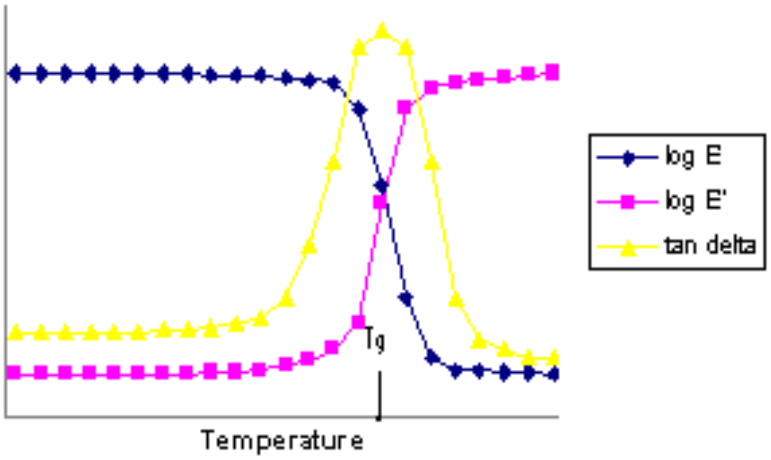

Figure 2.1: Typical experimental plot showing changes in $E^{'}$, $E^{''}$ and tan delta with temperature. T_g is reflected by the sudden change in properties.

2.3.2 Tests carried out on paint coatings

There are three broad classes of paint tests: field exposure tests, laboratory simulation tests, and a broad category of empirical tests [15]. Each of these tests is summarised below.

2.3.2.1 Field exposure tests

The best way to evaluate the performance of a coating is in actual use. However, as feedback may take many years to obtain, the next best method is to perform smaller scale accelerated field performance tests. For example, automobiles painted with new coating systems are driven through extreme road and weather conditions and compared to the performance of a known control.

2.3.2.2 Laboratory simulation tests

Under well simulated conditions to mimic actual use, and through thorough validation procedures, laboratory tests can be useful in predicting specific performances of paint coatings. For example, exposures to UV radiation in specially designed UV cabinets are commonly used to evaluate UV degradation under normal exposure to sunlight. The test samples are compared to known standards that cover the whole range from poor to excellent performance.

Generally, the sample preparation and testing times for the above two categories of testing are too long to be useful for checking whether production batches of an established coating are equal to the standard. Quality control is best achieved by rapid (preferably immediate) testing to allow feedback control of the manufacturing process. Hence, faster empirical tests are employed for industrial quality control to check for acceptance of daily production batches.

2.3.2.3 Empirical tests

Besides their use in quality control, empirical tests are often used in specifications for new coating systems. The most commonly used empirical tests are briefly described below [16]:

2.3.2.3.1 Pencil hardness test

The most widely used hardness test for thin paint coatings is the pencil test, conducted to ASTM standard D3363-05 [17]. Pencils with hardness varying from 6B

(softest) to 9H (hardest) are available. The pencil "lead" in the pencil is squared off by rubbing perpendicularly on abrasive paper. For the test, the pencil is held at 45^{o} angle to the test sample and pushed forward with pressure just below that required to break the lead. The hardness is reported as the grade of pencil that does not create any marring of the surface. For quality control purposes, test samples must pass the test for a specific grade of lead. The reproducibility of the test would depend on the experience of the tester and is thus subjective.

2.3.2.3.2 Coin scratch test

Similar to the pencil hardness test, a scratch is made and visually assessed for coating adhesion. Again, it is subjective and qualitative.

2.3.2.3.3 Other scratch tests from literature

Scratch test is especially important in the automotive industry where scratching and marring of the top coat can affect gloss and result in 'fading' of the paintwork. For example, dust and dirt particles trapped in automated car wash brushes can introduce fine scratches a few microns deep and around ten microns wide, that are visible to the naked eye. The fine-scale scratching is known as marring. Attempts were made to simulate and qualify or quantify scratching and marring in the laboratory [1, 18-27]. Shen et al. [20] characterised mar/scratch resistance of a variety of coatings using a nano-indenter and a scanning probe microscope. In their work the different responses of coatings to marring stress, and the critical forces for forming rough trough, cracking, delamination and chipping were examined. Micro-mar resistance (MMR) was defined as the normal force applied in the scratching test divided by the cross sectional area of the resultant trough. They further introduced a quantitative

index using the damage categories (viz. mar, trough, cracking, delamination, chipping) and the frequencies of occurrence in each category. Gregorovich and co-workers [21] attempted to simulate scratching and marring of automotive top coats using the commercial Taber Abraser, and a modified standard test for plastics [28]. In a typical wear test using the Taber Abraser, the sample is mounted to a rotating turntable and is subjected to a rub-wear action of the two abrading wheels attached to an arm with adjustable weights (typically 250g, 500g and 1000g). As the turntable rotates, it in turn causes the abrading wheels to turn, thus resulting in sliding rotation. The test produces abrasion marks that form a pattern of cross arcs over a circular ring approximately 30cm^2 in area and these cover all angles on the material surface. The gloss retention of the materials tested was then ranked in the scale from 1 to 100. The results were compared to the average results from 'field' tests in a car wash using the ranking (in a scale of 1 to 4) from 8 observers. They found good agreement in the trend for the coatings studied.

Attempts were also made to relate scratch resistance to material properties. Pelletier 2008 [29] attempted to correlate viscoelastic-plastic properties of polymer films with scratch resistance using depth-sensing instruments. By measuring the surface before and after performing the scratch test, under very low loads to minimize further plastic deformation, true scratch profile including material pile-up height and angle of elastic recovery could be determined, thus the true contact height and contact area could be determined. They further proposed a methodology to determine the viscoplastic index and the free volume (related to the space between molecules). They were able to show correlation of these parameters to the fracture resistance of polymers, verified by indentation scratch test results for three polymers tested.

Bertram-Lambotte and co-workers [25] measured indentation hardness vs. strain rate at different temperatures and constructed a time-temperature superposition curve. From this curve the activation energy of viscoplastic process could be determined. These values were close to the secondary β transition temperature, usually attributed to local molecular motion, such as rotation of side groups or limited rotations with the chain backbone. Their results show that mar resistance was dependent on this transition temperature, in comparison to the main mechanical relaxation (α transition) temperature. Jardret et al. [30] made use of three- dimensional (3-D) topographic relief to determine actual contact depth and contact area, taking into account pile up phenomenon for a number of metallic materials and a acetate polymer. By superimposing the Berkovich indenter profile and the scratch groove profile, the elastic recovery could be determined. Thus plastic deformation could also be determined. They found that the proportion of plastic deformation increased (compared to elastic deformation) when the ratio of elastic modulus to hardness increased. Lange et al. [1, 24] were able to relate scratch resistance of pre-painted steel sheets to crosslink density, although the effect of pigment and wax additions were more ambiguous as they were dependent on the type of tests.

2.3.2.3.4 Impact test

Impact tests evaluate the ability of the coating to withstand extension without cracking when the deformation is applied suddenly or rapidly. A weight is dropped down a guide tube onto a hemispherical indenter that rests on the coated panel. An opening, opposite the indenter in the base support on which the sample rests, permits deformation of the panel. If the coated side is up such that the indenter directly hits the coating, the test is called a direct impact test. It the coating is facing downwards,

the test is called a reverse impact test. The weight is dropped from greater and greater heights until the coating cracks. The results are often reported as the distance the weight falls times its weight, or as an equivalent potential energy, in Joules. Generally, reverse impact tests are more severe as the coating is subjected to a tensile stress rather than a compressive stress in the case of the direct impact test. Since the impact energy is absorbed by the substrate as well, this test is only useful in comparing similar samples with the same substrate; and is therefore more suitable as a quality control tool. In this case, the test samples are expected to pass a certain standard of Joules. Again, paint lift off can be checked to assess adhesion properties.

2.3.2.3.5 T bend test

This test is widely used to check formability in coil coatings. A strip of coated metal is bent back flat against itself with the coating side out. If there is no visual crack along the edge of the bend, the result is reported as zero T. The zero means that there is no additional layer of metal inside the bend. If the coating cracks, the strip is bent again back on itself, such that the radius of curvature of the bend is increased, having an extra layer of strip inside the bend. Repeated bends back over the original bend are made until the coating does not crack, since the radius of curvature increases further with each additional bend. The results are reported as 1T, 2T, etc. Paint lift-off can also be checked by taping the cracked region. The tape is then peeled off and the tape surface examined under an optical microscope. Paint lift off can be used as a quick test for coating adhesion.

2.3.2.3.6 MEK double rub test

This test is employed to assess solvent resistance. Although solvent resistance is not a mechanical property, it is important since solvent resistance is related to the degree of cross-linking that will ultimately affect its mechanical properties and performance. The most common test is the methyl-ethyl ketone (MEK) double rub test. In general this test is sensitive to detect coatings having low cross-link densities, and can therefore detect production batches resulting from inadequate curing conditions.

Solvent soaked material such as cotton wool is used to repeatedly rub the paint surface in a forward and backwards motion. The result is reported as the number of double rubs that the coating withstands before rubbing off. For quality control purposes, a sample will be required to pass a specified number of double rub cycles. This test can be performed manually or by means of a mechanical tester using a fixed load.

2. 4 Micro-indentation

2.4.1 Historical background

Conventional hardness testing involves indenting the sample (with known force and shape of indenter) and measuring the size of the residual indentation with an optical microscope. The major drawback in measuring mechanical properties of materials on submicron scale is the minute size of the resultant impression which cannot be measured accurately using conventional optical techniques. Indeed, advances in the past decade were only made possible by the development of instruments capable of

continuously recording depth and displacement data during indentation. If plastic deformation occurs due to the indentation process, then a residual impression will result, and the material hardness (and modulus) values will depend on the size of the residual impression. An indirect method to determine the contact area at full load would be to make use of the penetration force/displacement data and the known geometry of the indenter. From this, the mean contact pressure and hence hardness can be determined, although the hardness in this instance is determined from the contact area size. The assumption is that the projected area of the contact patch is equivalent to the size of the residual impression, since elastic recovery is predominately in the direction of unloading.

The first satisfactory analysis of stresses at the contact of two elastic solids was provided by Hertz in 1882 [31]. In addition to static loading he also investigated the quasi-static impacts of spheres. He also attempted to apply the theory to define the hardness of a solid in terms of contact pressure to initiate plastic yield in the solid by pressing a harder body in contact with it. This definition proved unsatisfactory due to the difficulty in detecting the point of first yield under the action of contact stress. A satisfactory theory was only found after the development of the theory of plasticity. Hertz simplified his model by treating each body as an elastic half-space loaded over a small elliptical region. This simplification can only be satisfied if the significant dimensions of the contact area are small compared with

- the dimensions of each body
- the relative radii of curvature of the surfaces.

In general, the model is suitable for any solids under low stress conditions (low load, large indenter) such that the deformation is purely elastic.

Denoting the significant dimensions of the contact area radius by a, the relative radius of curvature by R, the significant radii of each body by R_1 and R_2 and the significant dimensions of the bodies both laterally and in depth by I, the basic assumptions made by the Hertz theory can be summarised as:

- The surfaces are continuous and non conforming: a<<R;
- The strains are small: a<<R;
- Each solid can be considered as an elastic half-space: a<<$R_{1,2}$, a<<I;
- The surfaces are frictionless.

For a solid of revolution,

$$P_0 = \frac{3P}{2\pi a^2} = \left(\frac{6PE^{*2}}{\pi^3 R^2} \right)^{1/3} \tag{2.3}$$

where P_0 = maximum pressure;

P = total vertical load.

Taking into account of the interaction of a non-rigid indenter capable of deforming elastically under load, the reduced modulus E^*, is defined as

$$\frac{1}{E^*} = \frac{1-\nu_m^2}{E_m} + \frac{1-\nu_i^2}{E_i} \tag{2.4}$$

where ν_m and E_m are the Poisson's ratio and the elastic modulus for the material being tested; and ν_i and E_i are the Poisson's ratio and the elastic modulus for the indenter, respectively.

For a rigid indenter indenting onto an elastic surface (foundation model):

$$P = \frac{2}{3}\left(\frac{Ea}{h}\right)\frac{a^2}{R} \qquad (2.5)$$

where *h* is the vertical elastic displacement of the indenter into the material due to load *P*.

Note that for the above the foundation is modelled as a ‘mattress’ rather than an elastic half space; and there are no interactions (shear between adjacent elements) between the springs [31].

Upon unloading, some degree of elastic recovery occurs. An analysis of the initial portion of this elastic unloading response gives an estimate of the elastic modulus of the indented material. The general relationships for load and displacement for any rigid punch that can be described as a solid of revolution of a smooth function, was first derived by Sneddon and cited by Oliver & Pharr [32] as

$$P = nh^m \qquad (2.6)$$

where P is the indenter load, h is the elastic displacement of the indenter, and n and m are constants. Values of m for some common punch geometries are m = 1 for flat cylinder, m = 2 for cones, m = 1.5 for spheres in the limit of small displacements, m =1.5 for paraboloids of revolution [32, 33, 34].

Specifically, for the unloading curve (unloading portion of the load-displacement curve), the above equation can be rewritten as

$$P = n(h - h_f)^m \qquad (2.7)$$

where h_f is the final displacement after complete unloading,

Experimental observations showed that the value of m is slightly material dependent. Pharr and Bolshakov [35] found that the m value for a Berkovich indenter ranged from 1.2 to 1.6 for a range of metals and glasses, while Saki [36] indenting a number of metals and ceramics using a Vickers indenter, found the m values to be closer to 2.

Doerner and Nix [37] developed a comprehensive approach based on the observation that the elastic behaviour of the indentation contact is similar to that of a flat punch during the initial stages of unloading. That is, the area of contact remains constant, as the indenter is unloaded. This was justified by their experimental observations on a range of materials. For metals, constant contact area was observed over most of the unloading range. Constant contact area would imply linear unloading, that is, the relationship between load and displacement would be linearly proportional. For materials with higher ratios of hardness to elastic modulus, more curvature was observed in the unloading curve. However, even for Silicon where large elastic recoveries occurred, linear unloading was observed for the initial 1/3 of the unloading curve. These observations suggest that, for some materials at least, the initial portions of the unloading curves could be described by the equation for the flat punch (under conditions of frictionless loading/unloading for which contact area A remains constant), as follows:

$$\frac{dP}{dh} = S = \alpha E^* \sqrt{A} \tag{2.8}$$

where S is the unloading contact stiffness, α is a constant and A is the projected area of the resultant impression and E^* is the reduced modulus, as defined above in equation (2.4).

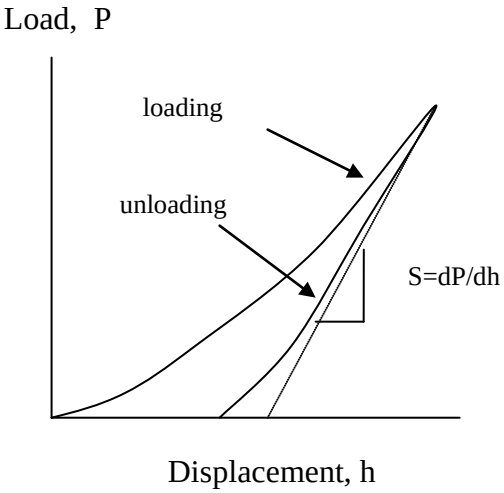

Figure 2.2: Schematic illustration of indentation load-displacement data.

Doerner and Nix further proposed that the contact area can be independently determined by extrapolating the initial linear portion of the unloading curve to zero load (Figure 2.2) and using the extrapolated depth with the indenter shape function to determine the contact area, A. Thus E^* can be determined. In addition, hardness can be determined by the simple relationship

$$H = P_{max} / A \qquad (2.9)$$

where P_{max} is the peak load.

The one disturbing feature of the Doerner-Nix method is the assumption of linearity of the unloading curve. Oliver and Pharr [32] and Pharr and Bolshakov [35] from

experimental data, showed that the unloading data could be better described using power law functions of the form shown in equation (2.6 & 2.7), with exponents ranging from 1.2 to 1.6. Also, they found the flat punch approximation to be lacking as indicated by stiffness and hence area changes with unloading for the materials tested in their experimental work. They proposed that the contact stiffness be measured at peak load only, and that no restrictions were placed on the unloading data being linear during any portion of the unloading event. They rewrote equation (2.8) as

$$E^* = \frac{\sqrt{\pi}}{2}\frac{S}{\sqrt{A}} \tag{2.10}$$

The above equation is a general relationship that applies to all axis-symmetric indenters with a smooth profile [38]. Oliver and Pharr also made use of an indenter shape function to correct for the contact area at peak load. This function relates the cross-sectional area of the indenter to the distance from its tip, and can be determined experimentally using a material with known mechanical properties. They further proved that for the conical and paraboloid indenters, the contact depths are greater than those for the flat punch, and introduced the geometric constant, ε , to account for the differences, such that

$$h_p = h_t - h_e \tag{2.11}$$

and

$$h_e = \varepsilon \frac{P_{\max}}{S} \tag{2.12}$$

where h_p, h_t, and h_e are the contact depth (due to plasticity), total depth and depth due to elastic deformation, respectively, and P_{max} is the maximum load. They showed that the value of ε ranged from 0.72 for a conical indenter to 1 for a flat punch. For an indenter that could be described as a paraboloid of revolution, ε = 0.75. The method of Oliver and Pharr will be discussed in more detail in section 2.4.3.1.

2.4.2 Indenter geometry

Modern micro-indentation tests allow the applied load, typically in the order of milli-Newtons, to be controlled while the indenter displacement, typically in nanometres, is continuously measured during the loading and unloading cycle. This approach enables the hardness, elastic modulus; yield strength and the energy spent on loading and unloading to be determined. The two most popular indenter geometries used are the spherical and the three-sided pyramidal, or Berkovich indenter. The Berkovich is preferred to the four-sided Vickers indenter as the apex of the former can be more readily fashioned to meet at a point. The main advantages and disadvantages of both types of indenters are listed below:

Spherical Indenters

Advantages:

- Stresses and displacements of the initial elastic penetration are adequately described by the Hertzian equations.
- The average strain increases with penetration depth, enabling the determination of strain hardening.

- Orientation does not play a role in the examination of properties of anisotropic materials and single crystals.

Disadvantages:

Sufficiently accurate results can only be obtained within a limited range of depth, since:

- At depths greater than about ¼ of the tip radius, the conical shaft of the indenter comes into contact with the specimen; and a suitable model to describe spheroconical indenters is still lacking. Hence the Hertz equations, upon which the unloading is based, is only valid for indentations where the contact diameter is small in comparison to the indenter diameter.
- Real indenters are not perfectly spherical and the radius of curvature tends to vary with distance from the tip. However, calibration and the use of correction functions can minimise this problem.

Pointed indenters

Advantages:

- The stress distribution is similar at any depth of penetration and the average strain is constant.
- The average contact pressure or hardness is constant at any depth. Hence the properties of coating can be separated from the influence of the substrate and trends between different coatings can be examined.

Disadvantages:

- Very high stresses can develop beneath the sharp tip, causing cracking in brittle materials.
- The tip and edges of real indenters are not perfectly sharp and the bluntness can result in a decrease of observed hardness with indentation depth.
- The measured indentation depth is slightly different from an ideal indenter, due to tip bluntness. However, this can be corrected using suitable calibration procedures.
- The continuously varying slope of the unloading curve requires the use of appropriate power law curve fitting procedures, in order to calculate the elastic modulus.

2.4.3 Analysis of indentation test data

The validity of the results for hardness and modulus depends largely upon the analysis procedure used to process the raw data. Currently, the most commonly used methods are the “Oliver and Pharr” method [32] and the “Field and Swain” method [39].

2.4.3.1 Oliver and Pharr method

From a typical indentation experiment using a pyramidal Berkovich indenter, a set of load vs. penetration data such as shown in Figure 2.3 is obtained. In the figure, h_r is the depth of the residual impression; h_t is the total penetration by the indenter at maximum load. Elastic recovery can be obtained by examining the initial portion of

the unloading slope. Oliver and Pharr recognized that significant amount of creep caused the slope of the upper portion of the unloading curve to be abnormally high and introduced a holding period at peak load to saturate this effect. That is, the peak load is held constant until the creep strain reduces to a small enough extent that it does not affect the shape of the unloading curve. It should be noted that for many compliant materials, such as polymers, creep effects may not diminish sufficiently even after prolonged holding times. Creep effects will be discussed further in section 2. 6. Recall that equation (2.7) is the power law relationship between load and displacement that describes the unloading data:

$$P = n\left(h - h_f\right)^m \tag{2.7}$$

where the constants *n*, *m* were determined by a least squares fitting procedure; *h* is the depth of penetration and h_f is the final or permanent depth of penetration after the indenter is fully unloaded (sometimes the term h_r is used instead, for residual penetration depth). The initial unloading slope was then found by analytically differentiating equation (2.7) and evaluating the derivative at the peak load and displacement.

Also, on unloading, the vertical displacement due to elastic recovery h_e , can be expressed as

$$h_e = \varepsilon P_{max}/S \tag{2.12}$$

and

$$S = \varepsilon P_{\max}/h_e \tag{2.13}$$

where ε = 1 for a cylindrical punch and = 0.75 for a Berkovich indenter

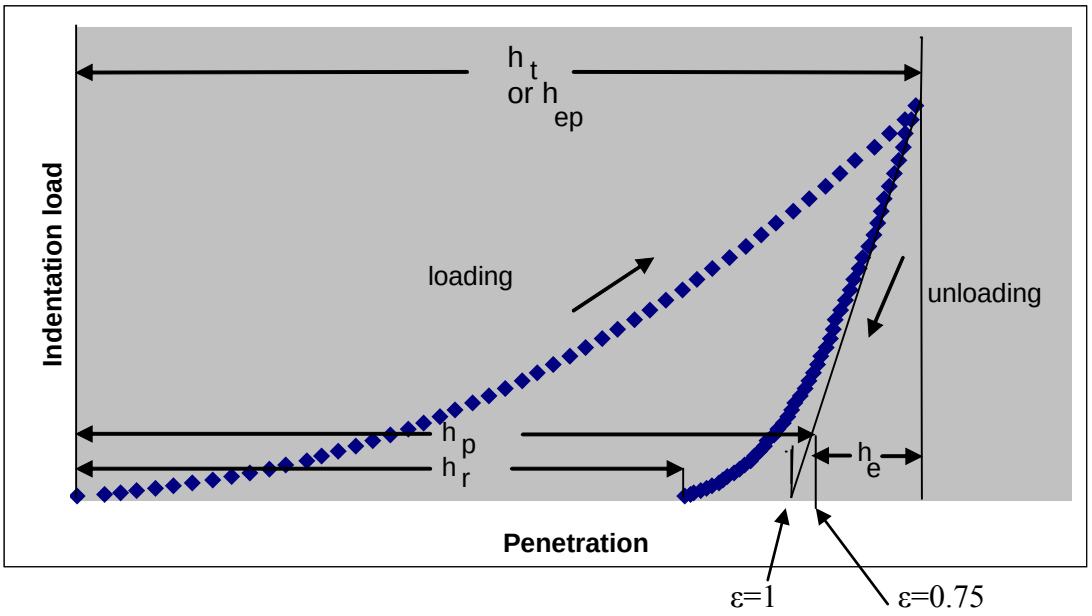

Figure 2.3: Load vs. displacement for elastic-plastic loading followed by elastic unloading.

Oliver and Pharr further showed that the area function for a perfect Berkovich indenter was:

$$A(h_p) = 24.5h_p^2 \qquad (2.14)$$

where h_p is the displacement due to plastic deformation.

Using equations (2.10) and (2.14) , the reduced modulus of a material could be determined by indentation method, using a Berkovich indenter, as follows:

$$E^* = \frac{S}{2kh_p} \qquad (2.15)$$

where k is a geometric factor.

For a spherical indenter, the contact area is

$$A = \pi a^2$$

where a is the radius of the circle of contact. Hence equation (2.10) can be rewritten as:

$$E^* = \frac{S}{2a} \tag{2.16}$$

and a can be obtained from geometry, using Pythagoras theorem:

$$a = \sqrt{2R_i h_p - h_p^2} \tag{2.17}$$

where R_i is the indenter radius, so that the reduced modulus can be obtained from:

$$E^* = \frac{S}{2\sqrt{2R_i h_p - h_p^2}} \tag{2.18}$$

2.4.3.2 The ‘Field and Swain’ method (load-partial unloading)

The theory is based on Hertz’s equation for elastic contact and Hertz’s relationship between force and displacement [40, 41, 42]:

$$a^3 = \frac{3}{4E^*} PR \qquad (2.19)$$

and

$$P = \frac{4}{3} E^* R^{1/2} h_e^{3/2} \qquad (2.20)$$

Substituting equation (2.19) into equation (2.20) gives:

$$E^* = \frac{3P}{4ah_e} \qquad (2.21)$$

Unlike the case for the pointed indenter, the elastic recovery for the case of the spherical indenter is $h_e/2$. It should be pointed out that equation (2.16) and equation (2.21) were derived upon the basis of reloading onto a preformed impression by the same indenter. If the depth of the preformed impression is h_r, upon reloading to maximum load P_{max}, the reloading is elastic through a distance

$$h_e = h_t - h_r \qquad (2.22)$$

Plastic deformation can be given as:

$$h_p = h_t - h_e / 2 \qquad (2.23)$$

Since h_t is a measurable quantity, equation (2.22) shows that if h_r is known, then h_e could be calculated. From equation (2.23) h_p could be obtained, then a could be estimated using equation (2.17). Hence E^* could be obtained from equation (2.21). Using the loading-partial-unloading procedure developed by Field and Swain [39], h_r could be obtained indirectly. If the indenter is unloaded to an intermediate load P_i from the full load P_{max}, the measuring instrument will provide the corresponding values for displacement, viz., h_i and h_t, respectively. The value h_r is found by forming the ratio

$$\left(P_{\max} / P_i\right)^{2/3} = \left(h_t - h_r\right)/\left(h_i - h_r\right) \qquad (2.24)$$

thus

$$h_r = \frac{h_i (P_{\max} / P_i)^{2/3} - h_t}{(P_{\max} / P_i)^{2/3} - 1} \qquad (2.25)$$

From each partial unloading, a value of E* (or hardness) can be obtained by solving equation (2.20), with the aid of equation (2.22), hence this method provides a quick mean of probing mechanical properties through the thickness of a sample.

2.4.4 Errors associated with hardness and modulus determinations

The errors that are associated with depth-sensing micro-indentation tests have been reviewed in detail [42, 43]. Those deemed relevant to the present problem are summarised below:

Initial depth of penetration

An initial depth of penetration exists for every indentation test as the indenter makes initial contact with the sample. This depth is not measured and must be accounted for and added to the subsequent depth measurements. This is usually achieved using suitable regression curve to the initial points of the load-displacement curve, and extrapolating it to zero load.

Indenter tip shape

In practice, indenters are usually made from diamond since it is important that the indenter is harder than the material being indenter so that the indenter does not deform plastically during indentation. As it is virtually impossible to fashion a perfectly sharp indenter, one would expect a difference between the actual contact area and the area corresponding to an ideally sharp indenter. This difference is more significant at small depths of penetration because of the unavoidable small rounding at the tip, and can contribute to an apparent change in hardness with load. There are two methods to correct for the imperfect tip shape. The first is by direct imaging and measurement of the tip geometry using either an atomic force microscope (AFM) or a scanning electron microscope (SEM). The measured area is then plotted against the depth, and using regression analysis of an appropriate order, an analytical function is obtained which gives the actual projected area for a given value of h_p. This function is commonly called the “area function” for the particular indenter being characterized. The direct method is often difficult to perform and a more common approach is the indirect method for determining the area function. The procedure was

mentioned earlier and involves performing a series of indentation at varying loads (hence varying displacement) on a standard material with known elastic modulus and Poisson's ratio. Hence the actual contact area *A* for any given h_p is obtained.

Recent studies by Giannakopoulos [44] on the influence of imperfections in pyramid indenters on elastic and viscoelastic indentation of flat surfaces revealed that small variations of angles between pyramid planes have small influence on the contact area, but have considerable influence on the load-displacement response.

Surface roughness

At the initial stage of loading, the indenter touches the sample at the asperities and the contact area is smaller than the theoretical area, giving rise to a lower apparent stiffness of the material. At higher loads, the contact points undergo deformation due to the high stress concentrations and the sample response begins to move towards the ideal situation. With ultra-micro hardness tests, it has been suggested that the modulus and hardness values calculated for small penetration depths (typically below 20nm) are inaccurate [43].

Compliance of the measuring system

The measuring system consisting of the indenter, specimen holder and measuring head, etc, has its own compliance and results in a larger measured displacement than the actual depth of penetration. The compliance of the measuring system must therefore be corrected for. The method for this correction is outlined elsewhere [42] and not included here since for commercial instruments, the compliance has already been corrected for and incorporated into the analysis software.

Thermal Drift

Temperature fluctuations in the specimen, indenter or in parts of the measuring device can lead to incorrect displacement measurements. It is therefore important for proper temperature equalisation prior to testing.

Other factors

Other factors associated with testing are inherent errors in the measuring of load and displacement, as well as noise in the system and inhomogeneity of the sample.

2. 5 Nano-indentation

The ability of the atomic force microscope (AFM), scanning force microscope (SFM) or scanning probe microscope (SPM) to create three-dimensional micrographs with resolutions down to the nanometre scale has made it an essential tool for imaging. In addition to this, AFM/SFM/SPM can also probe nanomechanical properties [45 - 69]. An advantage of using the AFM for indentation work, in theory, is the ability for in-situ imaging of the indentation. The small forces applied and the small indentations also mean that very small phases in the material can be tested in isolation. A force plot reflecting changes in the photo detector voltage, caused by cantilever deflection, as well as the z-piezo movement (in Volts) can be obtained. This in turn can be converted to load-displacement plots from which the elastic properties can be determined using the same method as for the micro-indentation.

The method to convert ‘force plot’ to load-displacement plots will be discussed in the section that follows.

2.5.1 Force plots

Force plots generated in contact mode have also been used to determine elastic properties, with some success. A typical force plot is shown in Figure 2.4.

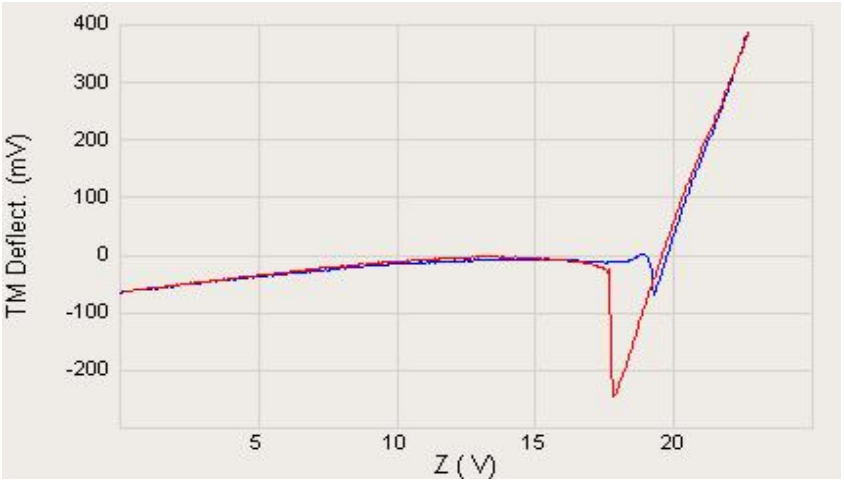

Figure 2.4: Force plot generated using an AFM on a silicon sample, showing loading curve (red) and unloading curve (blue)

In a force curve the cantilever deflection is recorded as a function of the height of the sample (in Z direction). There are generally two regions: a flat one, where the tip is not touching the sample and thus the deflection is constant, and a sloped one, where the deflection is proportional to the sample height, when the tip is in contact with the sample. The large dip in the loading curve occurs due to the strong attraction of Van der Waals force pulling the cantilever to the sample surface before contact. The smaller dip on the unloading curve is caused by adhesion before the cantilever tip

pulls off the sample surface. The offset between the two dips is caused by the permanent deformation (plasticity). Similar to conventional curves generated by depth sensing instruments, the slope of the unloading curve is steeper than for the loading curve, if permanent penetration or viscous losses has occurred.

For a soft sample, the slopes for both the loading and unloading curves in the contact region will be gentler than for a stiff material, since the cantilever defection is smaller than the z movement of the sample due to more penetration by the indenter into the sample. The force curve in the contact region also becomes non-linear for more compliant materials. The point of contact (slope change, true height of sample surface) will differ more as the indentation load increases.

Yao et al. [58] used force plots to compare the elastic modulus of a number of polymer network gels. The work was carried out using silicon nitride cantilevers with pyramid tips, having force constant of 0.12 N/m and tip opening angle of 45^{o}. The force curve of a cleaved mica support was recorded as a reference and to determine the photodetector sensitivity. In this work the force curves (Z-position vs. cantilever deflection in nm) for mica and the gel samples were compared. The amount of indentation was calculated by taking the difference in deflection of the gel sample and the mica reference (the gel sample exhibited lower deflection as it is softer). The force-indentation relationship was then represented using the Hertzian model. The paper cited two appropriate geometries for describing the AFM tip and the sample: either a sphere or a cylindrical cone indenting into a planar soft sample. The paper used the latter in the analysis. Thus the force-indentation relationship predicted by the Hertz model was given by

$$F = \frac{\pi}{2}\frac{E}{(1-\nu)}\tan(\alpha)\delta^2 \qquad (2.26)$$

where E = elastic modulus of the sample,

α = opening angle of the tip,

δ = indentation,

ν = Poisson ratio of the sample.

The loading force was written as

$$F = Kd \qquad (2.27)$$

where K and d were the force constant and the cantilever deflection, respectively. The elastic modulus could then be obtained by plotting log F as a function of log δ, and by applying a linear fit. For the gel films analysed, the modulus values were found to be in the range of 0.14 to 1.26 MPa, depending on swelling time and the pH of the solution.

Hofmann et al. [59] used force mapping (force curves as a function of lateral position) to compare the elastic properties at different sample locations of living chicken cardiocytes. This technique allowed the localised elastic properties to be correlated with topography. These workers used a similar approach to the work of Yao et al., but used oxide-sharpened silicon nitride type cantilevers with a lower force constant of 20 mN/m. They also applied the Hertz model, Eq. (2.26), as well as the cone geometry for the indenter. Again, values for *E* were obtained by plotting

force-indentation data on a log-log scale. It was noted that the theoretical model matched that of the experimental results for the soft part of the cell sample, but deviated from those measured on the stiffer fibres. This was explained by the basic assumption of the Hertz model of sample homogeneity, which did not apply in areas where the stiff fibres were embedded in the softer parts of the cell.

Although it is evident that force plots could be used to generate force-indentation curves from which elastic modulus could be calculated, uncertainty remains as to the geometry of the tip and the contact geometry between the tip and the sample. Blach et al. [60] compared force-displacement expressions for different tip geometries to find the most appropriate geometry. They made use of Sneddon's relationship, Eq.(2.6), and plotted ln(P) vs. ln(h). From the slope of the resultant straight line, the exponent m was determined. Since m = 2 for conical indenters, m = 1.5 for a paraboloid and m = 1 for a flat cylinder, comparison of the m value would give an indication of the most appropriate tip geometry to apply in the analysis for the modulus value. Another method was proposed by Reynaud et al. [61] to avoid the limitation of unknown tip geometry. This relative method involved a calibration step with a set of reference polymers with known E values. They made use of the method of Sneddon and Oliver and Pharr, as described in the section for micro-indentation methods. They assumed that at maximum force the total displacement was the sum of both the elastic and the plastic components. They further proposed that the first phenomenon to occur when the tip was withdrawn was the elastic recovery of the zone near the contact area: for the initial stage of the unloading curve, the slope S was the tip-sample contact stiffness and that adhesion was negligible.

From equations (2.7) and (2.8), S could be expressed as:

$$S = \frac{dP}{dh}\Big|_{P\max} = mn(h - h_f)^{m-1} \qquad (2.28)$$

and

$$A = C(h_p)^2$$

where C is a constant. Also

$$h_e = h - h_p = \varepsilon P_{max} / S$$

where ε = 0.75 for a paraboloid of revolution, = 0.72 for a conical indenter and = 1 for a flat punch. From equation (2.10), *E* could then be rewritten as:

$$E = \frac{(1-\upsilon^2)\sqrt{\pi}}{2\sqrt{C}} f \qquad (2.29)$$

where

$$f = \frac{S^2}{(Sh_{\max} - \varepsilon P_{\max})} \qquad (2.30)$$

The validity of the method was based on using the following assumptions:

- The load must be normal to the sample surface and uniaxial;
- The tip keeps the same unknown but regular geometry without deformation during the experiment;
- Indentation must exceed a few nanometres, unless C was not a constant.

In reality, the cantilever was slightly tilted and the tip might break on hard samples, hence the method was limited to material of low modulus.

In the actual experimental work by Reynaud and co-workers [61], a set of reference samples with different known elastic modulus was selected for calibration. Indentation curves were obtained, giving S, h_{max} and then f. A plot of f vs. E would give the calibration curve from which the Young's modulus of unknown samples could be deduced by determining the corresponding f values.

As can be seen from Figure 2.4, the force plots generated by commercial AFMs are generally given in voltage and must be converted to nanometres. This is achieved through the use of the sensitivity parameter [62] to relate the photo detector voltage change (caused by cantilever deflection) to the actual cantilever bending. Sensitivity is the slope of force curve generated in the repulsive region. This parameter depends on various factors such as the cantilever geometry and the feedback laser alignment as well as on the material of interest. Under the same operation conditions, material with higher elastic modulus yields a steeper slope due to less indentation with the same applied force. When the sensitivity is calibrated on a material much stiffer than the cantilever, a conversion factor can be obtained which relates the photo detector voltage change with the actual cantilever. The relationship between the z-piezo travel (Δz_p), the cantilever deflection (Δz_c) and the indentation depth (Δz_i) is,

$$\Delta z_p = \Delta z_c + \Delta z_i \qquad (2.31)$$

Δz_p can be converted through the voltage applied to the piezo tube, and Δz_c can be obtained once the photo detector voltage is calibrated. A material of 'infinite

hardness', such as Si wafer, is used for calibration. Δz_i can then be calculated using Eq.(2.31). Given Δz_c, and the cantilever spring constant, the applied force F can be determined using Hooke's law as per Eq.(2.27). A plot of applied force F vs. indentation depth Δz_i can then be generated and the effective modulus of the material can be extracted from the unloading slope (Oliver and Pharr method), or using the Herzian equation.

Chizhik and co-workers [63] applied AFM to probe the micromechanical properties of compliant polymeric materials. Classical models of elastic contacts, Sneddon's, Hertzian, and the model of Johnson, Kendall and Roberts (also known as the JKR model), were tested for various indentation depths for a rubber sample. The JKR model incorporates the effect of adhesion into the Hertzian contact, using a balance between the stored elastic energy and the loss in surface energy [64]. Elastic response was controlled by the observation of indentation area after force measurements, and normal loads were selected to ensure an absence of indentation marks. Force-distance curves were used with approach-retract frequency in the range 0.02-183 Hz. Spring constants ranged from 0.25 to 21 N/m. The stiffer cantilevers were used on the harder samples. It was observed that at indentation depths of below 30nm, unstable results were obtained which were related to the destabilizing attractive force gradient in the vicinity of surfaces. All three models gave convergent results and were very close to the absolute E of rubber. Due to this observation, subsequent calculations for the other polymer samples were only done using the Herzian approach and the results showed strong frequency dependence, but in general the values were comparable to the reported values. Rubber, of course, shows

little plastic deformation so that the Sneddon correction for elastic-plastic behaviour was not necessary. Similarly, the JKR model corrects for the case where substantial adhesion occurs between the sample and indenter. Such corrections were not important in this particular study.

In summary, modulus values can be obtained using force plots and cantilevers of appropriate stiffness. Once the data is converted to force-displacement information, using Hooke's law and proper calibration procedures, various analytical methods can be applied to yield the modulus values. These methods include elastic contact models such as Sneddons, Hertz and JKR; and the use of the Oliver and Pharr method. The problem of unknown tip geometry can be overcome by employing the calibration method of Reynaud et al. [61] using polymers of known mechanical properties for calibration.

In principle, a dynamic AFM experiment can be used to obtain viscoelastic properties of polymeric samples. These can be done by oscillating the cantilever or the surface either normal or perpendicular to the surface. The most common method is the force modulation microscopy whereby the height of the sample is modulated during the scan. The induced modulation of the cantilever deflection is detected via a lock-in amplifier. The amplitude and phase shift of this response are characteristic of the complex modulus of the sample. The obtained results, however, are mainly qualitative, as the dimension of the contact area is difficult to determine and friction phenomena at contact are likely to affect the measurements. Despite these shortcomings, dynamic AFM experiments are still considered useful in providing better understanding of localized material properties and some experimental work

has been carried out in an attempt to provide quantitative material property values. These will be briefly described below.

For a linear viscoelastic material, a simple "Voigt" model can be constructed where the sample and the AFM instrument are assumed to be a "black box" composed of elastic (storage), viscous (loss), and inertial components. Braithwaite & Luckham [65] based on earlier work by Radmacher, obtained relationships for complex shear modulus G, based on measurable AFM data, as follows:

$$G'(\omega) = \frac{\gamma k}{b} \frac{(\cos\varphi - \gamma)}{\gamma^2 - 2\gamma\cos\varphi + 1} \qquad \text{and}$$

$$G''(\omega) = \frac{\gamma k}{b} \frac{(\sin\varphi)}{\gamma^2 - 2\gamma\cos\varphi + 1} \qquad (2.32)$$

The above equations were presented in terms of the cantilever stiffness *k,* the detected signal γ (the ratio of detected to drive amplitudes) and φ (the phase difference between the drive and received signals). This signal is not the rheological phase lag (i.e., the phase between the stress and strain), but rather the mechanical lag (the phase between the force and displacement). The geometric coefficient, *b*, is critical for obtaining quantitative results. In the experimental work by Braithwaite on adsorbed gelatine layers, the modulus results were presented as *b* x G^* to remove uncertainties associated with the determination of *b*, and interesting qualitative information was obtained. In particular, the cross-over from viscous to elastic behaviour appeared to be frequency sensitive as did the viscous term. However, it should be noted that the rheological lag could be determined more accurately as it was independent of the value *b*, as follows:

$$\tan\delta = \frac{G^{''}}{G^{'}} = \frac{\sin\varphi}{\cos\varphi - \gamma} \tag{2.33}$$

McGuiggan & Yarusso [66] modified the instrumentation of the AFM by attaching the sample to a piezo transducer (PZT). Modulation was attained by inputting a sine wave signal into the PZT via a function generator. The amplitudes of the PZT actuators were measured independently using a profilometer. The vertical deflection photodiode signal was monitored and fed into a lock-in amplifier. The phase of the photodiode output relative to the input signal was measured using the lock-in amplifier. Measurements were first made on a stiff surface to establish the baseline phase shift, θ_o, and for photodiode calibration. Since no theoretical model exists to predict the response of viscoelastic material under small sinusoidal oscillations, of finite thickness, and having a contact area comparable to the diameter of the probe (a 30μm diameter glass probe was used), quantitative measurements were restricted to that of the loss tangent,

$$\tan\delta = \frac{\sin\varphi}{\cos\varphi - \left(V_0^{o}V_1 / V_1^{o}V_0\right)} \tag{2.34}$$

The extra term $V_0^{o}V_1 / V_1^{o}V_0$ occurred due to the coupling between the spring and the sample, and V_0 and V_1 were the applied voltage and the corresponding resultant voltage generated by the cantilever deflection, respectively. The superscript denoted values from the stiff surface. As all the parameters in Eq. (2.34) were measurable

experimentally, tan δ could be obtained. Furthermore, when a geometric prefactor was used, qualitative estimates of $G^{'}$ and $G^{''}$ could be obtained.

Earlier on it was mentioned that a major contribution to difficulties in obtaining quantitative material properties using dynamic AFM techniques was due to contact friction. Fretigny & Basire [67, 68] attempted to use lateral modulation in the static friction regime to obtain material properties of viscoelastic materials. In the earlier paper published in 1997 [68], they applied modulation in the direction of the cantilever axis. They observed linearity when the cycle aperture was varied with scan amplitudes, when the amplitudes were less than the penetration depth δ, and derived equations for modulus in the form of:

$$E^{''}(\omega) = \frac{1}{c}\frac{\Delta z}{s\delta} \qquad \text{and}$$

$$E^{'}(\omega) = \frac{1}{c\delta}\left(\frac{H}{s} - d\right) \qquad (2.35)$$

where *H* was the height of the cycle. The constants *c* and *d* were values for cantilever stiffness and geometry, and could be obtained by taking measurements on a known sample, using the same cantilever and without modifying the laser tune. In the later work by Basire & Fretigny [67] the modulation was applied laterally in a perpendicular direction to the axis of the cantilever, in the static friction regime. The experiment was performed under zero applied normal load and the torsion of the cantilever, due to the lateral movement, was converted to tangential force.

As a starting point an elastic material was considered and the response of the contact was given as:

$$T = \frac{16}{9} Ead \qquad (2.36)$$

where T is the tangential force, E is the elastic modulus, a is the contact area and d the displacement.

The above equation could be applied to viscoelastic material since the domain where the boundary conditions apply does not vary with time. For the case of constant velocity displacement, the relaxation modulus $E(t)$ was expressed as:

$$T(t) = \frac{16}{9} a \int_{-\infty}^{t} E(t - t') \frac{dy}{dt'} dt' = \frac{16}{9} a \upsilon \int_{0}^{t} E(t') dt \qquad (2.37)$$

It was argued, using geometric considerations, that the above relationship was valid for pyramidal punches, such as an AFM tip. Furthermore the contact area could be expressed as:

$$a = \frac{4}{\pi} \delta \tan \gamma \qquad (2.38)$$

where δ is the indentation depth and γ is the average half-angle of the punch. The geometric factor $4/\pi$ was used for the pyramidal shape. The relaxation modulus could be obtained by differentiation of the striction curve obtained experimentally.

Through the use of a linear operator $\overline{E^*}$, equation (2.36) could be expressed as:

$$T(t) = \frac{16}{9} a \overline{E^*}[d(t)] \qquad (2.39)$$

When a displacement $y(t)$ was imposed on the sample, a portion of it, $y_c(t)$, was transmitted to the cantilever such that the contact displacement $d(t) = y(t) - y_c(t)$. If k_{ty} represented the lateral cantilever stiffness, the forces at equilibrium could be written as:

$$\frac{16}{9} a \overline{E^*} [y(t) - y_c(t)] = k_{ty} y_c(t) \tag{2.40}$$

The displacement of the sample, $y(t)$, followed a saw tooth law and could be represented by its Fourier expansion:

$$y(t) = -\frac{4s}{\pi^2} \sum_{n=0}^{\infty} \frac{1}{(2n+1)^2} \cos[(2n+1)\omega t] \tag{2.41}$$

where s represented the displacement amplitude and $\omega / 2\pi$ its frequency.

The periodic response, $y_c(t)$, was expressed as:

$$y_c(t) = \frac{T(t)}{k_{ty}} = \sum_{n=0}^{\infty} \{a_{2n+1} \cos[(2n+1)\omega t] + b_{2n+1} \sin[(2n+1)\omega t]\} \tag{2.42}$$

where the coefficients a_{2n+1} and b_{2n+1} depended on the excitation frequency.

Finally, combining equation (2.38) and solving for equation (2.40) for each harmonics led to:

$$E'\left((2n+1)\omega\right) = -\frac{k_{ty}\alpha}{\delta}\frac{b_{2n+1}^2 + a_{2n+1}\left(\lambda_{2n+1} + a_{2n+1}\right)}{\left[\left(\lambda_{2n+1} + a_{2n+1}\right)^2 + b_{2n+1}^2\right]} \quad \text{and}$$

$$E''\left((2n+1)\omega\right) = \frac{k_{ty}\alpha}{\delta}\frac{b_{2n+1}\lambda_{2n+1}}{\left[\left(\lambda_{2n+1} + a_{2n+1}\right)^2 + b_{2n+1}^2\right]} \tag{2.43}$$

where $\lambda_{2n+1} = \frac{4s}{\pi^2}\frac{1}{(2n+1)^2}$ and $\alpha = \frac{9\pi}{64\tan\gamma}$

The coefficients a_{2n+1} and b_{2n+1} were obtained by Fourier analysis of the tangential force response at a given excitation frequency.

The relationship for the loss angle was also derived:

$$\Delta\left((2n+1)\omega\right) = -\tan^{-1}\left(\frac{b_{2n+1}}{a_{2n+1}}\right) \tag{2.44}$$

The above method was successfully applied to styrene-butadiene copolymer, and was said to be suitable for samples with relaxed modulus ranging from 0.1 to a few MPa. For such compliant materials, the indentation depths were large and the method was not too sensitive to the precise tip shape. However, for higher moduli, the contact area would be reduced and the static friction domain would be much smaller. In such case, the tip shape geometry would become important. Also, the signal to noise ratio would be reduced as only small displacements would be possible to keep the tip in a static friction regime.

It would appear that useful qualitative and semi-quantitative information regarding viscoelastic properties of polymeric materials can be obtained using the AFM for

indentation. The major drawback of the method is the difficulty in determining the cantilever tip shape, as well as the lack of frictional information. In the static friction regime, lateral modulations gave acceptable modulus values for materials with relaxed moduli ranging from 0.1 to a few MPa.

It should be noted that from the literatures concerning nano-indentation experiments using AFM, the common practice was to use a ‘stiff’ material for calibration, even though error due to deformation of the tip is likely to occur.

2. 6 Treatment for viscoelasticity

As was mentioned earlier, a polymer may exhibit mechanical behaviour characteristic of either an elastic solid or a viscous liquid. The actual response depends upon temperature, in relation to the glass-transition temperature (T_g) of the polymer, and upon the time scale of the deformation. It is common for polymers to exhibit intermediate response, i.e., to exhibit creep (which may be a result of viscoelasticity or viscoplasticity). There are two basic approaches to managing time-dependent behaviour in indentation testing. The first is the application of an oscillatory displacement or force, in which the transfer function between the load and displacement provides a method of calculating the storage and loss modulus of the material [65 - 69]. The second is by means of creep or relaxation experiments and suitable mechanical models to estimate time dependent properties [70 - 94].

A major impediment to the use of elastic equations of contact in the analyses of indentation data for soft, compliant polymeric materials is the time-dependent

response (creep), leading to ambiguity in the interpretation of load-displacement data. Indeed, the standard Oliver and Pharr method as described in section 2.4.3.1 makes use of the unloading response of the material and assumes that the unloading behaviour is purely elastic. An experimental approach to remove this ambiguity is to eliminate the time dependence, for example, by allowing sufficient time at peak load for creep effects to saturate. However, such approach might not always be practical, and may not work for compliant polymers whose creep response may not saturate sufficiently even after prolonged holding times at maximum load. Therefore, there is a need to incorporate viscoelastic models into indentation analysis for compliant polymers. Bearing in mind that creep might be a combination of visco-elasticity and visco-plasticity, the validity for using viscoelastic models would require the absence of viscoplasticity. This can be verified by allowing a prolonged holding time at the end of the unloading cycle, to ensure that the displacement due to creep recovery is the same as that during creep, and thus proving the absence of delayed plasticity.

2.6.1 Mechanical models using springs and dashpots

Basic mechanical models exist which attempt to describe the stress-strain response of viscoelastic materials. These models are based on a combination of an ideal linear elastic spring, as the elastic element, and a dashpot as the viscous element. The dashpot may be viewed as a shock absorber consisting of a piston in a cylinder filled with Newtonian fluid of viscosity η. Two simple elemental models are; a series combination of a spring and dashpot, the Maxwell element (Figure 2.5), and a parallel combination of a spring and dashpot, the Voigt element (Figure 2.6) [86].

The Maxwell element

Figure 2.5: The Maxwell element as a series combination of a spring and a dashpot.

In the case of a series combination of a spring and a dashpot (Figure 2.5), the total strain (or strain rate) is the sum of the individual strains (or strain rates) of the spring and the dashpot. From Hooke's law ($\sigma = E\varepsilon$), the strain rate of the spring can be written as

$$\frac{d\varepsilon}{dt} = \left(\frac{1}{E}\right)\frac{d\sigma}{dt} \tag{2.45}$$

while the strain rate for the dashpot is obtained by rearranging Newton's law of viscosity as

$$\frac{d\varepsilon}{dt} = \frac{\sigma}{\eta} \tag{2.46}$$

Therefore the total strain rate for the Maxwell model is

$$\frac{d\varepsilon}{dt} = \left(\frac{1}{E}\right)\frac{d\sigma}{dt} + \frac{\sigma}{\eta} \tag{2.47}$$

In a creep experiment, a constant stress, σ_0, is applied instantaneously. The total strain is then reduced to

$$\frac{d\varepsilon}{dt} = \frac{\sigma_0}{\eta} \tag{2.48}$$

Integrating the above will yield

$$\varepsilon(t) = \left(\frac{\sigma_0}{\eta}\right)t + \varepsilon_0 \tag{2.49}$$

where ε_0 represents the instantaneous strain response of the spring element at time $t = 0$. The creep compliance, D(t) is then given by

$$D(t) = \frac{\varepsilon(t)}{\sigma_0} = \frac{t}{\eta} + \frac{\varepsilon_0}{\sigma_0} = \frac{t}{\eta} + D \tag{2.50}$$

where D is the instantaneous compliance of the spring element.

In a stress-relaxation experiment where the strain (ε_0) is constant and the total strain rate is zero,

$$\left(\frac{1}{E}\right)\frac{d\sigma}{dt} + \frac{\sigma}{\eta} = 0 \tag{2.51}$$

Introducing the relaxation time, $\tau = \frac{\eta}{E} = \eta D$, the above equation can be rewritten as

$$\frac{d\sigma}{\sigma} = -\left(\frac{1}{\tau}\right)dt \tag{2.52}$$

and integrating the above gives the stress response

$$\sigma = \sigma_0 \exp\left(\frac{-t}{\tau}\right) \tag{2.53}$$

where σ_0 is the instantaneous stress response of the spring element.

One can also relate the stress relaxation modulus to the instantaneous elastic modulus (E), as follows:

$$E_r(t) = \frac{\sigma}{\varepsilon_0} = \left(\frac{\sigma_0}{\varepsilon_0}\right)\exp\left(\frac{-t}{\tau}\right) = E\exp\left(\frac{-t}{\tau}\right) \tag{2.54}$$

Voigt Element

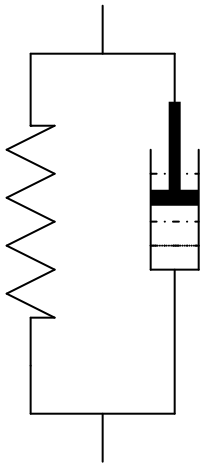

Figure 2.6: The Voigt element as a parallel combination of a spring and a dashpot.

For a parallel combination of a spring and dashpot (Figure 2.6), the strain on each element must be equal while the stress is additive. The fundamental relation for the Voigt model is,

$$\sigma = E\varepsilon + \eta \frac{d\varepsilon}{dt} \tag{2.55}$$

In the case of creep, the above equation can be rewritten, by making use of the relaxation time τ , as a linear differential equation:

$$\frac{\sigma_0}{\eta} = \frac{\varepsilon(t)}{\tau} + \frac{d\varepsilon(t)}{dt} \tag{2.56}$$

Making use of an integrating factor ($e^{t/\tau}$), the above equation can be solved to yield the compliance function:

$$D(t) = D\left[1 - \exp\left(\frac{-t}{\tau}\right)\right] \tag{2.57}$$

In contrast to the Maxwell model, the Voigt equation cannot be solved in any meaningful way for stress relaxation.

Further modifications to these basic models are often employed to better describe indentation creep responses. For example, the basic Maxwell and Voigt models are often used in combination to better describe viscoelastic behaviour in plastics.

Fischer-Cripps [83] attempted to model the creep behaviour of polymeric and metallic materials under indentation loading using variations of both the Maxwell and the Voigt models. Equations for both the conical indenter and the spherical indenters were developed. The study showed that the models worked well for viscoelastic materials, even though the loading mode was not purely tensile or compressive. Furthermore, due to the initial plastic deformation, which occurred with the sharp conical indenter, the initial response in displacement was found to be

substantially larger than the predicted values. The models, however, worked better for the spherical indenter. Selection of appropriate loading rates were also an important factor, as too fast a loading rate tended to cause load overshoot, while too slow a loading rate tended to cause plastic deformation, which would in turn result in higher than expected depth penetration. The author further stressed that although these models were useful for comparison purposes, as values for E_i (for the various individual spring elements) and η_i (for the corresponding dashpot elements) can be determined from curve fitting and iteration procedures, they did not contribute to the basic understanding of the physical mechanisms involved in the deformation process. The basis of the models and the corresponding equations are given below:

For the case of a rigid spherical indenter in contact with a material represented by a three-element Voigt model, the Hertzian equation was modified by the addition of a time-dependent exponential, such that

$$h^{3/2}(t) = \frac{3}{4}\frac{P_0}{\sqrt{R}}\left[\frac{1}{E_1^*} + \frac{1}{E_2^*}\left(1 - e^{-tE_2^*/\eta}\right)\right] \qquad (2.58)$$

for a spherical indenter , and

$$h^2(t) = \frac{\pi}{2}P_0 \cot\alpha\left[\frac{1}{E_1^*} + \frac{1}{E_2^*}\left(1 - e^{-tE_2^*/\eta}\right)\right] \qquad (2.59)$$

for a conical indenter.

Note that E^* in this model referred to the combination of the elastic modulus and the Poisson's ratio of the specimen material ($E^* = E/(1-\nu^2)$), and not the combined modulus of the material and the indenter.

For the case of a two-element Maxwell model, the time-dependent depth of penetration was given by

$$h^{3/2}(t) = \frac{3}{4}\frac{P_0}{\sqrt{R}}\left[\frac{1}{E_1^*} + \frac{1}{\eta}t\right] \tag{2.60}$$

for a spherical indenter, and

$$h^{2}(t) = \frac{\pi}{2}P_0 \cot\alpha\left[\frac{1}{E_1^*} + \frac{1}{\eta}t\right] \tag{2.61}$$

for a conical indenter.

A more complicated four-element Maxwell-Voigt model was also applied, having equations

$$h^{3/2}(t) = \frac{3}{4}\frac{P_0}{\sqrt{R}}\left[\frac{1}{E_1^*} + \frac{1}{E_2^*}\left(1 - e^{-tE_2^*/\eta_2}\right) + \frac{1}{\eta_1}t\right] \tag{2.62}$$

and

$$h^{2}(t) = \frac{\pi}{2}P_0 \cot\alpha\left[\frac{1}{E_1^*} + \frac{1}{E_2^*}\left(1 - e^{-tE_2^*/\eta_2}\right) + \frac{1}{\eta_1}t\right] \tag{2.63}$$

for the case of spherical and conical indenters, respectively.

The major advantage of the Fischer-Cripps model is that it is mathematically simple to use and to computerize. Curve fitting can be improved simply by adding more elements in series. The main disadvantages are that besides the E_1^* term, and the η_1 term which could be related to the elastic modulus, and viscosity, respectively, all the other terms may not have any physical meaning. Another drawback is that there is substantial error in modelling the initial loading, and it is more pronounced for sharp indenters. The method is also sensitive to loading rates, as the model is valid for instantaneous step loading, which in practice could be approximated by a fast loading rate.

Yang et al. [84] developed an elastic-viscoelastic-viscous (EVEV) model based on a generalised Kelvin model and indentation using a flat punch indenter. The Kelvin model consists of a series of dashpots and linear springs and in its simplest form, the Kelvin model is the Voigt element [94]. This model is usually used to describe the creep of polymers. The model was modified and shown to be applicable for the Berkovich indenter on a number of polymers. The authors claimed that the method was more appropriate for determining the elastic modulus of viscoelastic materials than the Oliver and Pharr method, as it did not rely on the determination of the unloading slope in the calculation of the elastic modulus, hence reducing the error introduced by creep. However, due to substantial plastic deformation occurring in the case for the Berkovich indenter, the authors still had to make use of the Oliver and Pharr method to determine the displacement due to elastic and plastic deformation, such that the plastic component could be subtracted from the overall displacement prior to modelling. The remaining creep displacement was fitted using the model by

an iterative process to determine the elastic modulus of the material. A more detail description of the model is given below:

In its generalised form, the strain change can then be expressed as:

$$\varepsilon = \frac{\sigma_0}{\mathrm{E}_0} + \sum_1^n \frac{\sigma_0}{\mathrm{E}_i}(1 - e^{-\mathrm{E}_i t/\eta_i}) + \frac{t}{\eta_0} \qquad (2.64)$$

where σ_0 represents the stress experienced by the first spring element, t represents time; and E and η represent elastic modulus and viscosity coefficient, respectively. Also, i = 1 to n where n is the total number of two-element Voigt models used.

Yang et al. further defined indentation strain as $\varepsilon = h/h_{in}$ where h is the indentation displacement; and h_{in} is the virtual length equivalent to the displacement before creep begins, i.e., at the end of the loading cycle, at maximum load.

Equation (2.64) can then be rewritten in terms of displacement h, as:

$$h = h_{in}\frac{P_0}{E_0 A_0} + \sum_1^n \frac{P_0 h_{in}}{E_i A_0}(1 - e^{-E_i t/\eta_i}) + \frac{h_{in}}{\eta_0} t \qquad (2.65)$$

and

$$E_i = \frac{P_0 h_{in}}{A_0 h_i} \qquad (2.66)$$

where A_0 is the contact area at the end of the load cycle.

From the EVEV model, h can be expressed as:

$$h = h_e + \sum_{1}^{n} h_i (1 - e^{-t/\tau_i}) + t/\mu_0 \qquad (2.67)$$

where h_e is the instantaneous displacement of the first spring element, equivalent to the elastic displacement of the system.

For i = 0,

$$E_o = \frac{P_o h_{in}}{A_0 h_e} \qquad (2.68)$$

Again the EVEV model is mathematically simple and flexible in that more terms can be added to improve curve fitting. The physical meaning of additional terms, however, may not always be apparent. Another disadvantage is that the model still relies on the estimation of the unloading slope to approximate the elastic displacement, h_e., in order to calculate the plastic displacement and hence the contact area. The model is sensitive to loading rates. Although it is best to use fast loading and unloading, such that creep events can be restricted to the holding period, load overshoot often means that a slower loading rate is used.

Oyen and Cook [85] presented a phenomenological approach which sought to include elasticity, viscosity, and plasticity using a series of quadratic mechanical elements, to describe sharp indentation behaviour of materials having time dependent responses. Solutions to the model constitutive equation described features observed under load-controlled indentation of polymers, including creep, negative unloading tangents, and loading rate dependence. In direct analogy to the linear elastic spring and the linear dashpot, the quadratic relationships were modified to:

$$P_e = k_Q h_e^2 \tag{2.69}$$

for the spring element, and

$$P_v = \mu_Q \left(\frac{dh_v}{dt} \right)^2 \tag{2.70}$$

for the quadratic dashpot, where k_Q was defined as the quadratic stiffness, and μ_Q was defined as the quadratic viscosity coefficient.

In addition, substantial plastic deformation could occur beneath a sharp indenter under load. For a rigid, perfectly plastic material, the appropriate relationship between load and displacement was given as:

$$P_p = \alpha_1 H h_p^2 \tag{2.71}$$

where P_p and h_p are the load and displacement on the plastic element, H is the hardness, and $\alpha_1 = \pi \tan^2 \psi$ is a dimensionless geometry parameter for a sharp indenter with effective included angle 2ψ.

The displacement would be the sum of the displacement arising from the elastic, plastic and viscous responses, as would the displacement rate, as follows:

$$h = h_v + h_e + h_p$$

and

$$\frac{dh}{dt} = \frac{dh_v}{dt} + \frac{dh_e}{dt} + \frac{dh_p}{dt}$$

$$= \frac{P^{1/2}}{(\mu_Q)^{1/2}} + \frac{1}{P^{1/2}}\frac{dP}{dt}\frac{1}{2k_Q^{1/2}} + \frac{1}{P^{1/2}}\frac{dP}{dt}\frac{1}{2(\alpha_1 H)^{1/2}}$$

where

$$k_Q = \alpha_2 E', \alpha_2 = \pi/(2\cot\psi) \text{ and } E' = E/(1-\nu^2)$$

For creep at constant applied load, P_A,

$$\frac{dh}{dt} = \frac{P_A^{1/2}}{\mu_Q^{1/2}}$$

Differentiating the above equation will yield:

$$h(t) = \frac{P_A^{1/2}}{\mu_Q^{1/2}}t + P_A^{1/2}\left[\frac{1}{k_Q^{1/2}} + \frac{1}{(\alpha_1 H)^{1/2}}\right] \qquad (2.72)$$

in which the creep response is linear with time.

As with all the models mentioned before that makes use of mechanical elements such as springs and dashpots, it is simple to compute. The creep data can be used directly without further manipulations. However, the major drawback is that the determination of the tangent to the “linear” portion of the creep data is subjective and

thus error is easily introduced in the determination of the y-intercept from which the modulus value can be obtained.

2.6.2 Method of Feng and Ngan

Feng and Ngan [11, 12] suggested that the elastic recovery process occurs alongside time dependent displacement during unloading, and derived a method to correct the elastic stiffness of the indented material due to creep effects, as follows:

$$h = h_v + h_e \tag{2.73}$$

where h, h_v and h_e are the total displacement, time dependent displacement and elastic recovery, respectively. Differentiating the above will yield:

$$\left.\frac{dh_e}{dP}\right|_u = \left.\frac{dh}{dP}\right|_u - \left.\frac{dh_v}{dP}\right|_u \tag{2.74}$$

where $dh_e/dP|_u$ is simply the reciprocal of the elastic recovery stiffness S, $dh/dP|_u$ is the reciprocal of the observed initial unloading contact stiffness S_u, and $dh_v/dP|_u$ is the correction term due to time dependent effects. It was further shown that

$$\left.\frac{dh_v}{dP}\right|_u = \frac{\left.\dot{h}_v\right|_{hold}}{\dot{P}} \tag{2.75}$$

If one assumes that thermal drift is negligible, then the displacement rate due to time-dependent effects during the holding period would be due to creep effect. Furthermore, since the load P and the contact radius are continuous at the onset of unloading, it would imply that the creep rate at the onset of unloading would be

equivalent to the creep rate at the end of the holding period. Hence, the correction for the elastic recovery stiffness would be:

$$\frac{1}{S} = \frac{1}{S_u} + \frac{\dot{h}\big|_{hold}}{\left|\dot{P}\right|}. \qquad (2.76)$$

By using suitable curve fitting equations, the nose of the unloading curve could be accounted for and the elastic stiffness can be corrected to yield acceptable modulus values using the classical method of Oliver and Pharr. However, the method assumes that the creep event is restricted to the holding period, and does not correct any creep events occurring during the loading and unloading steps. Once again, fast loading and unloading rates will limit creep events during the loading and unloading stages, but load overshoot will introduce errors in the load-displacement data.

2.6.3 Superposition principle

The simplest theoretical model proposed to predict the strain response to a complex stress history is the Boltzmann Superposition Principle. It simply states that for a linear viscoelastic material, the strain response resulting from a complex loading history is the algebraic sum of the strains due to each individual step in load. It would imply that the behaviour of a viscoelastic material is a function of its entire loading history. This can be expressed mathematically for N step changes of stress as:

$$\varepsilon(t) = \sum_{i=1}^{i=N} \sigma_i \left[\frac{1}{E(t - t_i)} \right] \qquad (2.77)$$

where σ_i is the step change of stress which occurs at time t_i.

In the open literature, superposition rules relating to time (t) and temperature (T) has been applied to rheological functions such as creep compliance and stress relaxation in instrumented indentation studies [95, 96]. The superposition rule suggests that a rheological function F(t,T) at temperature T when shifted by a shift factor a_T parallel to the time t-axis is accurate to be superimposed on $F(t,T_o)$ at an arbitrary reference temperature T_o. This implies that the temperature dependence of rheological function F(t,T) can be expressed by a normalised temperature dependent dimensionless time $t/\tau(T)$ such that f(t,T) is equivalent to $f[t/\tau(T)]$. This characteristic time $\tau(T)$ controls the temperature dependence of the shift factor and the shift factor $a_T = \tau(T)/\tau(T_o)$. In the work by Saki et al. [95], the characteristic time $\tau(T)$ represented the relaxation time in stress relaxation processes, and the retardation time in creep deformation. From their experimental work on soda-lime glass tested at different temperatures below and above the glass transition temperature, a load-displacement master curve could be established using the time-temperature superposition principle. In the nano-indentation work of Shimizu et al. [96] on amorphous Se, time-temperature, penetration depth-temperature and penetration depth-penetration rate superpositions were used to yield relaxation modulus and creep compliance function.

In the present study, the creep data is modelled using Maxwell-Voigt elements and the parameters determined using curve fitting (this will be discussed in more detail in the experimental section 3.4.3.2). As a first approximation, the creep displacement as a function of time could then be extrapolated for the duration of unloading. Note that although the stress (and thus strain) state would be different during unloading compared to the maximum stress and strain experienced during creep, if the

unloading rate is sufficiently fast, the delayed response from the maximum load will still be present even after prolonged time. This is reflected in the persistent creep effects observed, even after prolonged holding time at maximum load, for soft compliant polymeric materials, indented using a sharp indenter, or near the glass transition temperature. By extrapolating the creep event for the duration of unloading, the creep displacement at each time interval during unloading can be approximated. This displacement can then be subtracted from the actual displacement data, to yield a revised load-displacement point whereby the creep component in the indenter penetration is minimised. In this way, a new unloading curve devoid of creep effects can be established, and unloading stiffness and elastic modulus can then be estimated using the Oliver and Pharr method.

It should also be stated that the superposition principle is applicable only for materials that exhibit linear viscoelasticity. The method to determine linear viscoelasticity will be discussed in the experimental section 3.4.3.2.

2. 7 Summary of thesis

2.7.1 Overall Aims

The overall aim of this work is to examine depth-sensing instrumented indentation as a rapid means to obtain elastic properties of industrial paint systems for the possible future development of an on-line quality control system.

2.7.2 Specific Objectives

1. To evaluate micro-/nano- indentation methods using commercial depth-sensing indentation instruments on a reference polymer (polystyrene) and a number of different paint coatings. Specifically, repeatability of the results and the sensitivity of the indentation test in generating results that could differentiate different paint qualities (in terms of different degrees of cure and different pigment/filler contents) must be established. The effect of micron-scale surface roughness in the sample on the modulus results obtained must also be evaluated.
2. To evaluate the applicability of the elastic contact equations used to analyse the force-penetration depth data generated using depth-sensing instruments for the reference polystyrene sample as well as for different paint coatings.
3. To examine the extent to which creep occurs during indentation and its effect on the results obtained using elastic contact equations. Should creep be an issue, methods to eliminate creep are to be evaluated such that the elastic contact equations could still be applied.
4. In the event that creep could not be eliminated from the force-penetration depth data, mechanical elements commonly employed (in terms of springs and dashpots) to model creep events in polymers and other viscoelastic solids are to be evaluated, for the estimation of elastic modulus.
5. To specify, from the results, specifications for an ‘ideal’ indentation instrument for on-line QC of paint coatings.

2.7.3 Outline of Methodology

The methodology used in this work is outlined in the flowchart below:

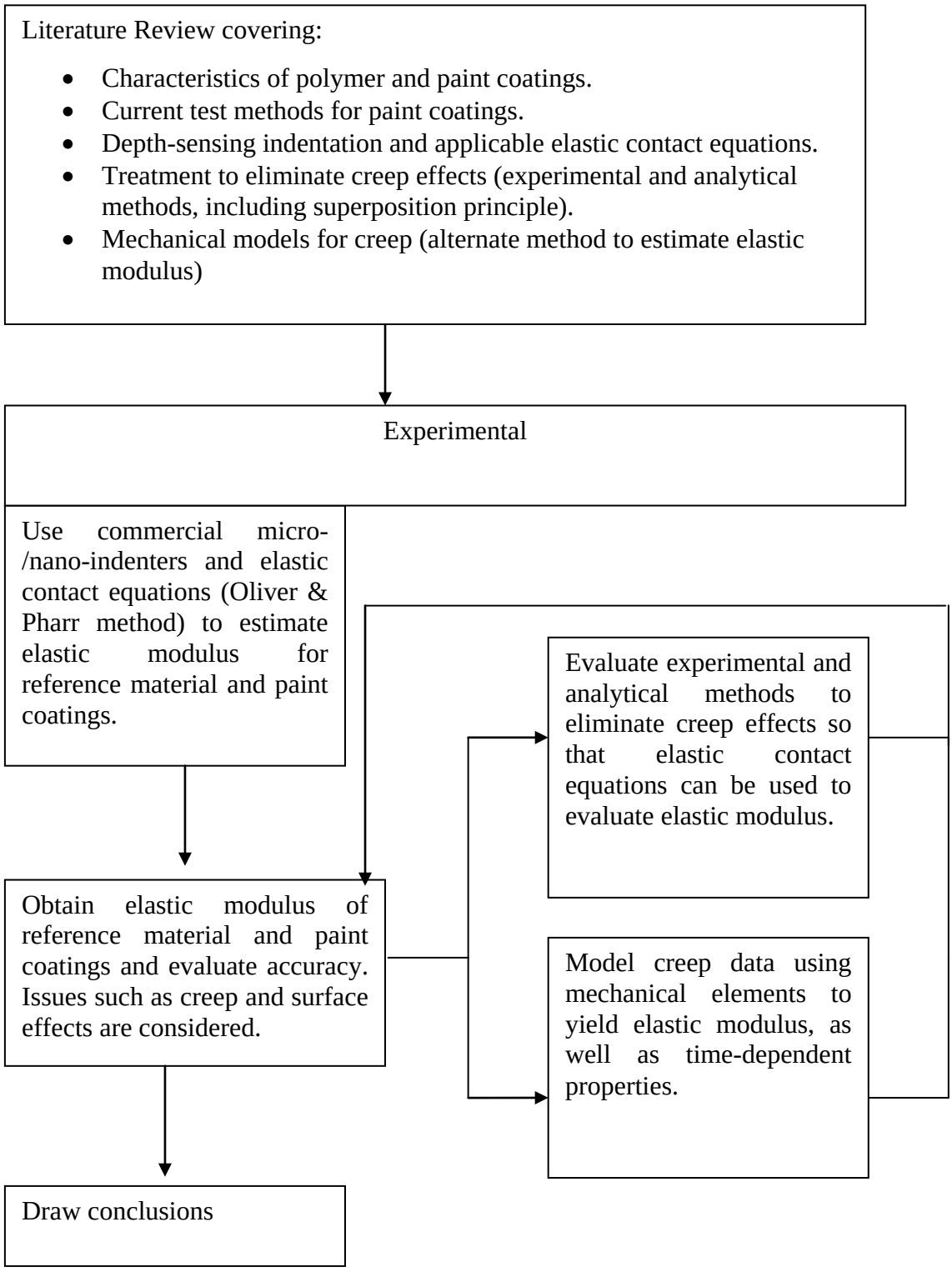

2.7.4 Identification of novelty

Elastic modulus can be directly linked to the degree of crosslink in polymer systems. Depth-sensing instruments allows indentation tests to be performed quickly (each test typically takes only minutes and no special sample preparations are required) thus the method has the potential to be used as a rapid quality control tool. The analytical methods, such as those devised by Oliver and Pharr, are based on elastic contact equations applied to the unloading part of the load-displacement data, thus the issue of creep renders the analyses inaccurate for the determination of modulus. A simple method is proposed in this work based on curve fitting of the creep data to establish creep displacement as a function of time. After establishing linear viscosity, the Boltzmann's superposition principle allows for the creep displacement to be subtracted from the original unloading displacement data, thus more accurate elastic modulus values could be obtained. The method is simple to apply and could readily be incorporated into indentation testing routines for quick assessments of elastic modulus values. Finally, from the results recommended requirements for an "ideal" instrument suitable for thermo-mechanical testing of paint coatings could be formulated.

2.7.5 Outline of thesis chapters

2.7.5.1 Introduction

This chapter introduces the need for a rapid quality control method for industrial paint coatings. Elastic modulus could be related directly to crosslink density and thus would be a good indicator to highlight production problems affecting the curing of

paint coatings. Micro- and nano-indentation methods are introduced as a rapid means to provide elastic modulus values and they are suitable for the testing of thin coatings. However these are commonly used to test hard materials since for more compliant materials, the issue with creep would affect the values attained as the elastic contact equations used in the analysis of the indentation data would no longer be applicable. Methods to minimize the effect of creep are mentioned, as are the use of mechanical elements (springs and dashpots) to model creep as a means to obtain the elastic modulus.

2.7.5.2 Literature Review

The following topics are covered in this chapter:

- Characteristics of polymer and paint coatings.
- Current test methods for paint and paint coatings.
- Depth-sensing indentation and applicable elastic contact equations.
- Models to describe creep using mechanical springs and dashpots, and attempts to obtain modulus values from these models.
- Treatment to minimise creep effects (experimental and analytical methods, including superposition principle).

These topics introduces the soft compliant nature of the materials being tested, specifically the tendency for creep under stress. Common methods for paint testing and paint coating testing surveyed indicated a need for a new test for industrial quality control purposes. The available literature showed that depth-sensing indentation methods were commonly used for rapid testing of thin film materials,

mostly hard metallic and ceramics, while those performed on compliant polymeric materials showed substantial creep. Nano-indentation testing of paint films and polymer coatings were predominantly scratch tests, which yielded qualitative results. No open literature was found on indentation tests of paint coatings using the elastic contact methods. Treatments to minimize creep effects were covered. These included experimental (hold time at maximum load in order for the effect of creep to saturate, before unloading) and analytical (method of Feng and Ngan). The concept of Boltzmann superposition was introduced, which would provide a means to 'eliminate' creep effects in the displacement data in the unloading event.

2.7.5.3 Experimental

Polystyrene was selected as a reference material because of its known properties, so that the accuracy of the indentation method and the applicability of the various creep models could be examined. Since the paint coatings have their T_g close to room temperature, the reference polystyrene was also tested at high temperatures up to its T_g. The paint coatings selected from the production line ranged from the stiffest (white) to the most compliant (black), with brown having intermediate stiffness. White coatings were made in the laboratory to various degrees of curing and to two thicknesses. A clear coat with no pigments was also made to examine the paint matrix.

Section 3. 2 describes the commercial UMIS-2000 system used for testing of the polystyrene and the paint coatings. Test cycle used including a hold time at maximum load (to saturate creep effects) was specified. The methodology used was

stated as follows: first repeatability of the method was to be carried out on the reference polystyrene, using the Berkovich indenter to perform a set of five indentations. Secondly, surface roughness effects were to be investigated on polystyrene roughened with P400 SiC paper, indented using the Berkovich indenter, for direct comparison with results obtained in the repeatability test. Indentation using spherical indenters and the Field and Swain load-partial unloading method, which enables E* to be determined at increasing depths, was also described for polystyrene samples with a 3μm and a 6μm surface finish.

White paint coatings with different degrees of cure, and different colour coatings were to be tested to examine the sensitivity of the micro-indentation technique in obtaining significantly different modulus results. The effect of indenter geometry (Berkovich vs. spherical) and the two modes of operation, viz., continuous loading and load-partial unload, were also to be examined using reference polystyrene and a clear coat (to minimize surface roughness effects).

Section 3. 3 describes the experimental methodology for the nano-indentation work using a commercial AFM (Digital Instrument Nanoscope) as well as a home-built AFM type equipment, the force-rig, which allows the user to specify a holding period before unloading. Testing was to be carried out on a reference polystyrene sample and a black and a white paint-coated sample. The operation of the force rig was described in some detail in this section. Technique to convert the force plots (plot of cantilever deflection vs. piezo travel) to a force-indentation depth plot is described.

Experimental methods to study the effect of creep in indentation are described in section 3. 4. Creep effects are important as the T_g of the paint coatings being tested are around room temperature, hence the model material polystyrene was to be examined at high temperatures up to its T_g (from 40^oC to 115^oC) . Since the UMIS system employed did not have a heating stage, a commercial DMA with a heating chamber was to be used, with a spherical indenter. The indentation modulus results were to be compared with those obtained using 3-point bend test. Creep models (EVEV and Fischer-Cripps) would also be examined as an alternate means to obtain elastic modulus values from polystyrene as well as paint coatings. From the creep models, time dependent properties could also be obtained. Analytical methods (Feng and Ngan, as well as the Boltzmann superposition principle) would also be examined as a means to eliminate creep effects from the unloading curve in the force-indentation depth plot so that the Oliver and Pharr method could be applied to yield modulus values.

2.7.5.4 Results

This chapter presents results obtained from each subsections as described in the experimental chapter. Section 4.1 shows the results for the UMIS work. Testing on polystyrene showed that the method yielded repeatable results, provided surface roughness was not an issue. Surface roughness affected the modulus values obtained by affecting the overall indentation-depth due to asperities loading, but did not affect the unloading slope of the force- indentation depth plot greatly. The load-partial unload module yielded modulus values at increasing depth of penetration. An interesting outcome was that asperities height and hence surface roughness could be

inferred by examining the penetration depth above which the modulus values became more or less constant. Micro-indentation using the UMIS system was sufficiently sensitive to yield significantly different modulus results for paint coatings having different degrees of cure, and pigment/filler contents. The white paint coating having optimum curing showed the highest modulus value, as expected. The modulus results also decreased with decreased pigment contents, thus white paint coating showed higher modulus value than the brown paint coating, for the samples obtained from the production line, and white paint coating showed higher value than the clear coating, for the samples coated in the laboratory. Using a spherical indenter, the UMIS results from the two operating modes, viz, continuous loading (CL) and load-partial-unload (LPU), on polystyrene showed that the LPU mode sometimes gave slightly lower modulus results, mainly due to the LPU mode using only two data points to determine the slope of the unloading curve. For the clear coating, CL also gave slightly higher modulus values than the LPU mode. For polystyrene higher indenting loads gave higher results closer to those obtained in the repeatability test, mainly due to surface roughness effects (asperities loading).

Attempts to generate force-indentation depth plots using the AFM and the ‘force-rig’ are shown in Section 4.2 Using the AFM, which did not allow for holding time before unloading, creep effects were evident even on polystyrene, causing a ‘nose’ in the unloading slope. The ‘force-rig’, on the other hand, allows a holding period to be specified. However, results on the black paint coating showed large scatters in the cantilever deflection data, as well as a gap in the initial portion of the unloading slope. This missing portion was attributed to creep effects that allowed the indenter to continue sinking into the material even after the load has been removed. This sink-

in caused a decrease in cantilever deflection; hence the unloading curve started at a lower cantilever deflection value than at the end of loading. Unfortunately, the combination of high stresses generated by the sharp cantilever tips and the compliant polymer materials being tested would mean that creep would also be a serious issue, hence further testing was abandoned.

Section 4.3 deals with the issue of creep in indentation. In section 4.3.1 the results for high temperature testing of polystyrene was presented. After area correction, the indentation modulus results compared favourably to those obtained using the 3-point bend test (Figure 4.22), although the T_g was slightly lower in the case of indentation. In section 4.3.2 the modulus results obtained for polystyrene as well as for the paint coatings, using the EVEV creep model, are presented. These results are in general higher than those obtained directly from UMIS, using the Oliver and Pharr method. Modulus results obtained using the Fischer-Cripps creep model was also presented for polystyrene tested at high temperatures and compared to those obtained using the Oliver and Pharr method. The modulus values for both methods were similar up to 80^oC. At temperatures near T_g (100^oC to 115^oC), the Oliver and Pharr method (UMIS) gave higher modulus values, due to creep effects. In addition, creep models yielded information on the time dependent material properties, in terms of viscosity coefficient and retardation times. The Feng and Ngan method could not provide any significant correction to creep effects on the unloading slope, for polystyrene tested at high temperatures. On the other hand, the Boltzmann superposition principle provided significant correction from 80^oC to 110^oC. Above T_g, at 115^oC, there was no significant improvement.

2.7.5.5 Discussions

This chapter presents an overall discussion to the main findings. In section 5.1 the applicability of indentation testing using commercially available ultra-micro indentation systems is discussed. The method could yield accurate and repeatable modulus values for less compliant polymers such as polystyrene, provided that asperity loading due to surface roughness was not present. For paint coatings, two issues were apparent: first, the inherent surface roughness (in micron scale) and second, the low T_g close to ambient temperature, causing creep. However, the method was sufficiently sensitive to yield modulus values which reflected differences in degrees of cure and pigment/filler contents. It can thus be proposed that using spherical indentation at the same loading conditions (5mN @2.5mN/s) instead of a sharp indenter, in a low temperature controlled environment (for example 10^{o}C), and using suitable holding times, quantitative modulus results could be obtained. By controlling and lowering the testing temperature, the large standard deviations observed when the Berkovich indenter was used (of over 20% of the modulus values) for paint coatings should be significantly reduced. Standard deviations could be further reduced through examination of individual force-indentation depth to identify the presence of asperity loading. Should this occur, the results should be discarded or rectified by subtracting the displacement due to asperity loading, prior to analysis using the Oliver and Pharr method.

Section 5.2 notes the issue of creep presented in nano-indentation testing using commercial AFM and the home-built ‘force-rig’. Even with the in-house-built ‘force-rig’ equipment which allowed for a holding time, the nature in which the force data

was generated was not suitable for materials which would undergo creep. This problem occurred as the indenter attached to the cantilever sinks into the material due to creep, the deflection recorded via the position of the laser spot would change accordingly.

High temperature indentation test on polystyrene in section 5.3 showed that the indentation method was successful in obtaining T_g and elastic modulus values in the reference bulk polystyrene material which were comparable to those obtained using a conventional three-point bend test on the same equipment, although at temperatures around T_g, the modulus appeared slightly higher with the indentation method. This could largely be due to increased creep effects at these temperatures.

The merits of the mechanical creep models examined were discussed in section 5.4. Although both the EVEV model and the Fischer-Cripps model yielded similar results for polystyrene, the EVEV model could not be applied for paint coatings, whereas the Fischer-Cripps model yielded believable results for the clear coating. This was mainly due to excessive creep giving rise to the steep unloading slope of the force-displacement curve. The Fischer-Cripps model thus worked better than the EVEV model and the Oliver and Pharr method where creep effects could not be sufficiently diminished using a holding time at maximum load. This section also provides a discussion on the analytical methods used to ‘correct’ for creep effects which may still be present during unloading, even after a holding time was applied before the unloading event. The Feng and Ngan method did not provide significant creep correction to the apparent contact compliance for polystyrene as well as for the black paint coated samples tested at temperatures close to T_g. However, the application of

the Boltzmann Superposition Principle was successful in providing significant correction for bulk polystyrene over a range of temperatures from 80^{o}C up to $T_{g.}$

2.7.5.6 Conclusions and Recommendations

It was concluded that indentation testing using commercial systems such as the UMIS 2000 could yield repeatable modulus results for polymeric materials provided that asperities loading due to surface roughness is limited, or the asperities could be pressed down readily. The method could yield reliable modulus values if testing was carried out below T_g. Thus for paint coatings, the method would provide reliable results if creep responses could be limited. This could be achieved using a spherical indenter with low loads and at low temperatures, for example 10^{o}C or lower. Where creep effects could not be totally eliminated, two methods could be employed. Firstly, mechanical creep models could be used to estimate elastic modulus as well as provide time-dependent properties. In this regard, the Fischer-Cripps method was found to be reliable. The second method made use of the Boltzmann superposition, whereby the creep displacement in the unloading event could be subtracted so that the Oliver and Pharr method could be used in yielding reliable modulus results.

Commercial indentation systems could be used for rapid quality control testing for pigmented paint coatings, provided that creep effects could be eliminated. Therefore, it is proposed that spherical indentation at low loads with fast loading rate (5mN @ 2.5mN/s) and a low temperature controlled environment (for example 10^{o}C) be used, with suitable holding times. Furthermore, standard deviations could be significantly reduced by discarding or rectifying load-indentation depth plots showing asperity

loading. Finally, from the results recommended requirements for an “ideal” instrument suitable for rapid thermo-mechanical testing of paint coatings was formulated.

3 EXPERIMENTAL

3. 1 Material

Polystyrene was used for reference to gauge the accuracy of the methods used in obtaining elastic modulus results, by comparing the results obtained to those found in open literature. The polystyrene material used for reference was prepared by compression moulding polystyrene granules in a hot press at 165^{o}C to obtain 3mm thick platelets. The granules were supplied, under the trade name of Austrex 103, by Polystyrene Australia. The sample used for reference was polished to a 1μm surface finish, without any intermediate grinding and polishing steps.

Industrial paint-coated steel samples were obtained from Bluescope Steel, Australia, under the trade name of Colorbond. Brown, black and white coatings were provided. The paints were melamine-crosslinked polyester of approximately 18-20μm thickness. Samples were also made in the research laboratory at Bluescope Steel. White paint coating as well as an unpigmented polyester clear paint was made to approximately 18μm. In addition, a thicker 24μm white paint coating was made to different degrees of cure. The white paint used was the same as that used on the industrial paint-lines. The clear paint was obtained for research purposes from the same supplier as the pigmented paints, and should represent the base paint without any pigment/filler additives. Paint coatings were deposited onto steel or aluminium substrates using “drawdown bars”. The pitch of the drawdown bar determines the final coating thickness, in microns, which is approximately twice the number in bars.

For example, a number-18 bar would yield a coating thickness of approximately 36μm.

The laboratory coatings were baked in preheated ovens for a predetermined time to generate a peak metal temperature (PMT) of 230^{o}C. From production history, this temperature was deemed to yield optimum curing of the paint coating, resulting in the optimum mechanical properties. To evaluate the sensitivity of micro-indentation technique in detecting varying degrees of curing, white colour paint coatings were cured in the laboratory at differing times to yield different equivalent PMTs.

3. 2 Ultramicro-indentation – UMIS 2000

3.2.1 The UMIS 2000 system

The UMIS 2000 system (CSIRO Australia) is a ‘force-driven static measuring’ ultra micro-indentation instrument specially designed for the investigation of mechanical properties at near-surface regions of materials; and is therefore especially useful in determining mechanical properties of thin coatings. It is ‘force-driven’ in the sense that the indenter is driven into the surface until a resistance equal to a set force is met. It is ‘static measuring’ in the sense that penetration is measured under conditions of force equilibrium at each force step.

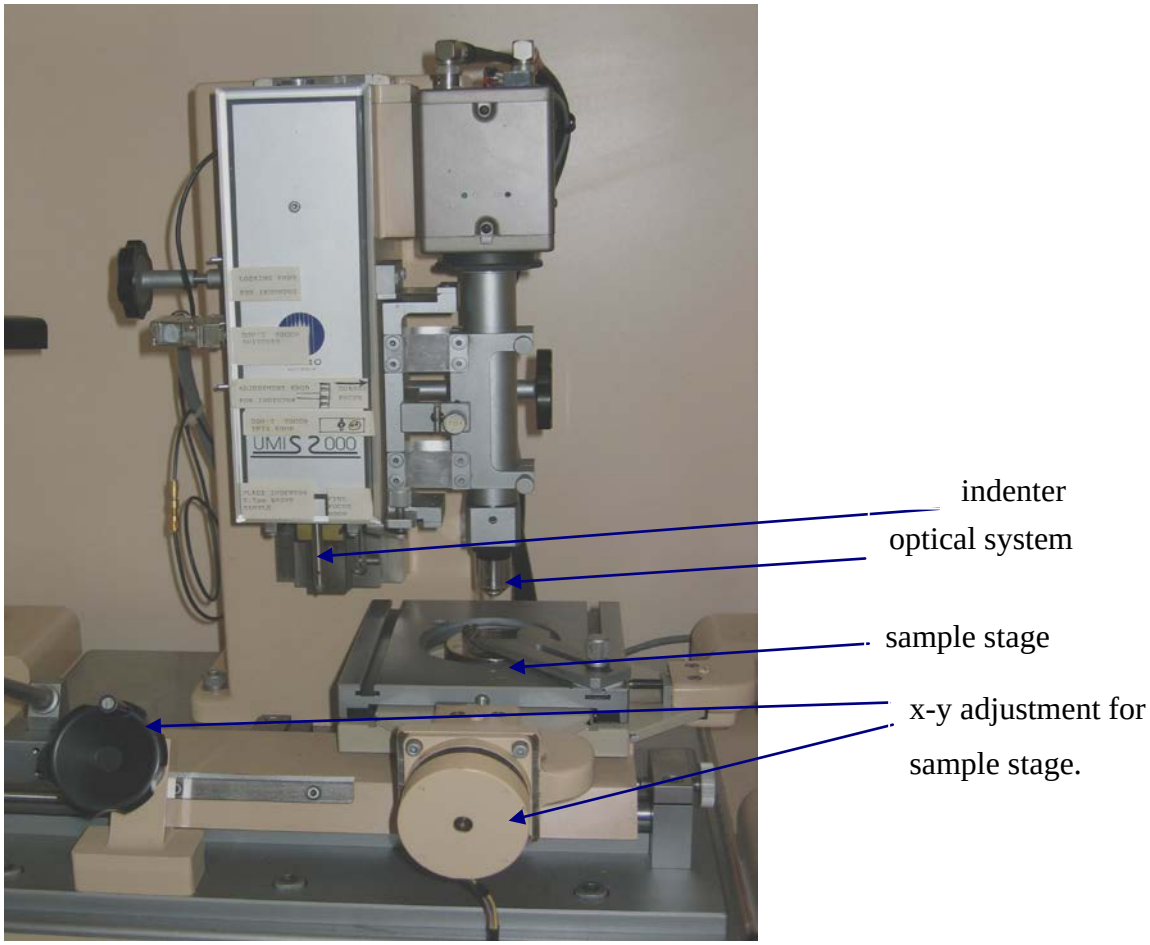

Figure 3.1: UMIS 2000 system.

The commercial UMIS 2000 system used in the experimental work is shown in Figure 3.1. Its basic components consist of an optical imaging system and an indenter column. The sample is placed on a holder on a positioning stage such that after selecting a suitable site for indentation using the optical microscope system, the sample can be moved by lateral movement of this stage, to a position under the indenter for indentation to take place. Force and displacement are measured by means of LVDTs as shown schematically in Figure 3.2. A feedback system ensures

precise control over the force. The force and displacement resolution for the equipment is given by the manufacturer as 0.025μN and 0.003μm, respectively.

Two modes of operation are available:

- Data requisition by continuous load cycle.
- Data acquisition by load partial-unload cycle.

Both methods can produce data with either a ball (sphero-cone), diamond pyramid or other indenter but the analysis package employed was limited to the use of the ball indenter for the partial unload. The indenting mechanism operates under the control of a computer program and requires only the appropriate software to perform either data acquisition sequence. Data acquisition refers to the collection of output data in terms of force and indenter depth of penetration.

The numerical output of interest from both modes is the composite elastic modulus, E*. Hardness results can also be obtained.

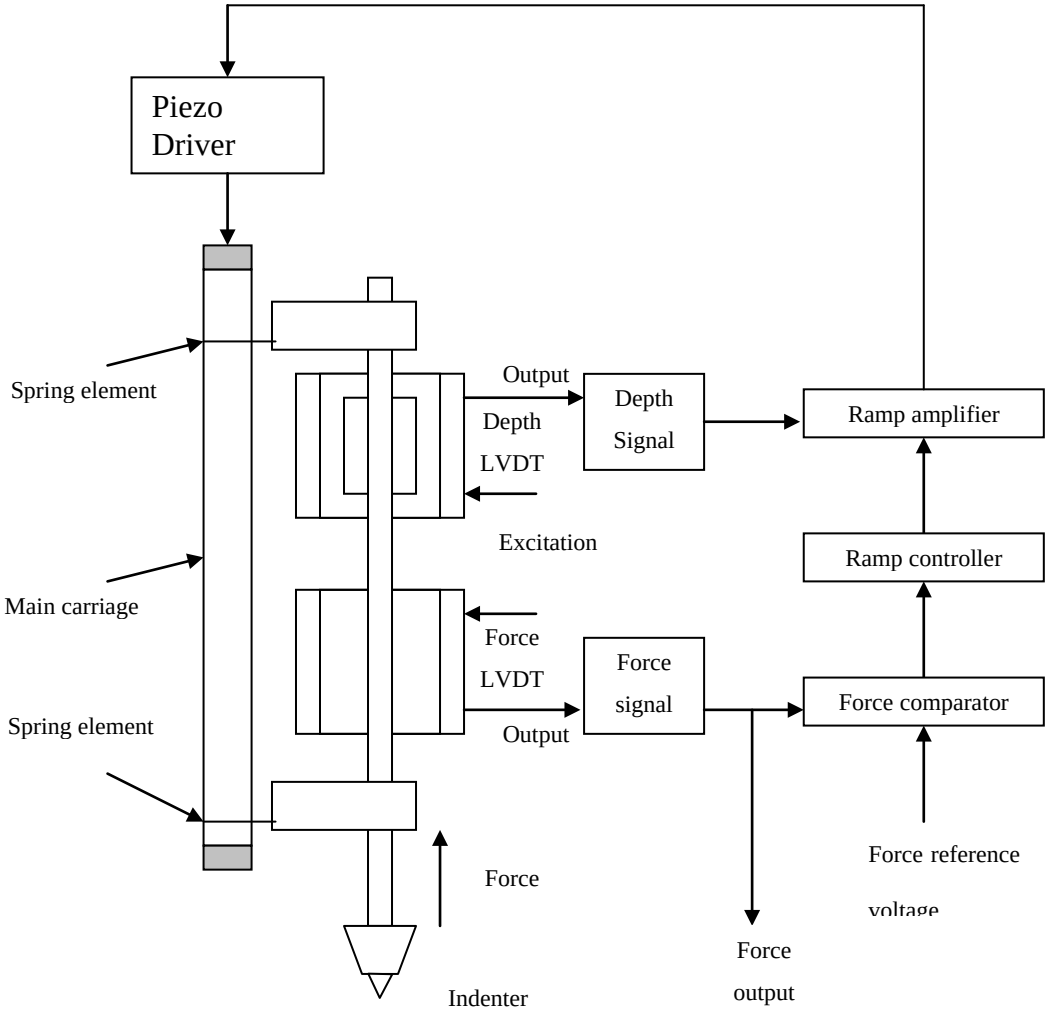

Figure 3.2: Schematic illustration of the basis of UMIS system [40].

3.2.2 Specimen preparation

A reference polystyrene sample as well as some painted steel samples was examined using micro-indentation tests. Different types of paint coating, made in the laboratory; as well as from production, were tested without further surface preparation. Grinding and polishing were deemed impractical on the thin paint coatings, and also because of the potential for the pigment/filler particles to pull out of the paint matrix.

Initially, the experimental work to evaluate the effect of surface roughness was carried out on a reference polystyrene sample (roughened using grade P400 silicon carbide grinding paper) with the Berkovich indenter, using the UMIS system at the University of Wollongong. However, it was recognised that the surface roughness effect could be directly observed by determining the elastic modulus values at progressively larger depths of penetration. Indentation test using the 'load-partial unload' procedure would provide a rapid means of obtaining elastic modulus values at increasing penetration depths. However, for this test procedure, spherical indenters are required. A variety of indenters of different sizes were available on the UMIS 2000 system, at the University of Sydney, where the load-partial unload procedures were undertaken. For testing using the spherical indenters, the reference polystyrene samples were ground and polished to a 3μm and a 6μm surface finish.

Specimens were cut into flat coupons of about 1cm by 1cm and hot mounted on a magnetic sub-base using heat-softening wax; or cold-mounted by using suitable glue. The surfaces to be tested were clean and dust-free.

3.2.3 Technique

As mentioned earlier in the literature review, a practical method to reduce the effect of creep was to allow a holding period at maximum load such that the creep effect can saturate, before unloading. For the polymeric materials tested in this work, especially with the Berkovich indenter, creep effects were significant and resulted in a ‘nose’ or negative unloading slope at initial unloading. The holding time was found experimentally using reference polystyrene and was set just sufficiently long to counter the effect of creep, but not too long as to render the test impractical or to cause potentially large errors due to fluctuations in ambient temperature. The 10 minute hold was found to work well for all of the material been tested. . Using the 10 minute holding time the creep displacement for ambient temperature indentation of polystyrene was sufficient for the creep rate to decay such that the creep displacement in 1 minute is less than 1% of the total displacement, as recommended Chudoba et al. [97]. For the more compliant clear coating, testing was carried out at around 16^{o}C with a reduced maximum load (1mN). At ambient temperatures above 20^{o}C, the creep effect was not sufficiently saturated even at much longer holding times. The pigment and filler particles in the paint coatings probably help to redistribute the stress and ‘dampen’ the effect of creep. For the clear coat, a lower testing temperature as well as reduced maximum load was required to decrease the creep response to an acceptable level.

The first part of the experimental work was carried out on reference polystyrene to determine the accuracy, reproducibility; as well as the effect which surface roughness has on the results. Using the 10 minute holding time, the modulus of the reference polystyrene was found, using equation 2.4, to be 3.8 ± 0.0 GPa. This result

is in line with those quoted in the literature [104] as detailed in section 4.1.1. The second part of the experimental work conducted on different types of paint coatings was designed to establish the sensitivity of the technique in differentiating varying pigment/and or filler contents of the surface paint layer; and in detecting differing degrees in curing. Lastly, the effect of indenter geometry and the associated analysis methods were evaluated using reference samples as well as a clear paint coating.

Most of the experimental work was performed with a diamond Berkovich indenter, using the following set-up:

- A maximum load of 5mN. A small load was used to minimise substrate effect on the coated samples. In general, the penetration depth should not exceed a tenth of the coating thickness [98, 99].
- Twenty increments of loading and unloading steps, respectively.
- Holding time at each step of 10 seconds and a longer holding time of 10 minutes at maximum load. The holding time was designed to allow for delayed loading response due to viscoelastic effects.
- Indentation was set at 50μm apart from the closest one.

In order to minimize error due to thermal effects, after the experiment has been correctly set-up, i.e., the testing parameter has been entered and the correct working distance set with the help of the software, the sample was left in the enclosed sample chamber for one hour prior to commencement of the indentation test. This time delay was used to ensure minimal thermal differential between the sample and the indenter probe, and for establishment of thermal stability. The time delay was set using the equipment's software.

Repeatability tests were conducted on reference polystyrene to establish the reproducibility of the technique. A set of five indentations was carried out, using the Berkovich indenter.

Surface Roughness effects had to be established since the pigmented paint coatings could not be polished prior to testing. The experiment was carried out using different types of indenters - the Berkovich indenter, as well as tungsten carbide spherical indenters having radii of 250 and 500 μm. The indentation work using the spherical probes was conducted on the UMIS 2000 equipment belonging to the University of Sydney.

Berkovich indentations were carried out on polystyrene roughened with P400 silicon carbide paper. Five indentations were made and the results were directly compared to those obtained in the repeatability tests. The experimental work using the spherical probes was done on polystyrene samples polished to 3μm and 6μm, respectively. These results were directly compared to tests carried out on reference polystyrene samples, tested using the 500μm radius probe, at a maximum load of 300mN. For the 3μm surface finish, maximum loads of 300 and 500mN were used for the spherical probe of 500μm radius, while maximum loads of 100 and 500mN were used for the probe of 250μm radius. In the case of the 6μm sample, maximum loads of 100 and 500mN were used for the larger probe, and maximum loads of 300 and 500mN were used for the smaller probe. Three to five indentations were carried out for each set of experiment.

The spherical indentation software employed load partial-unload cycles, to probe and hence determine the modulus values at increasing penetration depths (Figure 3.3). Unloading at each cycle was set at 50% of the load employed for the particular cycle. The analysis software allows for the E* values to be calculated for each unloading cycle, such that a penetration depth vs. E* plot could be generated for each indentation. Surface roughness of the 3 and the 6μm samples were also independently determined by direct imaging using a commercial atomic force microscope (AFM) in tapping mode (Digital Instruments, Nanoscope IIIa). The R_{max} and median depth values were used for comparison. R_{max} was defined as the distance between the highest and the lowest points on the surface. Imaging was carried out using scan sizes of 10μm, 30μm, 50μm and 100μm. From simple geometry, and assuming only total elastic response of the material, and non-deformation of the indenter, the diameter of the contact circle could be determined from the indenter diameter D_i and the penetration h*:

$$D' = 2\sqrt{\left(\frac{D_i}{2}\right)^2 - \left[\left(\frac{D_i}{2}\right) - h*\right]^2} \qquad (3.1)$$

The value D' could be used as a rough estimate to determine the AFM scan size most suited for comparing the AFM-measured roughness with the UMIS results.

It was noted that the regions being scanned were not always perfectly level, and a flattening operation was performed on the images. Debris was occasionally observed on the surface, giving rise to high peaks in the height image. Such images were excluded from the roughness analysis.

Sensitivity of the technique was evaluated using Colorbond samples of varying pigment/filler contents as well as varying degrees of cure. Different pigment types and contents gave rise to the different observed colours in the paint coatings. In the experimental work, brown and white coatings were obtained from production line samples; while white and clear coatings were made in the laboratory. The white paint contained the highest amount of pigment/filler whilst the clear coatings have no pigment/fillers at all. Coatings with different degrees of cure were made in the laboratory by controlling the peak metal temperature (PMT). This is the temperature which the substrate metal attains before the paint coating is cooled by quenching with water. Altering this temperature will thus change the curing temperature of the paint coating. Since the optimum PMT used in production was at 230^{o}C, the PMTs used in the experimental work ranged from 185^{o}C to 257^{o}C and all coatings used for this part of the experimental work were made in the laboratory using a white paint.

Effect of Indenter geometry and the different applicable analytical methods used were examined using a 100μm radius spherical diamond probe on polystyrene and clear coating samples. Both the continuous loading (CL) and the load-partial-unload indentation (LPU) modes were used. The results were analysed using the Oliver and Pharr method for the former mode, and the Field and Swain method for the latter (refer to sections 2.4.3.1 and 2.4.3.2). The modulus values obtained were compared with those obtained using the Berkovich indenter, in the continuous loading mode, and using the Oliver and Pharr analytical method.

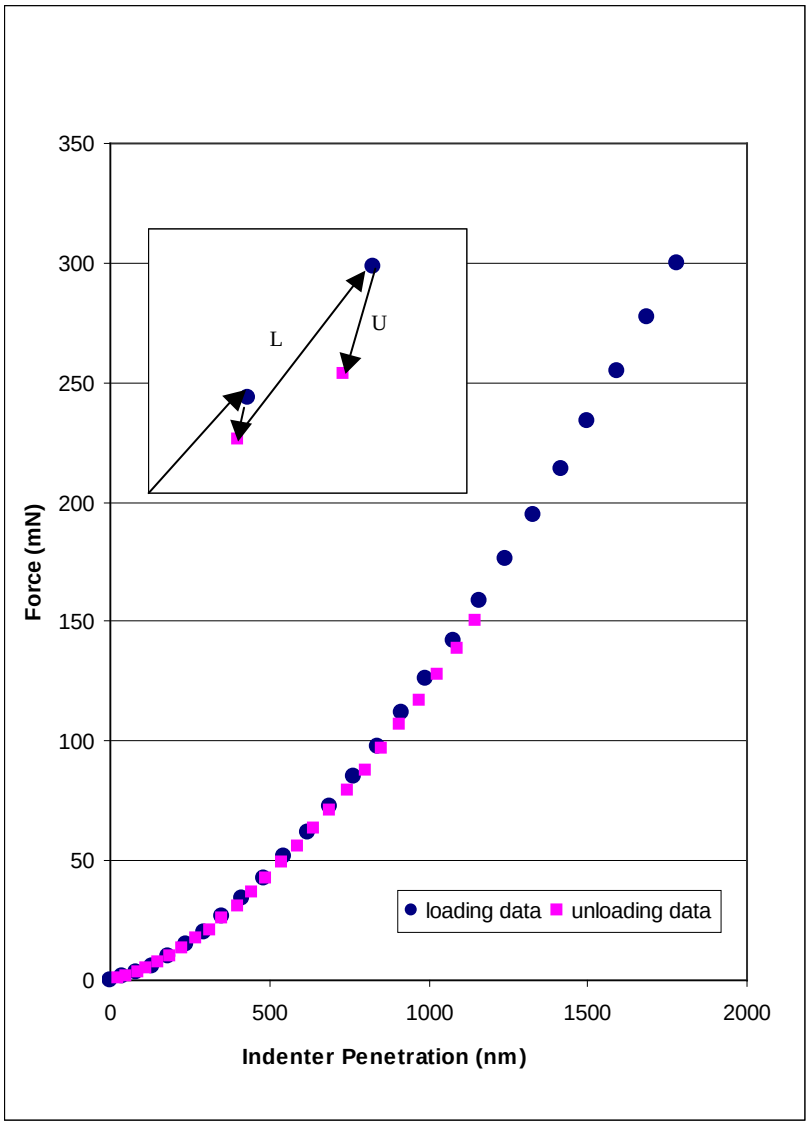

Figure 3.3: Typical plot generated from progressive loading-partial unloading cycles from an indentation test on polystyrene. The inset schematically illustrates the loading (L)-partial unloading (U) procedure.

3. 3 Nano-indentation

From the literature review, it was shown that nano-indentation techniques have been used with some success in biological and polymeric materials to yield mechanical properties. However, the use of nano-indentation on paint systems containing hard

particles has not yet been investigated. The closest material system found in open literature for a polymer film containing small hard phases was that of single-wall carbon nanotube cast into polyelectrolyte to form a nanocomposite film [100]. In this work the relaxation modulus was found by analysis the loading curve in indentation tests for a number of composite films containing varying amounts of carbon nanotubes. The current experimental work investigates the feasibility of using AFM cantilever tips to probe selective regions in the paint films, such that the elastic modulus of the paint matrix itself can be isolated and determined. Reference polystyrene was used in an attempt to verify the accuracy of the technique.

3.3.1 Sample preparation

For this part of the experimental work, a reference polystyrene sample, as well as a black and a white paint-coated sample were used. The paint-coated samples were cut using a mechanical precision cutting wheel. During cutting the samples were clamped in such a way that the surfaces of the samples to be tested were not inside the clamping jaws so as to avoid damage to these surfaces. These samples were cut to roughly 1cm by 1cm squares, washed in water and air -dried.

3.3.2 Equipments used

The atomic force microscope (AFM) used for this part of the work was the Digital Instrument Nanoscope (Figure 3.4). Typical tapping mode cantilevers (type TESP, supplied by Digital Instruments) having stiffness in the range of 20N/m to 40N/m was used for this part of the experimental work. The probes have a typical tip radius

of less than 10nm. A major limitation of the equipment was that the software did not allow for a holding period at the end of the indentation, before unloading. A home-built equipment was then used with software written to allow for user-specified holding periods [101]. Similar to the AFM, cantilever deflections were detected using a focusable laser diode and a position-sensing device (PSD). Vertical displacement between the sample and the indenting probe was controlled using an Inchworm (Burleigh) motor, which allows for displacement control in steps of 0.5μm. A photograph of the 'force rig' and a schematic representation is shown in Figure 3.5 & Figure 3.6, respectively. The movement of the Inchworm is achieved by expanding and retracting a central piezoelectric crystal (PEC) in the vertical direction while it is sequentially reclamped at each end. A major drawback of the Inchworm is a small jump or 'glitch' that accompanies the reclamping motion. The force rig was hence further modified by adding an external displacement sensor (DSS) to monitor the actual vertical displacement, although the movement control was still carried out using the Inchworm and the accompanied controller. A calibration plot of the displacement sensor system (DSS) is shown in Figure 3.7. The working distance must be preset prior to any indentation experiment to ensure that the displacement output (in Volts) is within the linear range. A plot of displacement as measured by the controller vs. that measured by the DSS is shown in Figure 3.8. It is evident from the figure that an independent displacement measurement is required.

Figure 3.4: Commercial AFM (Digital Instruments Nanoscope).

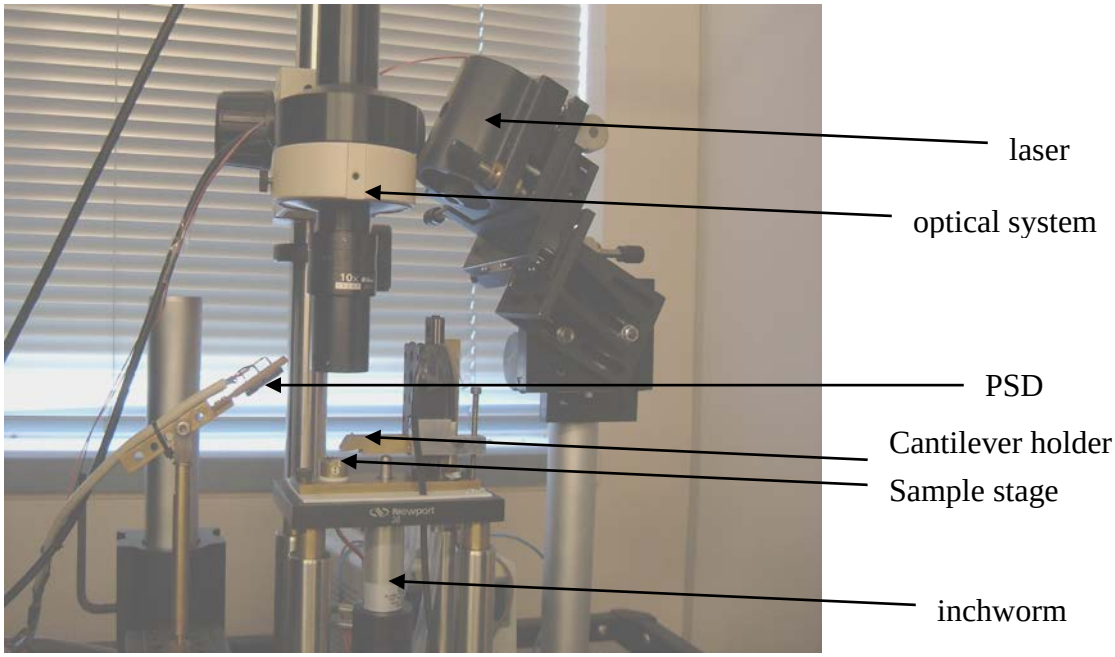

Figure 3.5: The force rig

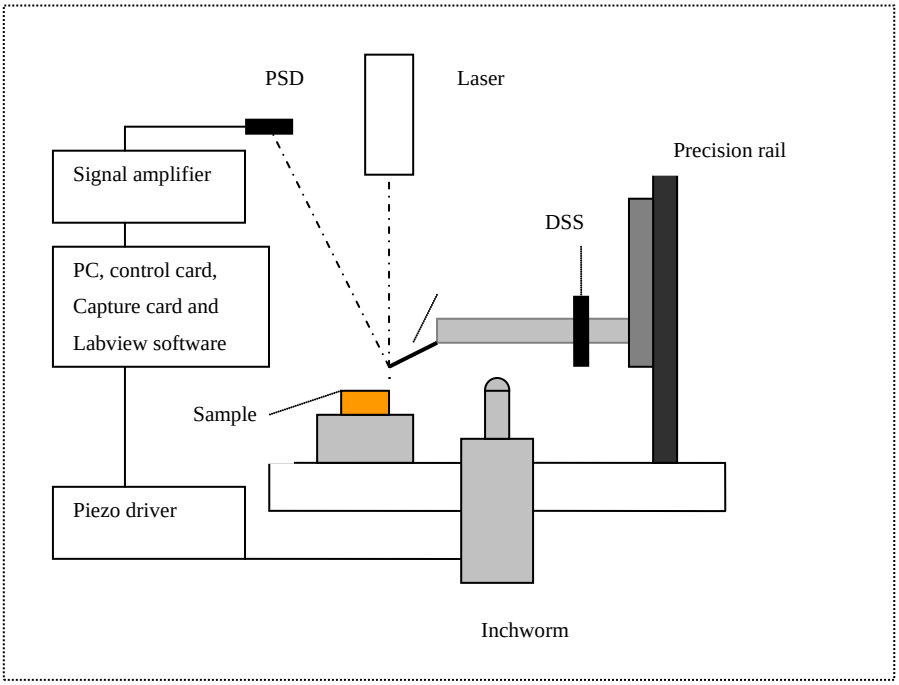

Figure 3.6: Schematic representation of the force rig showing the basic components [101].

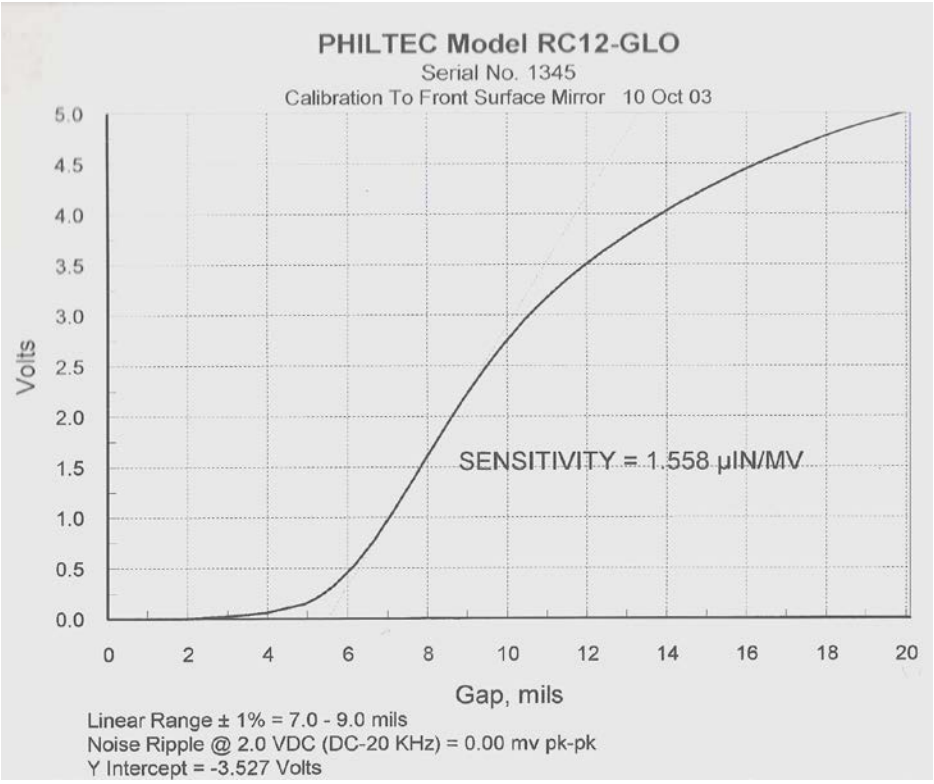

Figure 3.7: Calibration plot for the displacement sensor (DSS), as supplied by the manufacturer.

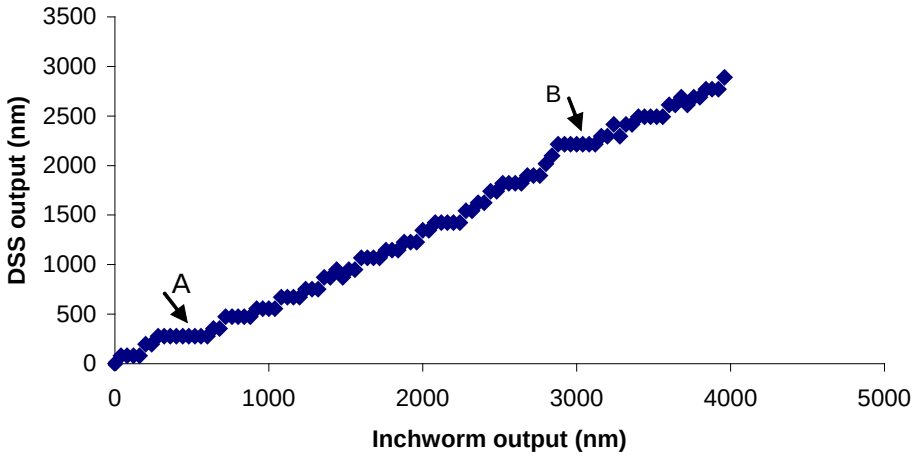

Figure 3.8: Plot of displacement output by the Inchworm vs. that by the DSS from an indentation experiment into silicon (loading curve). A and B show extensive displacement error due to the 'glitch' phenomenon.

3.3.3 Technique

3.3.3.1 Determination of cantilever stiffness

Cantilever stiffness was determined using the mass difference technique [102]. The resonance frequency of a cantilever is determined using the AFM software. Thereafter a known mass is glued onto the probe and the resonance frequency re-established. From the information the stiffness of the cantilever, *k*, can be determined from the following equation:

$$k = (2\pi)^2 \frac{M}{(1/\upsilon_1^2) - (1/\upsilon_0^2)} \qquad (3.2)$$

where M is the added mass, υ_1 is the resonant frequency of the cantilever with the added mass, and υ_0 is the original cantilever resonant frequency.

For the known mass, high purity tungsten spheres were used. A sphere was selected under the optical microscope, and transported using a micro-fibre attached to a micro-manipulator. It was then transferred onto an optical calibration slide for imaging, as shown in Figure 3.9. From its optical image, its diameter and hence its mass could be determined since the density of tungsten is known. The sphere was adhered to the probe by using minute amounts of PMMA. Small grains of PMMA were heated under a microscope using a home-built heater; a droplet of the molten PMMA was transferred using a micro-fibre attached to a micro-manipulator onto the tip of the probe. The sphere was then manipulated into position at the tip of the probe (Figure 3.10).

To remove the sphere, the cantilever is placed in a UV chamber and irradiated for ten minutes, such that the PMMA would vaporize and the sphere would simply drop off the probe.

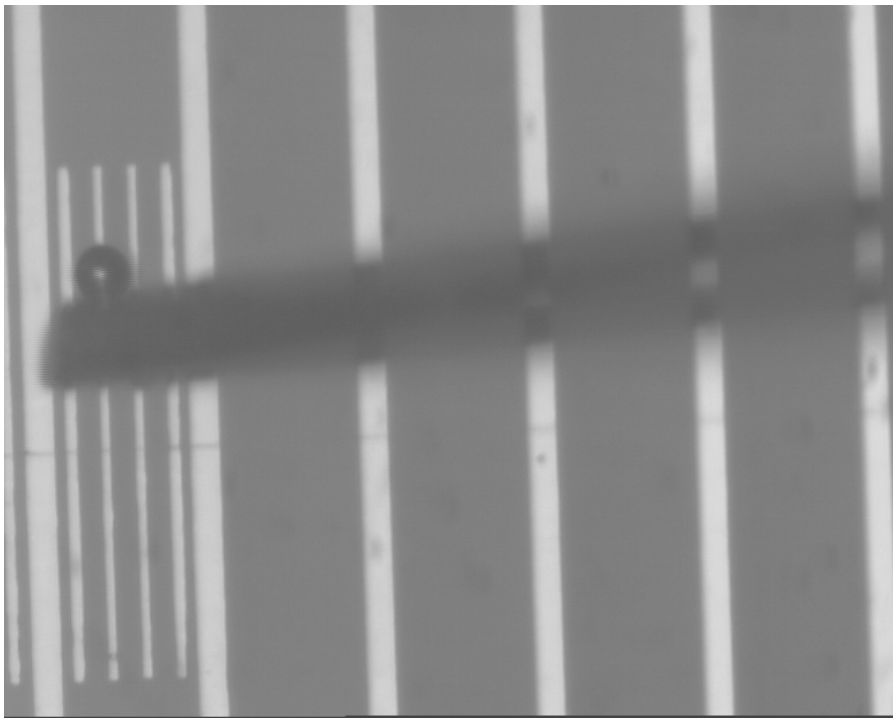

Figure 3.9: Showing a tungsten sphere transferred onto an optical calibration slide using a micro fibre. Small gratings are 20µm apart, and large gratings are 100µm apart.

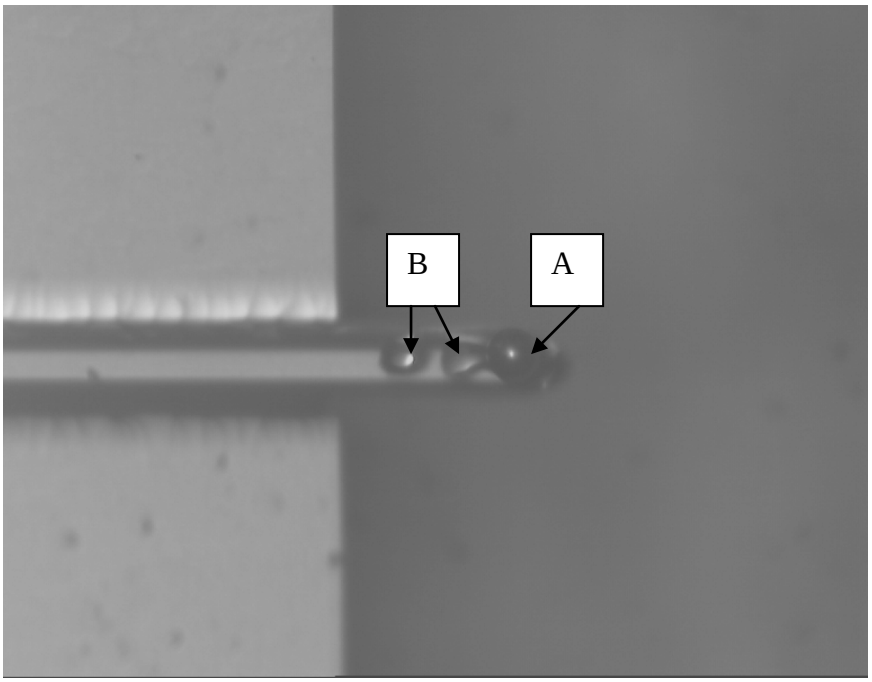

Figure 3.10: Showing a tungsten sphere (A) attached to a cantilever probe. Residual glue (B) is also present on the cantilever.

Force plots were generated using the AFM on a polystyrene reference sample, a silicon sample, a clear coating sample and a black Colorbond sample.

In contact mode, deflection curves were recorded by plotting cantilever deflection vs. z piezo motion with regard to the tip.

The photo detector voltage or displacement change can be calibrated to reflect actual cantilever bending using an 'infinitely' stiff material, in this case Si wafer. Since Si shows negligible indentation at the stresses used in theses studies, the cantilever bending is compensated by the z-piezo travel. The y-axis of the plot, such as shown in Figure 2.4 can then be multiplied by a sensitivity parameter such that the slope of the curve is 1. This sensitivity parameter can then be used to calibrate the plots generated on the samples of interest.

As was mentioned in section 2.5.1, the relationship between the z-piezo travel (Δz_p), the cantilever deflection (Δz_c) and the indentation depth (Δz_i) is given by,

$$\Delta z_p = \Delta z_c + \Delta z_i \qquad (2.31)$$

For silicon, Δz_i is negligible, but for softer samples, Δz_i can be calculated using the above equation, since Δz_c could be obtained from the Si calibration. Once the cantilever spring constant or stiffness, k, was determined, the applied force F can be determined using Hooke's law:

$$F = k\Delta z_c \qquad (2.27)$$

A plot of applied force F vs. indentation depth Δz_i can thus be generated and the effective modulus of the material can in theory be extracted from the unloading slope using the Oliver and Pharr method, or Hertz elastic contact equation, as outlined in section 2.5.1.

In the case of the 'force-rig' a similar procedure was adopted. A deflection vs. displacement (from the DSS output) plot was obtained in voltage. Using the supplied DSS calibration curve, the DSS voltage could be converted into displacement in nm. Care had to be taken in the set-up stage prior to the actual indentation experiment to ensure that the DSS was operating in its linear range. Again, the deflection data could be calibrated and converted to displacement data in nm using Si wafer, using the same procedure as for the AFM data.

3.3.3.2 Data processing

The raw data generated using the AFM and the 'force-rig' was processed using the software IGORPRO. Since the data points for the samples did not always coincide with those for the Si calibration sample, curve-fitting and transposition procedures were carried out such that force-displacement data points (force vs. Δz_i) can be calculated using equations (2.27) and (2.31). This is also illustrated in the schematic below.

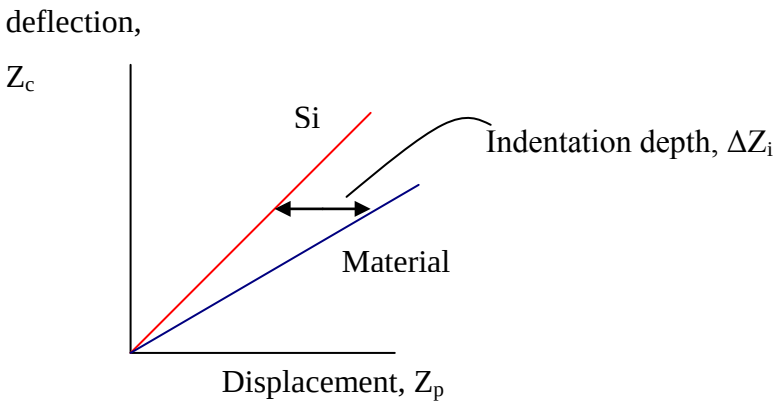

From the schematic above, it is clear that by subtracting the equations of the two curves, a curve describing ΔZ_i at the given Z_c range can be found. Mathematically, it is a simple matter to obtain differences in y-values at any given x-values by directly subtracting two equations. However, in our case it is the differences in x-values at specific y-values that were of interest. To overcome this, one can transpose the x and y values for the two curves, such that ΔZ_i can be directly obtained by subtracting the two curves.

3. 4 Viscoelasticity in indentation

As mentioned previously in the literature review section, creep phenomenon can affect indentation responses and lead to erroneous results when elastic contact equations are used to determine elastic modulus. Although experimentally a holding period prior to unloading can be used to minimise the effect of creep, the method is not always practical, since thermal fluctuations can result during testing and in some

cases excessively long hold times would be required for the creep rate to reduce to an acceptable level. This latter problem is particularly apparent when indentation is performed at temperatures close to the T_g of the sample, such that creep effects cannot be ignored even with prolonged holding periods.

This section is divided into three parts. The first part examines the accuracy of the indentation method at high temperatures (up to T_g for polystyrene) and also at establishing the T_g of the reference polystyrene. The second part examines the use of the various mechanical models used on the creep data to estimate elastic modulus values. Lastly, analytical methods for eliminating creep effects in the displacement data during the indenter unloading event were examined, so that the elastic equations could still be used to calculate the elastic modulus values.

3.4.1 High temperature indentation

The penetration experiments were carried out on reference polystyrene at a range of temperatures in order to establish its T_g. The polystyrene samples were roughly 1cm by 2cm in size and were tested from 40^{o}C to 100^{o}C in 20^{o}C increment, and to 115^{0}C in 5^{o}C increment, using a commercial DMA (model Q800, TA Instruments), as shown in Figure 3.11. The results were compared to those obtained on the same equipment, using three-point bend test through the same temperature range, in order to establish the accuracy of the indentation method in determining the elastic modulus values and in determining T_g. The force was controlled in a closed loop system; Penetration was carried out using a spherical indenter supplied with the

equipment. Preliminary tests were carried out at different maximum loads, and at differing loading and unloading rates. A holding time of 10 minutes and 20 minutes were compared. Thereafter, the optimum and most practical testing conditions were selected.

The selected testing cycle was as follows:

- Heat at 10^{o}C/min to set temperature.
- Equilibrate by holding at temperature for 1 hour.
- Apply load at 18N/min (0.3N/s) to maximum load.
- Hold at maximum load for 10 minutes.
- Unload at 18N/min (0.3N/s).

A maximum load of 0.7N was used for temperatures up to 105^{o}C, and above that temperature, a maximum load of 0.2N was used. The reason for the decreased load at high temperatures was to limit the penetration depth as the material became more compliant close to the T_g. Note that at the selected loading rate, the indenter would take just over 2 seconds to reach the maximum load of 0.7N and less than 1 second to reach 0.2N.

Optical imaging was carried out on the indenter to determine its diameter. The Oliver & Pharr method for spherical indenters, equation (2.16) was used to calculate E*.

Three-point bend tests over the temperature range of 40^{o}C to 115^{0}C were conducted for comparison with the results obtained from indentation methods in determining the glass transition temperature for reference polystyrene.

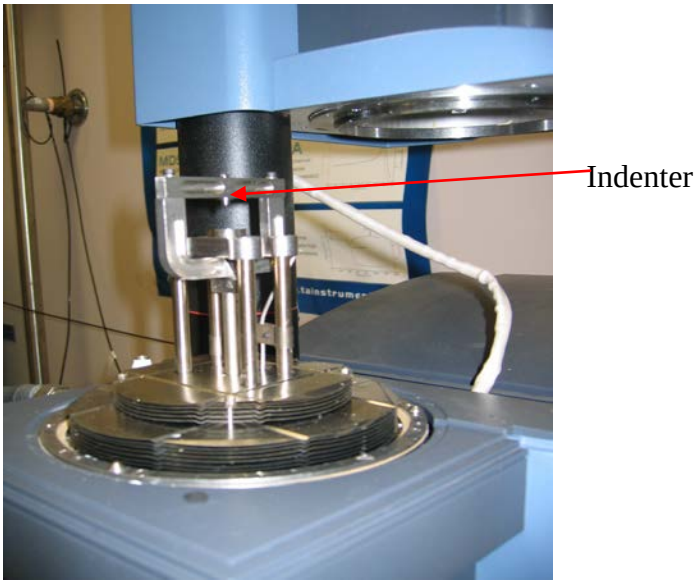

Figure 3.11: DMA (model Q800, TA Instruments) showing indenter assembly.

3.4.2 Mechanical models

Various models (using mechanical elements comprising of springs and dashpots) used to describe creep responses in micro/nano-indentations were examined. These models were used to fit the creep data obtained during indentation experiments using the UMIS apparatus or the DMA. Elastic modulus values were directly obtained from curve-fitting of the creep data. The results obtained were compared to those obtained using the Oliver & Pharr.

3.4.2.1 EVEV model

This section begins by describing the work of Yang et al. [84] in which a semi-empirical elastic-viscoelastic-viscous (EVEV) model was established to describe the creep behaviour of polymers indented using a flat-ended punch indenter. The authors claimed that the elastic modulus could be calculated using the empirical formula derived from their model. Thus the derived elastic modulus would be independent of the indenter unloading event, i.e., independent of holding time and unloading rate.

Using a generalised Kelvin model for a flat punch indenter, equation for indentation strain, ε, could be derived as shown in equation (2.64), section 2.6.1. Furthermore by introducing the concept of virtual length, h_{in}, such that $\varepsilon = h/h_{in}$, equation for the indentation displacement h can be obtained:

$$h = h_e + \sum_{1}^{n} h_i (1 - e^{-t/\tau_i}) + t/\mu_0 \qquad (2.67)$$

where h_e is the instantaneous displacement of the first spring element, and h_i represents the indentation depth at the *i*th Kelvin element.

For i = 0,

$$E_o = \frac{P_o h_{in}}{A_0 h_e} \qquad (2.68)$$

where h_{in} is defined as the virtual length equivalent to the displacement before creep begins, i.e., at the end of the loading cycle, at maximum load; and A_0 is the contact area at the end of the load cycle.

The authors extended the use of the model to Berkovich tips and noted two major differences between the two types of tips. Firstly, the Berkovich indenter caused significant plastic deformation during loading, which was not represented in the model. The plastic deformation h_p must therefore be subtracted from the total displacement for the model to be applicable. The penetration displacement due to plastic deformation was determined using the unloading data, using the Oliver and Pharr method. Secondly, the contact area would no longer be the constant, but instead would change with indentation depth for the Berkovich tip. The authors defined A_0 as the contact area before creep and in the experimental work outlined in this thesis; A_0 was calculated using the Oliver and Pharr area function, assuming an ideal Bervokich tip, as mentioned previously in section 2.4.3.1:

$$A(h_p) = 24.5h^2_p \qquad (2.14)$$

In the current experimental work, reference polystyrene as well as clear, black and white coatings, prepared in the Laboratory, were tested with the UMIS 2000 system, using a Berkovich diamond indenter. The coatings were cured at the optimum condition, and were approximately $20\,\mu m$ thick. The indentation test used in this study consisted of a loading segment, holding at maximum load, unloading to a load close to zero, followed by another hold at this load.

To ensure that the creep response is minimised in the loading and unloading segments, appropriate loading (and unloading) rates and holding times must be used. In general, the loading rate should be as fast as possible and the holding time as long as is practical. The effect of loading rate was studied by testing in the closed loop

configuration such that successive loading steps were only carried out once the system has reached the predetermined load step, i.e., a user specified loading rate was not possible. The loading rate in this mode would be comparatively slower, typically up to a minute to reach maximum load. In the open loop configuration, loading rates of 2.5mN/s and 5mN/s were used to reach a maximum load of 5mN. The drawback of a faster loading rate is that the desired maximum load would not always be attained during the holding cycle, and could be lower or higher than the actual load by as much as 10%. Also, a load-overshoot can occur before the actual holding cycle.

To minimise the substrate effect on the coated samples, attempts were made to use low loads so that the penetration depth was restricted to less than a tenth of the coating thickness [98, 99]. For the softer coatings (clear and black), the maximum load employed were much lower than that used for the white coating and for polystyrene. On the other hand, the same low load could not be employed for the harder samples as surface roughness effects would be exaggerated leading to inaccuracies [103]. The effect of maximum load was studied by testing polystyrene using maximum loads of 5mN and 10mN; and loads of 2.5mN and 1.5mN for the black coating. For the clear coating, a 1mN maximum load was employed.

The unloading rate was equal to the loading rate in each test, and unloading hold was carried out at 1% of maximum load for the same duration as for the holding time at maximum load. From previous unpublished work, the appropriate holding time for the coated samples was found to be 2400s, whereas a holding time of 1200s was sufficient for polystyrene. (Again the criteria used to establish the holding time was

for the creep rate to decay to a value where the creep displacement in 1 minute is less than 1% of the total displacement).

For each testing condition, between 6 and 10 indentations were carried out.

Experimental data were analysed using IGORPRO. Regression analysis was carried out on the unloading slope to determine the elastic penetration, in accordance with the Oliver and Pharr method. The plastic penetration can then be determined and subtracted from the creep penetration data. Further curve fitting of the creep data to the EVEV model was carried out using ORIGINPRO software.

A typical indentation test is shown in Figure 3.12. Points A-B describes the loading segment, B-C the creep event caused by constant load, C-D the unloading portion; and D-E the final unload hold. If loading and unloading rates are sufficiently fast, time dependent responses (creep) should be minimised in the loading (A-B) and unloading segment (D-E), such that loading would be mainly elastic and plastic (if indentation stress is sufficient to cause non-time dependent plasticity). Creep (which would include visco-elasticity and visco-plasticity) is restricted to segment B-C, corresponding to the hold period (10 minutes). Segment D-E shows recovery of visco-elastic displacement during a hold period (10 minutes) at constant load (set at 5% of maximum load). Since the segment of D-E is longer than segment B-C, it would imply that all the creep displacement has been recovered (including any creep displacement from the loading and/or unloading segment as well) and that there is negligible visco-plasticity present in the creep event. The discontinuity in the curve at the last load increment before creep at point ‘B’ is a consequence of using the open-loop configuration so that a user specified loading rate could be applied, since

the closed loop configuration is a lot slower as successive loading steps can only be carried out once the system has reached the predetermined load step. In the figure, the open loop configuration resulted in the system not attaining the maximum load at the end of the loading cycle. This load however, was attained at the beginning of the hold segment, at 'B'. Similarly at the end of unloading, at point 'D', the force at which unloading hold should begin was not reached, hence point 'D' is at a slightly higher load than point 'E'.

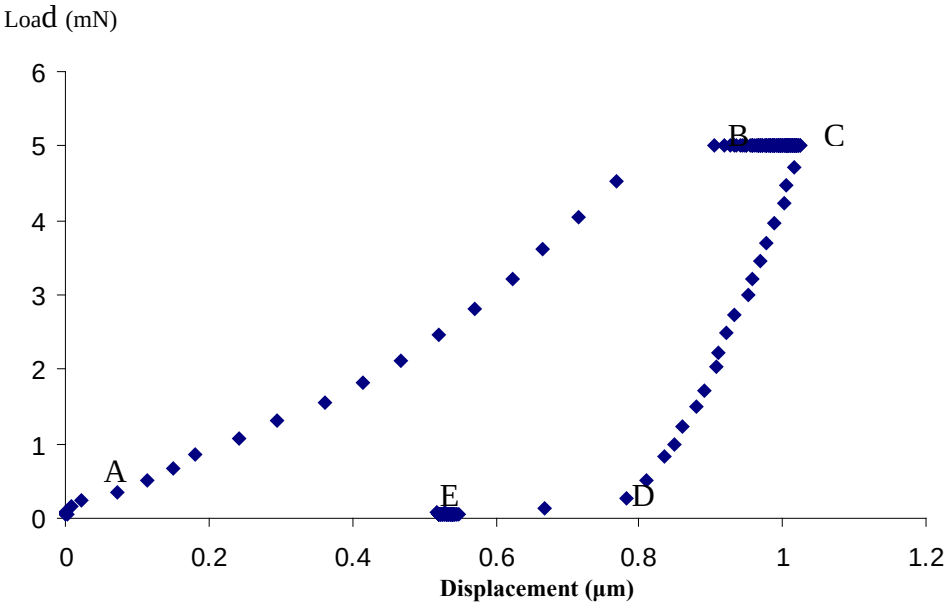

Figure 3.12: A typical indentation test carried out on polystyrene.

An approximate evaluation of h_e was carried out using Oliver and Pharr's power law equation [32, 84] on the unloading curve:

$$P = n(h-h_D)^m$$

where h_D is the indentation displacement at point D, corresponding to the end of the unloading segment; and is an approximation to the final indentation displacement.

By curve fitting the initial portion of the unloading curve, at maximum load, h_e can be calculated from the slope of the unloading curve and from equation (2.12). Again the geometry constant, ε is used and is equal to 0.75 for a Berkovich tip [32].

The plastic displacement, $h_{p,}$ can be calculated by subtracting the value of h_e from h_{in}.

Curve fitting of the creep data, using a Maxwell-Voigt model with different numbers of elements, was carried out, after subtracting h_p from the creep penetration data. An example is shown in Figure 3.13 below. A value of h_e was thus obtained, and the elastic modulus value was calculated.

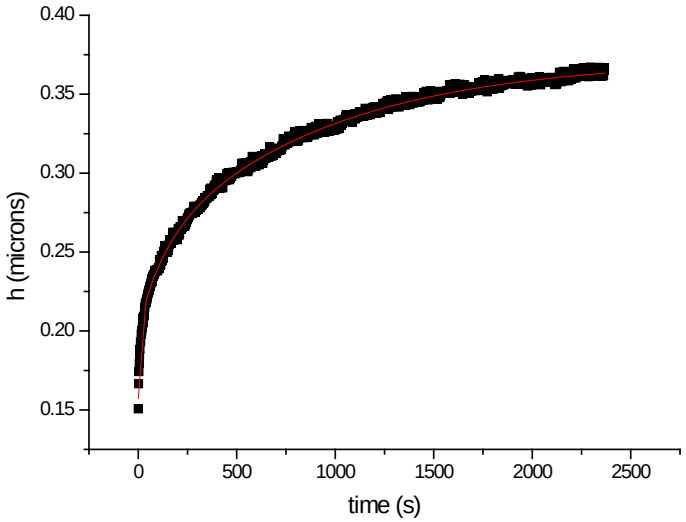

Figure 3.13: Typical plot obtained from creep experiement on polystyrene. Curve fitting using the EVEV model is shown as the superimposed red line.

3.4.2.2 Fischer-Cripps method

This method was employed to analyse some of the creep experiments carried out using the DMA, as described in section 3.4.1. High temperature tensile testing was also carried out using the DMA and the creep data thus obtained was analysed using the same method for comparison. Note that in his work, Fischer-Cripps [83] used the UMIS system and controlled ambient temperature. In the current work, the DMA was employed instead of the UMIS system as the DMA enabled testing at high temperatures. Keeping in mind that the creep model requires the initial applied load to be very rapid, in the current indentation work using the DMA, the longest time employed to attain maximum load was kept to just over 2 seconds.

The four element Maxwell-Voigt model, mentioned earlier in section 2.6.1, is illustrated in Figure 3.14. The equation describing this creep model is shown in equation (2.62) for a spherical indenter.

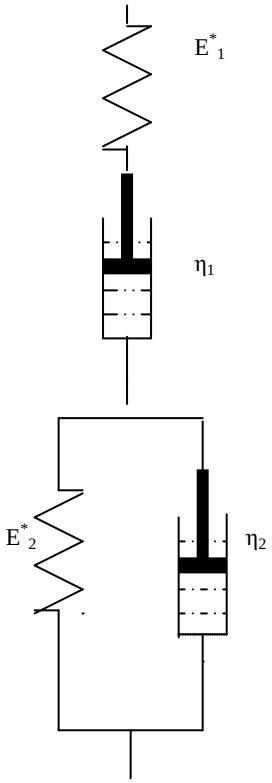

Figure 3.14: The four element Maxwell-Voigt model consisting of a Maxwell element in connected in series with a Voigt element.

There are usually three stages during a creep experiment. Unlike tensile creep test in which tertiary creep leads to fracture, fracture is unlikely to occur in indentation creep. For a viscoelastic material undergoing indentation creep, tertiary creep can take place as viscous flow, and can be represented by the dashpot, η_1 in the Maxwell element. Secondary creep is represented by the Voigt element (spring E^*_2 and dashpot η_2 connected in parallel) and primary creep is represented by the spring element E^*_1 in the Maxwell element. This instantaneous elastic response can be interpreted as the elastic modulus of the material. The elastic modulus E^*_1 is the combination of elastic modulus and Poisson's ratio of the specimen ($E^*_1 = E/(1-\nu^2)$)

and not the combined modulus of the indenter and the specimen as is normally expressed in the Oliver and Pharr equations.

$$h^{3/2}(t) = \frac{3}{4}\frac{P_0}{\sqrt{R}}\left[\frac{1}{E_1^*} + \frac{1}{E_2^*}\left(1 - e^{-tE_2^*/\eta_2}\right) + \frac{1}{\eta_1}t\right] \qquad (2.62)$$

Curve fitting was carried out using ORIGINPRO software. Non-linear least square fitting based on the Levenberg-Marquardt algorithm was employed. Initial values for the parameters E^*_i and η_i (i = 1, 2) were chosen for ten iterations. Normally, convergence occurred after four to five iterations and further iterations did not alter the values for the parameters significantly. The Chi square value shown after each iteration was used to estimate the error between the values fitted using the parameter values generated and the actual data points. At the end of the iteration process the coefficient of determination, R^2, was at 0.99, suggesting a good fit. The elastic modulus for the specimen could be extracted from the E_1^* value thus obtained and could then be compared to those obtained using the Oliver and Pharr method.

3.4.2.3 Oyen and Cook method

This method was used to analyse some of the creep data obtained from the UMIS system. Analyses were carried out using IGORPRO software.

In section 2.6.1 (equation 2.72) it was shown that for creep at constant applied load P_A,

$$h(t) = \frac{P_A^{1/2}}{\mu_Q^{1/2}} t + P_A^{1/2} \left[\frac{1}{(\alpha_2 E')^{1/2}} + \frac{1}{(\alpha_1 H)^{1/2}} \right] \qquad (2.72)$$

This gives a creep response that is linear with time. The y-intercept of the creep displacement vs. time curve would then yield the second term in the above equation. Since both α_1 and α_2 can be calculated for the Berkovich indenter (1.29 and 1.006, respectively), and hardness, H, can be obtained from the UMIS indentation test (directly from software output), the modulus value could, in theory, be calculated. An attempt was made to calculate the modulus value for reference polystyrene, as well as for a production white coating sample.

Preliminary results revealed that the method was highly subjective to the range of data selected for linear curve fitting, resulting in large variations in the modulus values obtained. Hence this method was not pursued further.

3.4.3 Analytical method to correct for viscoelasticity

3.4.3.1 Feng and Ngan method

In section 2.6.2, it was shown that the elastic recovery stiffness, S, could be corrected from the unloading contact stiffness, S_u, if the unloading rate and the creep rate at the end of the holding period was known.

$$\frac{1}{S} = \frac{1}{S_u} + \frac{\left|\dot{h}\right|_{hold}}{\left|\dot{P}\right|} \qquad (2.76)$$

Some of the creep data generated from the UMIS work (section 3.2.3) and those generated from the DMA work (section 3.4.1) were analysed using this method and the results were compared to those obtained using the EVEV model, the Fisher-Cripps model, and the Oliver and Pharr method. Analyses to yield the elastic stiffness, S, by means of the Oliver and Pharr method, were carried out using IGORPRO software. In general, only the initial portion of the unloading data was used for the analysis (approximately the first 20% of the unloading data).

3.4.3.2 Boltzmann superposition principle

Before the superposition principle can be used, linear viscoelasticity must first be established. Linear viscoelasticity can be shown by examining the results from curve fitting using various mechanical creep models, at different maximum loads or holding times. For polystyrene, this can be illustrated using the DMA, by indentation at different maximum loads (0.5N and 0.7N) at the same loading and unloading rates (3N/min) at 40^0C, and secondly using different holding times (4 and 6 minutes) at identical loading conditions (@18N/min to 0.7N) at 80^0C (Figure 3.15 & Figure 3.16). Then, using the 4-element Fischer-Cripps mechanical model, the creep curves were analysed and yielded similar values for the parameters in the two cases. That is, different maximum loads (at 40^oC) gave similar values for the parameters E^* and η, and the same was true for different holding times (at 80^oC). The results for the maximum load of 0.7N, with a 4 minute hold, however, were not similar since the

test temperatures were different in the two cases. Temperature would affect creep as well as general mechanical properties. The results are shown in Table 3.1 below.

Table 3.1: Values generated from curve fitting using the Fischer-Cripps model, for creep data resulting from different maximum load and different holding times, on polystyrene.

Load (N)	Holding time (minutes)	Loading rate (N/min)	Temperature (^{o}C)	E_1^* (GPa)	E_2^* (GPa)	η_1 (GPa s)	η_2 (GPa s)
0.5	4	3	40	1.5	49.2	$5.7x10^4$	$2.8x10^3$
0.7	4	3	40	1.9	52.1	$8.1x10^4$	$4.2x10^3$
0.7	4	18	80	1.4	17.4	$4.5x10^3$	54.1
0.7	6	18	80	1.6	15.0	$4.5x10^3$	64.2

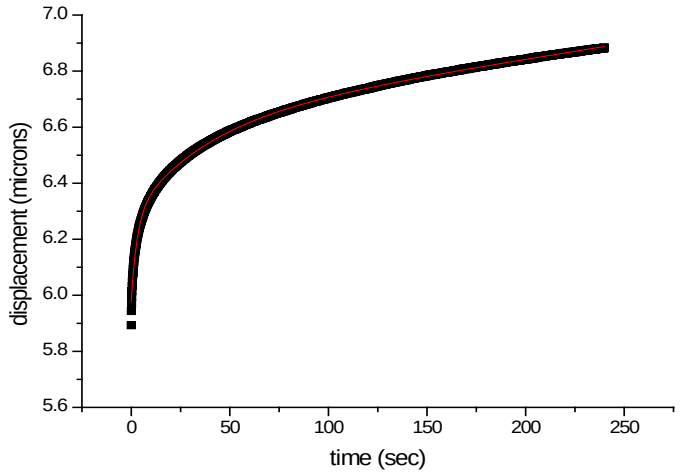

Figure 3.15: Curve-fitting carried out using the 4-element Fischer-Cripps mechanical model, on polystyrene. Holding time – 4 minutes.

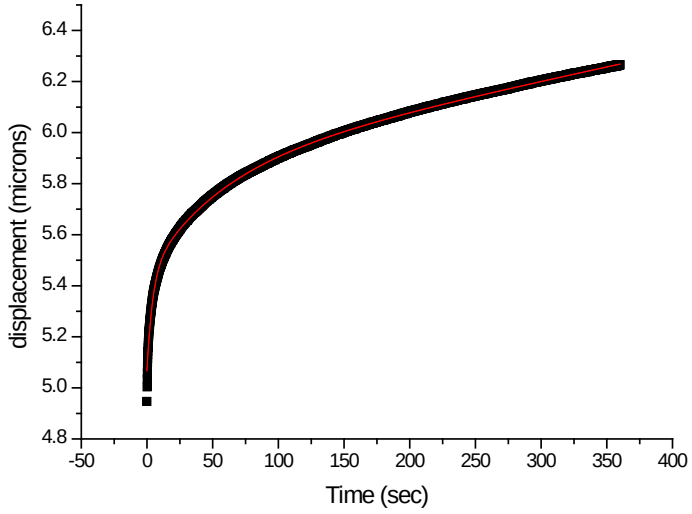

Figure 3.16: Curve-fitting carried out using the 4-element Fischer-Cripps mechanical model, on polystyrene. Holding – 6 minutes.

A similar exercise was performed on a clear colorbond paint coating using the UMIS, and a spherical probe for indentation. A loading rate of 2.5mN/s to a max load of 1mN was employed. Holding times were varied at 1, 4 and 10 minutes. The results are shown in Table 3.2. Again the values for the individual parameters E^* and η were similar for all three holding times, indicating that the assumption of linear viscoelasticity for the material holds true. Figure 3.17 shows the fitted curve (red) superimposed onto the original data for the clear paint coating at 1 minute holding time.

Table 3.2: Values generated from curve fitting using the Fischer-Cripps model, for creep data resulting**:** from different holding times on a clear paint coating.

Time (minutes)	E_1^* (GPa)	E_2^* (GPa)	η_1 (GPa s)	η_2 (GPa s)
1	0.48	0.96	17.6	11.71
4	0.42	0.62	21.6	17.54
10	0.41	0.23	29.7	19.12

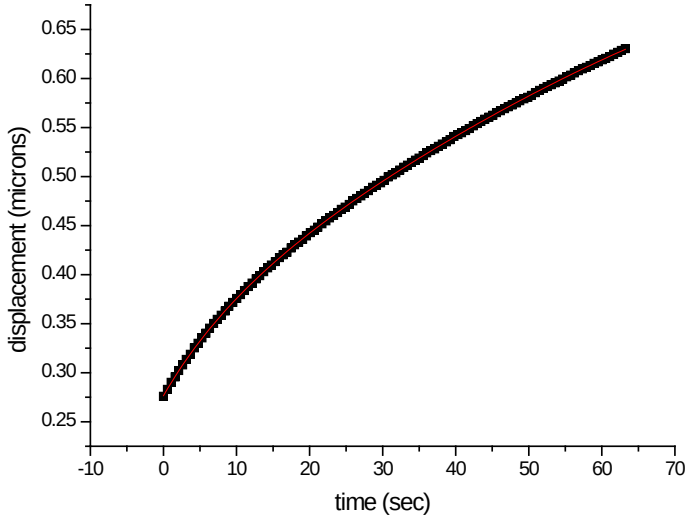

Figure 3.17: Curve fitting carried out using the 4-element Fischer-Cripps mechanical model, on clear colorbond, for the 1 minute holding time.

Once the materials were determined to be linear viscoelastic, the Boltzman Superposition Principle could be applied. Indentations were made at conditions that would allow significant creep to occur. For the DMA experiments, indentation creep data generated on reference polystyrene carried out at 110^{o}C were used. For the UMIS experiments, indentation creep data generated on the clear colorbond sample, with its T_g close to ambient, was used. Using applicable mechanical models, such as the Fischer-Cripps 4 element model for the DMA data, and the EVEV model for the UMIS data, the creep data could be modelled as a function of time, and extrapolation could be carried out for the duration of the unloading event. A schematic diagram showing a creep curve with an extrapolated portion is illustrated in Figure 3.18. The justification for the extrapolation procedure stems from the viscoelastic nature of polymer in the vicinity of the glass transition. The viscoelasticity results in a negative

unloading slope as the indenter continues to penetrate deeper into the specimen even as the load is decreased. This delayed response is also observed in the hold segment before fully unloading, and a substantial elastic recovery is observed as the specimen 'pushes' the indenter towards the original specimen surface, tens of minutes after the indenting force is removed. The negative unloading slope implies that the specimen is still 'creeping' under the effect of indenter load, and that the creep rate is higher than the unloading rate. Bearing in mind that the unloading event typically takes around 2 seconds, it is not unreasonable to assume that at the beginning of unloading, the specimen would experience delayed response to the full load. Indeed, the maximum displacement (or 'nose') is often observed in the unloading curve. As unloading progresses further, the specimen may response to a decrease in load (the extent of creep might still be higher than expected for the actual load, since a delayed response is expected), and the parameters for the fitted equation would be different because of a different load and hence different stress and strain condition. However, since it is the initial portion of the unloading that is of interest when the O&P method is applied (in our current work, approximately 20% of the initial unloading data would be used), for the sake of simplicity, the creep equation obtained for the constant load used during the creep test is used to extrapolate creep displacements for the entire unloading duration. The creep displacement during unloading can then be subtracted off the displacement attained at the end of the creep test. This difference in displacement is denoted $\Delta d(t)$ in Figure 3.18. In this way a 'revised' unloading curve could be obtained, as illustrated in Figure 3.19. The initial portion of this curve should approximate creep-free displacement with load. Assuming that plastic deformation occurred instantaneously at initial loading, the revised curve (with reduced stiffness S_r) would then be due to elastic recovery alone and the O&P

method would be applicable for the estimation of elastic modulus for the specimen. It should be noted that the accuracy for this ‘creep-free’ approximation would decrease as unloading progresses further, since with lower loads and reduced strain, a new creep equation with different parameters would apply.

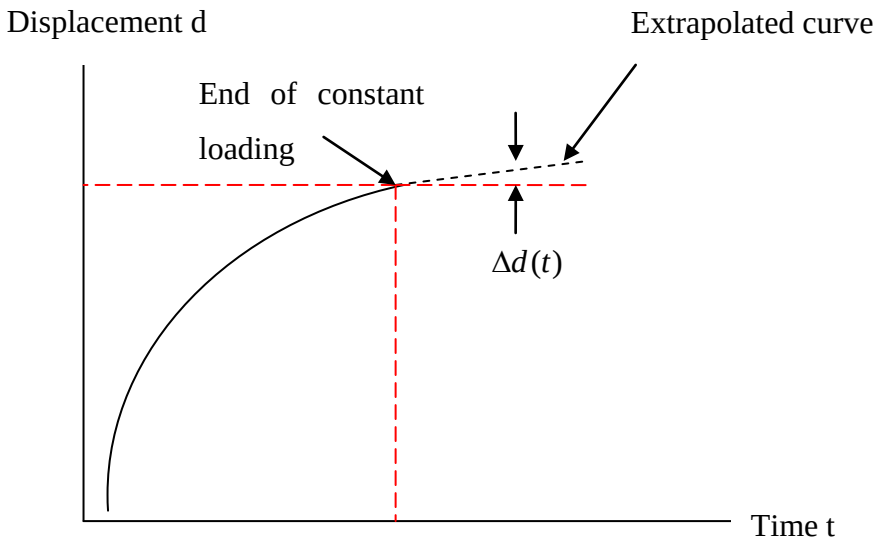

Figure 3.18: schematic diagram illustrating the method used for creep curve extrapolation.

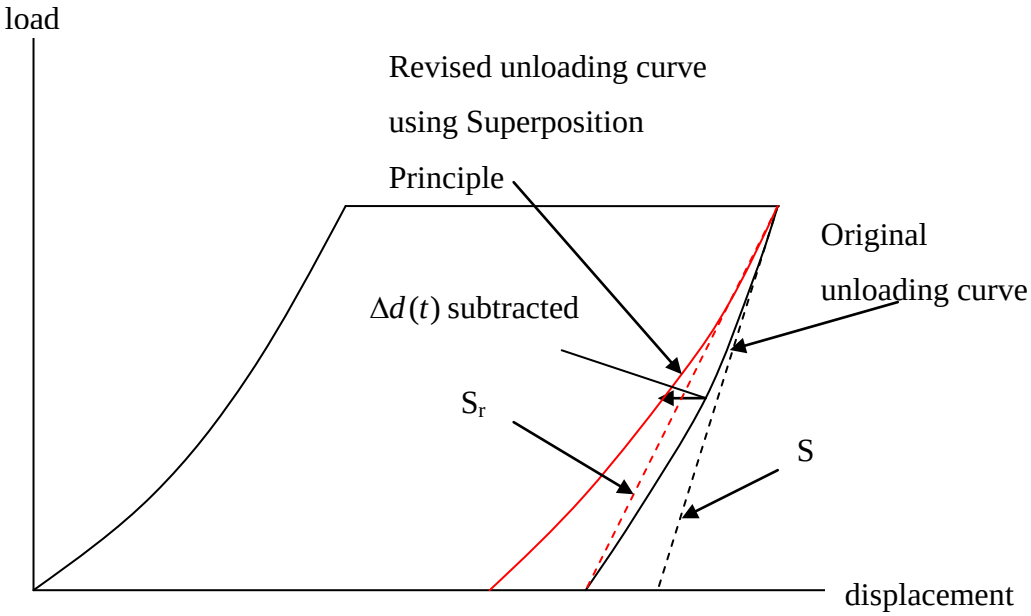

Figure 3.19: Schematic diagram showing the application of the Superposition Principle for the correction of the unloading data.

4 RESULTS

4. 1 Ultramicro-indentation

4.1.1 Repeatability and surface roughness effects

The ability of the micro-indentation technique in producing repeatable results is considered in this section. The effect of surface roughness is also examined, as the paint coatings being tested are inherently rough, and cannot be polished without causing damage or changes to their properties. For this work, polystyrene having varying degrees of surface roughness was used as a model system and the E* values obtained were compared.

The results of the repeatability tests conducted using the Berkovich indenter on polished polystyrene are shown in Figure 4.1. The force-displacements curves for the five indentations taken at different locations virtually overlap one another, yielding a reduced modulus E* of 4.3GPa. Knowing the modulus of diamond and Poisson's ratio for diamond and for polystyrene, the modulus of the reference polystyrene was found using equation (2.4) to be 3.8GPa. No significant standard deviation was recorded, demonstrating that indentation of a flat, glassy polymer gives very reproducible results.

The results of the surface roughness test using the Berkovich indenter on roughened polystyrene (roughness induced using grade P400 SiC grinding paper) are shown in

Figure 4.2 and tabulated in Table 4.1. It can be seen that the force-displacement curves for the five indentations varied greatly. The results showed that although the E* values obtained in each of the 5 indentations also varied greatly, the unloading slopes did not differ to the same extent. From equation (2.10) and equation (2.14), it can be deduced that the large differences in E* values were the result of large differences in h_p. Since the total displacement is the sum of the elastic displacement (h_e) and the plastic displacement (h_p), and since the unloading slope and hence the elastic recovery (equivalent to h_e) of the indentations did not differ greatly, it can be concluded that the variations in E* was caused by asperity loading affecting the total displacement recorded.

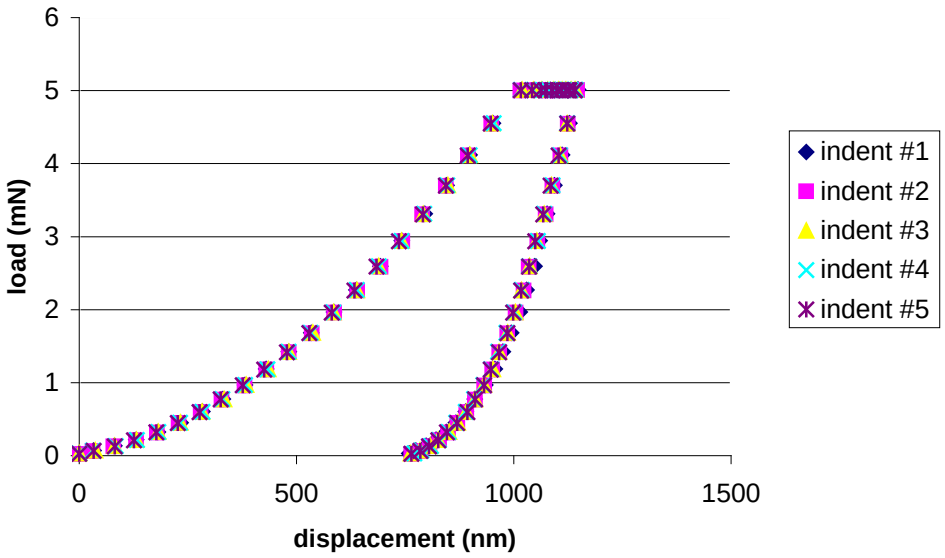

Figure 4.1: Indentation on polished polystyrene using the UMIS system with a Berkovich indenter.

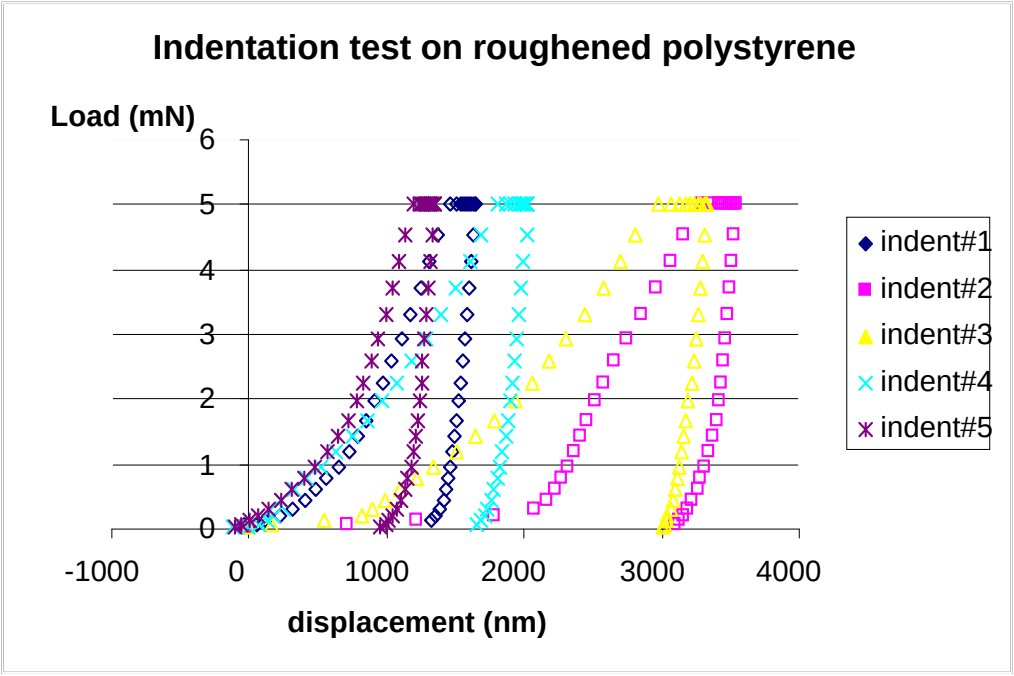

Figure 4.2: Indentation on roughened polystyrene using the UMIS system with a Berkovich indenter.

Table 4.1: Surface roughness test results on roughened polystyrene.

Indentation #	E* (GPa)	Unloading slope (mN/μm)
1	3.46	32.51
2	1.48	30.19
3	1.57	33.85
4	2.46	35.39
5	4.56	28.08

Further evaluation of the effect of surface roughness on indentation results was conducted using a spherical indenter. Table 4.2 summarises the modulus values obtained at the maximum load for samples indented with two different size indenters and to different maximum loads. The standard deviation in E* obtained from 3 to 5 repeat tests under each condition is also included in Table 4.2. The reference sample

polished to a 1μm finish was indented to 300mN with the larger size (500μm radius[1]) WC spherical indenter. The composite modulus, E*, was found to be very reproducible, viz., 4.3GPa, giving an elastic modulus, E, of 4GPa, from equation (2.4). It should be noted that the modulus value obtained at maximum load is similar to that obtained using the Berkovich indenter, but somewhat higher than reported elsewhere [104]. However, the method from which the literature value was obtained was not stated in the reference, and the discrepancy may be due to variations in loading rate or test temperature.

[1] Area correction carried out using a look-up table that was supplied and incorporated into the analytical procedure in the equipment software.

Table 4.2: Modulus and surface roughness results using WC spherical probes,

UMIS tests						
surface finish	indenter radius	Maximum Load	E* (GPa)	Estimated contact D'(μm)	"Roughness" range(nm)	Average "Roughness"
1μm	500μm	300mN	4.30 ± 0.02	23 - 27	130 - 180	180nm
3μm	250μm	100mN	3.76 ± 0.04	17 - 25	150 - 300	370nm
	500μm	300mN	4.20 ± 0.02	29 - 34	210 - 290	240nm
	500μm	300mN	4.49 ± 0.13	20 - 43	100 - 470	370nm
	250μm	500mN	4.38 ± 0.07	21 - 30	230 - 450	230nm
	250μm	500mN	3.82 ± 0.01	21	219 - 220	220nm
	500μm	500mN	4.10 ± 0.00	24 - 41	140 - 430	400nm
6μm	500μm	100mN	2.66 ± 0.9	Could not be determined	Could not be determined	Could not be determined
	250μm	300mN	3.69 ± 0.03	31 - 36	470 - 650	540nm
	250μm	500mN	3.74 ± 0.01	33 - 37	550 - 690	500nm
	250μm	500mN	2.71 ± 0.31	21 - 34	220 - 590	400nm
	500μm	500mN	4.16 ± 0.02	37 - 61	350 - 920	530nm

AFM - Rmax value				
surface finish	10μm scan	30μm scan	50μm scan	100μm scan
1μm	100 - 140nm	240 - 360nm	260 - 840nm	340nm - 1.1μm
3μm	150 - 300nm	240 - 460nm	460nm - 1.1μm	940nm - 1.6μm
6μm	370 - 720nm	790 - 930nm	790nm - 1.6μm	1.2 - 2.0μm

surface finish	AFM – median depth for 30μm scan
1μm	170 - 200nm
3μm	150 - 320nm
6μm	470 - 620nm

Unusually low modulus values and large scatter in the modulus values were obtained on the roughest samples when low loads were used (Figure 4.3). For the 6μm polished samples, when an indenter with a radius of 500μm was used, the composite

modulus increased significantly when the maximum load increased from 100mN to 500mN (Figure 4.3a). However, the composite modulus values obtained using a maximum load of 300mN and 500mN were similar for the smaller indenter size (radius of 250μm). The effect of loading force on the modulus was less obvious for the 3μm polished sample (Figure 4.3b), and only a slight increase in modulus was observed when the maximum load was increased from 100mN to 500mN (indenter radius of 250μm), and a slight decrease in E* values with increasing maximum load using a larger indenter. These slight variations in the E* results could be attributed to expected variations in the bulk E* value, which was found to be between 3.7GPa and 4.3GPa. Furthermore, it is important to note that, in general, increasing the load increased the accuracy of the tests, as indicated by the smaller standard deviations observed at the higher loads (Table 4.2).

Figure 4.4 illustrates the apparent changes in modulus measured at different penetration depths for the 6μm sample. The results suggest that the sample has an unusually low surface modulus (~ 0.3GPa) to a depth of 2μm. Between 2-3μm the modulus increases but the maximum value (1.9GPa) is still only half that expected for polystyrene. These unusual results are due to the indenter making contact with high surface asperities. The contact area is much smaller than assumed (for flat surfaces) and the contact stress is much higher, causing large deformation. Since the analysis of the penetration assumes a perfectly flat surface, the assumed low contact stress and high penetration lead to an inaccurately low modulus value. The increase in apparent modulus at deeper penetration is due to the flattening of high asperities and the formation of a larger contact area.

The results shown in Figure 4.4 were not common and more typical results were of the type shown in Figure 4.5. Here the apparent surface modulus is closer to the bulk value. The modulus increases with higher loads (deeper penetration) until a constant value was reached that does not change with further penetration. The maximum value occurs when all asperities have been flattened and full contact between the indenter and the surface has been made (as would occur on perfectly flat samples at all loads). Note that a deeper penetration (920nm) was required to reach a constant modulus for the 6μm sample compared to the less rough 3μm sample (≈500nm).

The effect of asperity contact at low loads on rough surfaces is illustrated schematically in Figure 4.6. A certain load (P_2) is required to make full contact between the indenter and a rough surface, whereas full contact occurs at smaller loads (P_1) on a smooth surface. Since the local stress is much higher at the contact points on a rough surface, a much greater penetration occurs at low loads (δ_1 to δ_2) on a rough surface than on a smooth surface. Once flattening all asperities has made full contact, however, further loading (P_2 to P_3) produces the same deformation (δ_2 to δ_3) on both smooth and rough surfaces. In this situation the measured elastic modulus is the same for both smooth and rough samples. However, a lower apparent modulus will be obtained on rough samples at low loads before full contact is made.

If the flattening of asperities is the reason for the low modulus values obtained at low loads, then a correlation is expected between the surface roughness and the penetration distance needed to fully flatten the asperities. The latter can be determined from the modulus/penetration curves, as illustrated in Figure 4.5 by

distance h*. These roughness values are included in Table 4.2: 130-180nm for the 1μm finish; 150-430nm for the 3μm finish; and 350-920nm for the 6μm finish.

The surface roughness was also measured using the AFM in Tapping Mode (Table 4.2). In this case the R_{max} value is reported, which is the distance between the highest point and the lowest point recorded in the scan area. All scanned images were 'flattened' using a plane-fit procedure to remove the large-scale waviness from the roughness analysis. As can be seen from Table 4.2, the R_{max} value is consistently higher when larger scan sizes were used. This is because there is greater probability in encountering larger asperities when a larger area of the surface is scanned.

For the purpose of comparing the penetration roughness (h*) with the AFM roughness (R_{max} and median depth), an AFM scan size similar to the indenter/surface contact diameter (D') was chosen. From simple geometry and assuming only elastic response of the material, the contact diameter could be estimated from equation (3.1). This contact diameter corresponds to the point where all asperities are flattened and the first full contact between the indenter and rough surface has been made. As summarised in Table 4.2, the contact diameters are mostly around 30μm. Thus, the R_{max} values measured from the smaller scan sizes (10μm or 30μm) are better for comparing with the indentation roughness parameter (h*). The correlations between h* and R_{max}; and h* and median depth are reasonable, with a distinct increase in measured roughness by both techniques in the order 1μm finish, 3μm finish, 6μm finish, as would be expected.

(a)

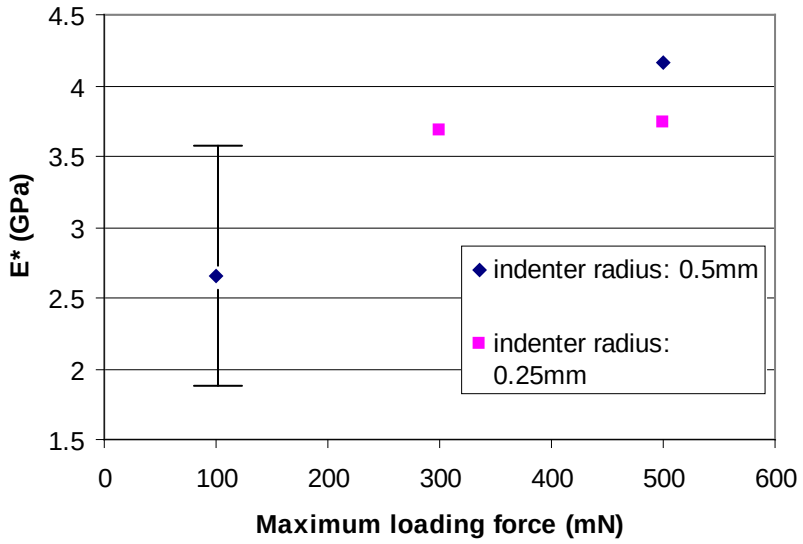

(b)

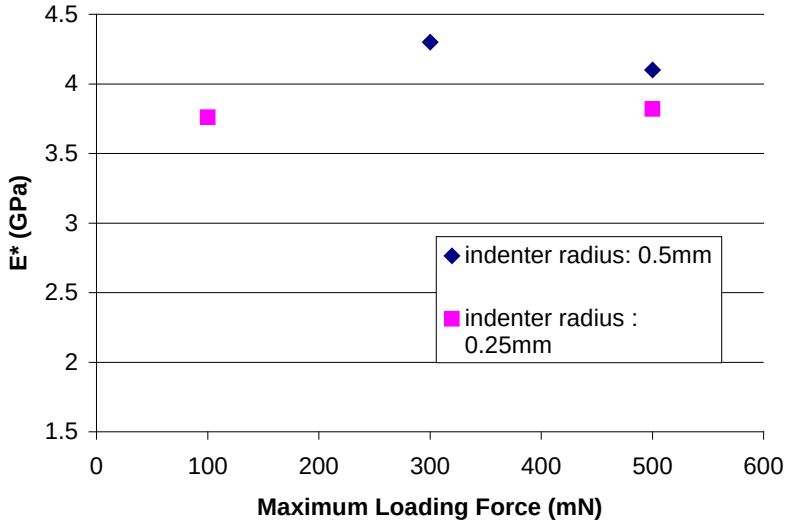

Figure 4.3: Effect of loading force on measured modulus: (a) 6µm finish; (b) 3µm finish. Note that error bars for the other data points are too small to be shown

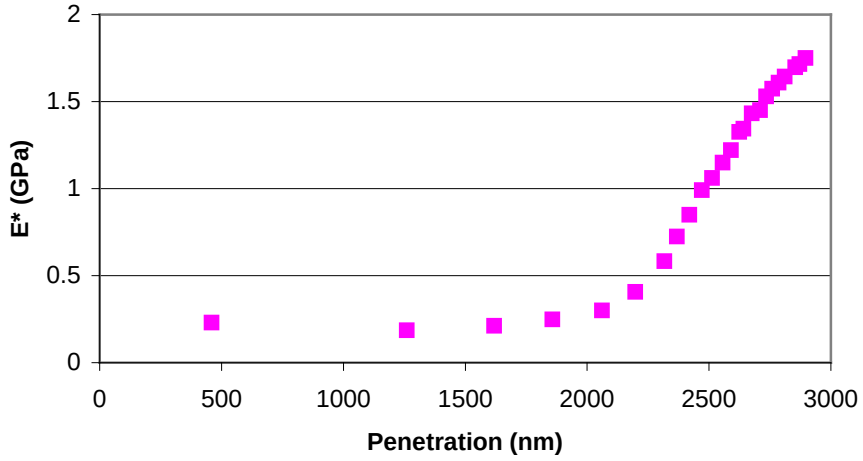

Figure 4.4: Measured modulus as a function of indentation depth for a polystyrene sample roughened to a 6µm sample and tested to 100mN. Indenter radius - 500µm.

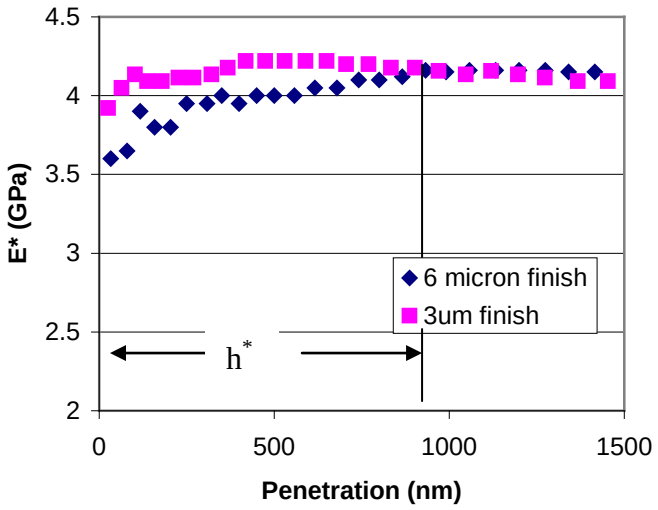

Figure 4.5: Variations in E^* with indentation depth for two samples tested to 500mN. Indenter radius - 500µm.

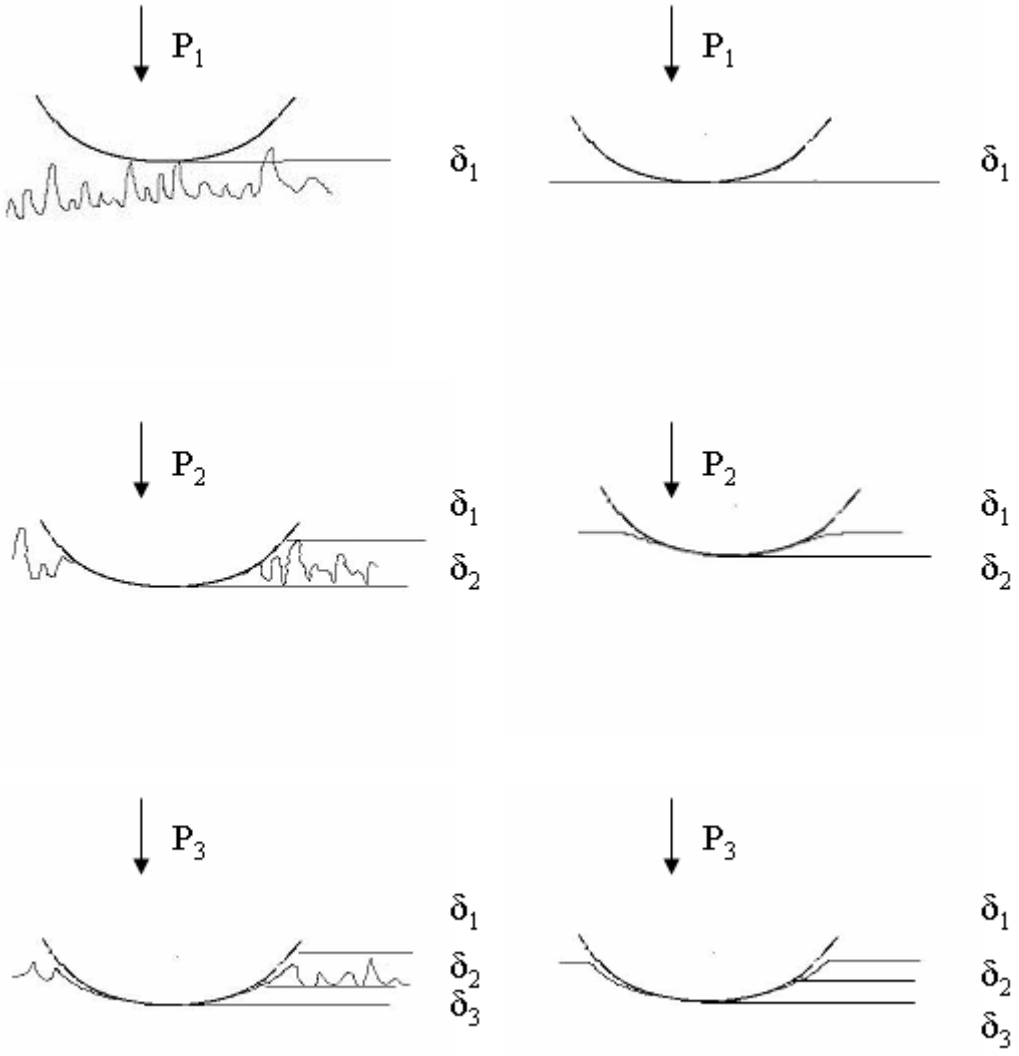

(a) (b)

Figure 4.6: Schematic showing indenter penetration into a (a) rough surface and (b) smooth surface.

4.1.2 Micro-indentation of paint coatings

The usefulness of micro-indentation for measuring the mechanical properties of polymers, and especially paint coatings is considered in this section. Coated samples were tested in the as-received condition using a Berkovich indenter. The paints are pigmented and, therefore, rough. The purpose of this study was to establish how useful standard indentation tests are for the typical paint coatings. Coatings have been prepared at different peak metal temperatures (PMTs), since the PMT is known to affect the performance of the coating in service (e.g., scratch resistance). (PMT is the temperature which the metal substrate attains in the paint coating curing process.) Secondly, different coloured paints have been studied since the different colours have different volume fractions of inorganic particles that act as pigment. The coating modulus should be sensitive to the volume fraction of pigment used.

The results for the first batch of white paint cured at different PMT are shown in Figure 4.7 and tabulated in Table 4.3. Ten indentations were conducted on each paint and the standard deviation was ~10% of the average modulus value. This variability reflects the inherent roughness of these paints. Despite this uncertainty, the results showed a clear correlation between modulus values and PMT. The modulus values obtained for the PMT of 230^{o}C were the highest, and those obtained at the PMT of 185^{o}C were the lowest. This trend was expected since the PMT of 230^{o}C was recommended by the paint supplier and considered to yield optimum amount of crosslinking in the paint matrix, thus yielding optimum mechanical properties. Overcuring by 27^{o}C to a PMT of 257^{o}C resulted in a significant drop in E* values.

This phenomenon has been reported previously [105] for similar industrial coil coating systems. Overcuring tends to cause oxidation of the polyester resin, leading to degradation and embrittlement, causing a drop in stiffness and the observed dropped in modulus values Deviating from the optimum PMT further by ~45^{o}C caused undercuring at the PMT of 185^{o}C. The E* values obtained at this PMT were the lowest, possibly since this temperature was the furthest from the ideal PMT. Undercured systems tend to result in insufficient crosslinking, leading to soft, weak films with poor durability, and low stiffness, as reflected in the modulus values.

It should be noted that the overall modulus values obtained were lower than would be expected. The E* values obtained at optimum PMT averaged at 1.8GPa, as compared to a much higher value for a second batch of white paint coating made in the laboratory at the same PMT, which gave a E* average of 4.6GPa (refer to Table 4.4). The low modulus results could be attributed to the thicker than usual paint layer used in the first batch (24μm as opposed to 18μm) which might have caused trapped solvent within the layer. Also a thicker layer would be more prone to thermal variations from the metal substrate to the surface. Such non-uniform conditions through the thickness of the coating could lead to non uniform curing and poor mechanical properties compared to a thinner coating.

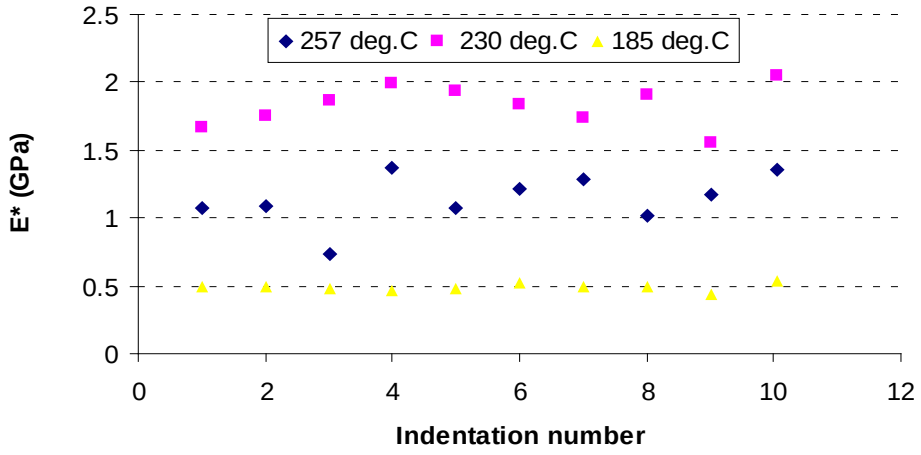

Figure 4.7: E* values obtained for ten indentations for white paint coatings cured at different peak metal temperatures (PMTs).

Table 4.3: Modulus values of the first batch of white paint coatings at different PMTs

PMT	185^{o}C	230^{o}C	257^{o}C
E* (GPa)	0.5 ± 0	1.8 ± 0.1	1.1 ± 0.1

The results for the second batch of white coating, having the normal thickness of 18µm, and cured at different PMTs are tabulated in Table 4.4. A much narrower range of PMTs were used in this study since PMT variations in practice are much smaller than those used to prepare the first batch of samples. The modulus values obtained for the samples cured at PMTs of 230^{o}C and 248^{o}C were similar; while a slight decrease in E* was observed with a higher PMT of 255^{o}C. This trend is similar to those observed for the thicker coatings (first batch). Now, however, the inherent error of ~10% in the test procedure is similar to the difference in average value obtained for the different paints. Small variations in modulus cannot be determined using this method. The optimum PMT appears to extend from 230^{o}C to at least 248^{o}C, with the corresponding modulus value of 4.6GPa.

Table 4.4: Modulus values of second batch of white paint coating at different PMTs

PMT	230^{o}C	248^{o}C	255^{o}C
E* (GPa)	4.6 ± 0.4	4.6 ± 0.4	4.1 ± 0.3

Different coloured paints were examined next to determine the sensitivity of micro-indentation to changes in pigment types. Different pigment types and contents produce the different observed colours in the coatings, with the clear coating having no pigment or filler additives; and the white paint having the most filler. The results of samples obtained from production samples as well as the laboratory-prepared samples are shown in Table 4.5. The E* values for different colours showed significant differences, with the white paint having the most pigment/ filler content recording the highest E*, and the clear paint with no pigment additives having the lowest value. The industrial white paint examined contained 50.7wt% TiO_2 pigment, while at the other extreme; the black paint contained only 23.1 wt% copper chromites pigment. The brown paint contained 41.2 wt% of mixed metallic oxides. If the density of TiO_2, Cu Chromites and polyester were taken to be 4200kg/m^3, 5200kg/m^3 and 1200kg/m^3, respectively; and the density of the mixed metallic oxides were approximated to be around 4700kg/m^3, then the volume fractions of the pigments could be estimated. Thus, the volume of pigments was estimated to be 22.6%, 15.2% and 6.5% for the white, brown and the black paint, respectively. Theoretically one could use the rule of mixtures to estimate the composite modulus E_c from the modulus and the volume fractions of the particulates and the matrix, such that:

$$E_c = V_p E_p + V_m E_m$$

For the white paint, the contribution from the pigment alone, which has an elastic modulus of 230GPa, would give a modulus of 52GPa! Clearly, other factors such as the shape of the pigment, the degree of bonding to the matrix and their distribution at the surface would play a role at determining the composite modulus, rather than the volume fraction alone.

The laboratory samples produced lower E* values than those obtained for the same colour coating from production samples. Comparing the white coatings tested, the laboratory samples yielded E* values of 4.0GPa (Table 4.5) to 4.6GPa (Table 4.4) while the production samples yielded average values of 6.5 and 6.7GPa (Table 4.5). The higher modulus from the production samples could be a reflection of the more stringent process control in production. The paint is subjected to vigorous stirring and viscosity checks before application, to prevent particles from clustering and to ensure the correct solvent content. In the laboratory the paint was stirred prior to application, but no further checks were used to ensure uniform pigment distribution or to ensure correct solvent content. If clustering of the pigments particles occurred, then the ratio of surface area of the pigments to that of the polyester matrix would decrease, effectively dropping the modulus of the composite paint. Insufficient solvent could also affect the flow of the paint, again affecting the particle distribution. In extreme cases, it may even lead to trapped air bubbles. On the other hand, excessive solvent could lead to trapped solvent in the paint, thus adversely affecting the properties of the coating. In addition, the differences in E* values could

indicate differences in the curing conditions in the production curing process as opposed to the simulation process used in the laboratory.

Table 4.5: Modulus values of different colour coated samples.

Production	E* (GPa)	Laboratory	E* (GPa)
Brown	5.9 ± 0.9; 5.7 ± 0.7	Clear	2.2 ± 0.5
White	6.7 ± 0.3; 6.5 ± 0.5	White	4.0 ± 0.3

It is expected that the surface roughness has a significant influence in the testing of paint coatings as the filled coatings are inherently rough. These coatings are too thin to be polished and polishing would likely result in the pulling out of pigment/filler particulates. Because of the unavoidable roughness, some scatter in the results for the coated samples would be expected, contributing to the large standard deviations compared to the actual modulus values. For the clear coating, the large scatter was attributed to the entrapped bubbles in the film, caused by solvents evaporating during the curing process. Some bubbles might be present in the coloured coatings too, although they were not easily observed as in the case of the clear coating.

The surface roughness of the paint coatings are shown in the AFM height images in Figs 4.8-4.10 and tabulated in Table 4.6.

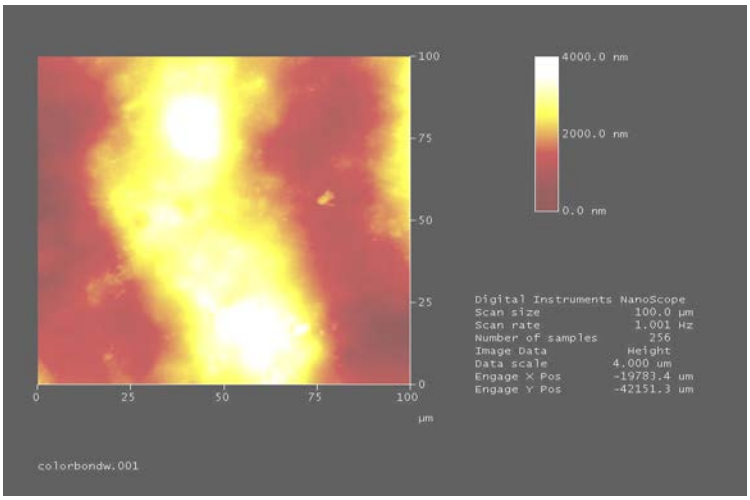

Figure 4.8: Contact mode AFM image of a white paint coating.

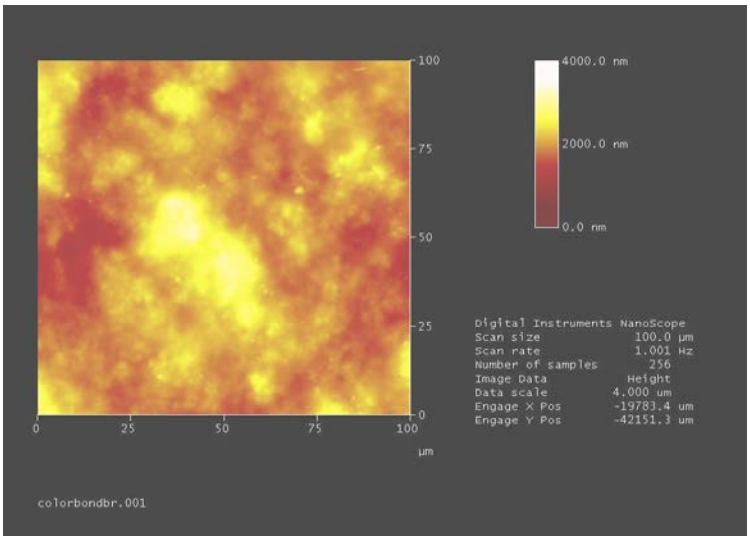

Figure 4.9: Contact mode AFM image of a brown paint coating.

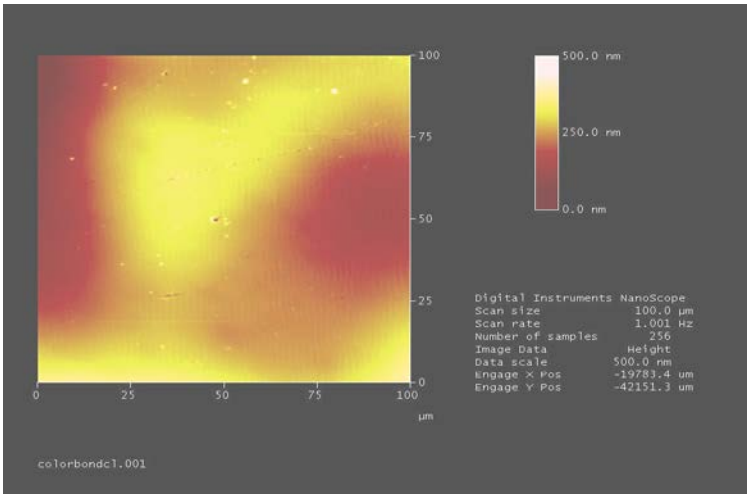

Figure 4.10: Contact mode AFM image of a clear paint coating**.**

Table 4.6: Surface roughness of the colour paint coatings.

Coating	Rmax(nm)	Ra(nm)	Rms Rq(nm)
white	4206	705.11	826.46
Brown	2117	235.44	303.46

Despite large standard deviations in the measured modulus, the technique appeared sufficiently sensitive in differentiating between samples of different curing conditions, as well as different pigment/filler contents. Differences in curing conditions were reflected in the first batch of samples prepared at different PMTs and only slightly for the second batch which had a narrower range of PMTs. For the latter, both PMTs of 230^{o}C and 248^{o}C appeared to yield optimum results, suggesting that quite a broad range of PMT exists for optimum curing. The first batch of samples cured at different PMTs had very low E*, and were likely to be undercured due to the thicker paint coatings been applied. Differences in curing conditions were also reflected in the modulus results between the production white coating and the one cured under laboratory conditions (Table 4.5). Furthermore, the results in Table 4.5 illustrated the effect of pigment contents on modulus values with decreasing

modulus values being recorded for coatings having decreasing amounts of pigments, as expected. The large variation in measured modulus values is attributed, at least in part, to the unavoidable roughness of the samples which induces asperity contact problems as discussed in Section 4.1.1.

Indenter geometry and analytical methods

The most widely used probes are the spherical and the Berkovich indenters, using the Oliver & Pharr method to analyse the unloading data. With the spherical indenter, the Field & Swain method has become popular since the method allows for modulus values to be evaluated with each load-unload increment, hence properties through the film thickness can be easily determined in one indentation test. This section examines and compares the modulus values obtained using the two types of indenter geometry, as well as the two different analytical methods for the spherical probe. A 100μm radius spherical indenter was used in this part of the experimental work to probe reference polystyrene sample as well as a clear paint coating. The two different analytical methods, viz., the Oliver & Pharr method in the case of continuous loading; and the Field & Swain method in the load-partial unloading mode were used to analyse the load-displacement data The results obtained are compared to the earlier results (section 4.1.1) obtained using the Berkovich indenter analysed with the Oliver & Pharr method.

Results for polystyrene and for a clear coating indented with a 100μm radius spherical diamond probe are shown in Table 4.7 and Table 4.8, respectively. Both the continuous loading (CL) and the load-partial-unload indentation (LPU) modes were

used, and the results were analysed using the Oliver and Pharr method for the former mode, and using the Field and Swain method for the latter.

Table 4.7: Modulus results for polystyrene indented with the spherical 100μm indenter.

Max. Load (mN)	E* for CL mode (GPa)	E* for LPU mode (GPa)
20	2.65 ± 0.08	2.38 ± 0.16
50	2.92 ± 0.06	2.53 ± 0.23
100	3.27 ± 0.54	2.86 ± 0.11
200	3.28 ± 0.01	3.10 ± 0.11
250	3.50 ± 0.05	3.13 ± 0.05

Table 4.8: Modulus results for clear coating tested using the 100μm spherical diamond indenter.

Indentation mode	Maximum load (mN)	E^*(GPa)
LPU	5	1.87 ± 0.10
LPU	3	1.73 ± 0.05
CL	3	2.04 ± 0.37

A noticeable difference was found in the results obtained for polystyrene using the two different testing methods. The modulus results appeared to be higher when the CL mode was used. Keeping in mind that only two data points used for the determination of the unloading stiffness in the LPU mode, it is not surprising that the results between the two modes were slightly different. The LPU mode generally gave lower results, since 50% of the unloading curve (partially unloading was set at 50% of maximum load at each sequential loading) was used in the determination of slope of the unloading curve, instead of the smaller % used in the case for the CL, and the slope of the unloading curve becomes less steep as unloading progresses, resulting in

lower stiffness and lower modulus values. For polystyrene, the E* value in general decreased with decreasing maximum load. This effect could be attributed to surface roughness, as explained in section 4.1.1. Higher loads would ensure that any asperities present would be “pressed down” and the results would be more accurate. For the clear coat, the trend was similar, although less pronounced.

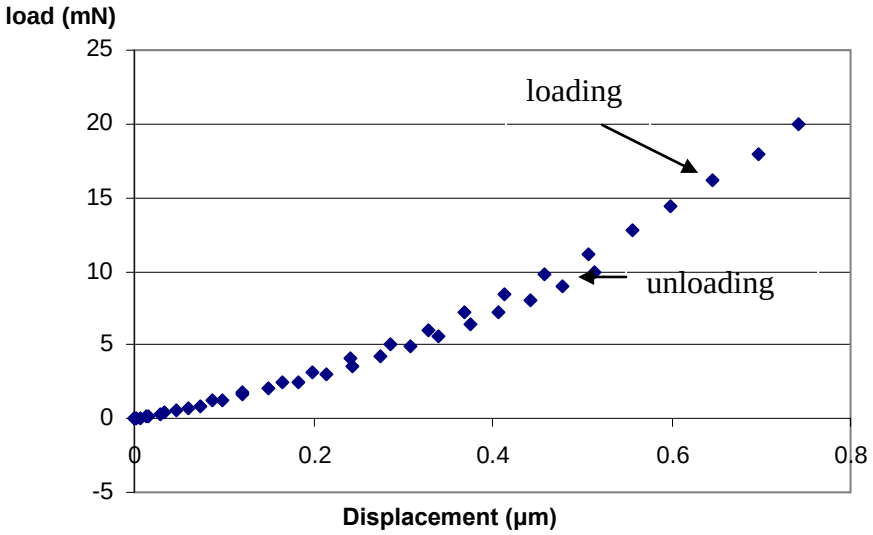

Figure 4.11: load and unload curves for polystyrene tested using LPU mode to the maximum load of 20mN. The lack of hysteresis indicates that little plastic deformation has occurred during indentation.

The E* values obtained for polystyrene using the spherical indenter were lower than those obtained for the Berkovich indenter (refer to section 4.1.1). Using the Berkovich indenter, an E* value of 4.3GPa was obtained. The same average value of 4.3GPa was obtained for polished polystyrene (1µm finish) tested using a 500µm radius WC probe, using a maximum load of 300mN (refer to Table 4.2). It would

appear then that the lower E* values obtained with the spherical indenter at lower loads (Table 4.7) were not due to indenter geometry, per se, but rather due to a slighter rougher surface finish, and to a lesser extent, scratches that might be present from manufacturing of the indenter tip. The polystyrene used for this part of the study was as-cast, without further grinding or polishing steps. The surface finish would be expected to be rougher than a 1μm surface finish. Unlike the other probes, area corrections were not carried out on the spherical indenter, as the indenter was newly purchased and certified to conform with regards to radius and shape. However, grinding marks from the manufacturing process might still lead to some degree of inaccuracies in the E* values (42). At the low forces used, however, the inaccuracies from asperities contacts would always be present and would overwhelm the effect of small imperfections of the indenter tip, thus defeating the use of standard materials to carry out area correction.

The results for the clear coating were similar for both testing methods, and at the two maximum loads employed. Very low maximum loads were used in these studies to minimise the indentation depth. The coating thickness is ~18μm, so the tip penetration should be < 2μm. Furthermore, the E* results (1.87GPa – 2.04GPa) compare well with those obtained using the Berkovich probe (2.2GPa as shown in Table 4.5). The maximum load effect is not evident for the clear coating, since it has a smooth surface finish and it is a very compliant material, and plastic deformation can take place even at very small loads.

Both the Oliver and Pharr method and the Field and Swain method worked well at generating acceptable results. The results of 2.7GPa - 3.5GPa for polystyrene were

comparable to those quoted in the literature [104]. Although the Field & Swain method might be less accurate as only two points were used for each partial unloading to generate E^* values, the method has an advantage since it is fast and thus less susceptible to thermal fluctuation in the environment. On the other hand, the Oliver and Pharr method employs curve-fitting to the unloading data which smooths out variations in the data.

4. 2 Nano-indentation

The feasibility of applying AFM type equipment to selectively probe different micro-regions within the paint coating was investigated. AFM imaging was carried out in Tapping Mode to visually assess whether the contact patch could be restricted to the paint matrix lying between the hard filler particles. Both height and phase imaging were carried out for the black, brown and white paint coatings, as shown in Figs. 4.12 to 4.14. In the figures, the left hand images show the height information, the lighter regions being higher and would likely indicate the presence of hard particles such as pigments and filler particles. The dark regions, on the other hand, would correspond to the paint matrix lying in between the hard particulates. The images on the right hand side show the phase differences which would indicate differences in surface chemistry and properties. It is expected that the high lying hard particles would not protrude through the paint coating entirely, and that some smaller or flatter particles would lie in between the larger particles. Thus the phase images would give a better representation of the surface distribution of the different constituents in the paint. The dark regions indicate the presence of hard particles that would interact to a lesser extent with the scanning probe than would the soft polymer matrix (lighter

areas). When both height and phase imaging are used in combination, a more complete picture is generated. It is interesting to note that the phase image for the white coating showed the least contrast, indicating that the hard particles at the surface were well covered by the paint. This could be due to the flat nature of the pigment. On the other hand, the pigments for the black paint appeared more rounded, while the brown pigments seemed flaky. From these images, it would appear feasible to probe between the hard particles at the paint matrix as the probe radius is reported to be less than 10nm by the manufacturer, and the tip opening angle was 34^{o}. From simple geometry, for an indentation depth of 1μm, the triangular projected contact area would have sides of 0.58μm, and the area would only be $0.17\mu m^2$. Hence it should be possible to indent between the hard particles (dark regions on the height image and light region on the phase image) for all three paints. Probing the polymer matrix properties directly in this way may prove to be more sensitive to the paint cure conditions than measuring the composite properties with larger size indenters.

In this part of the experimental work, the reference polystyrene sample was also used in an attempt to establish the accuracy of the AFM indentation technique.

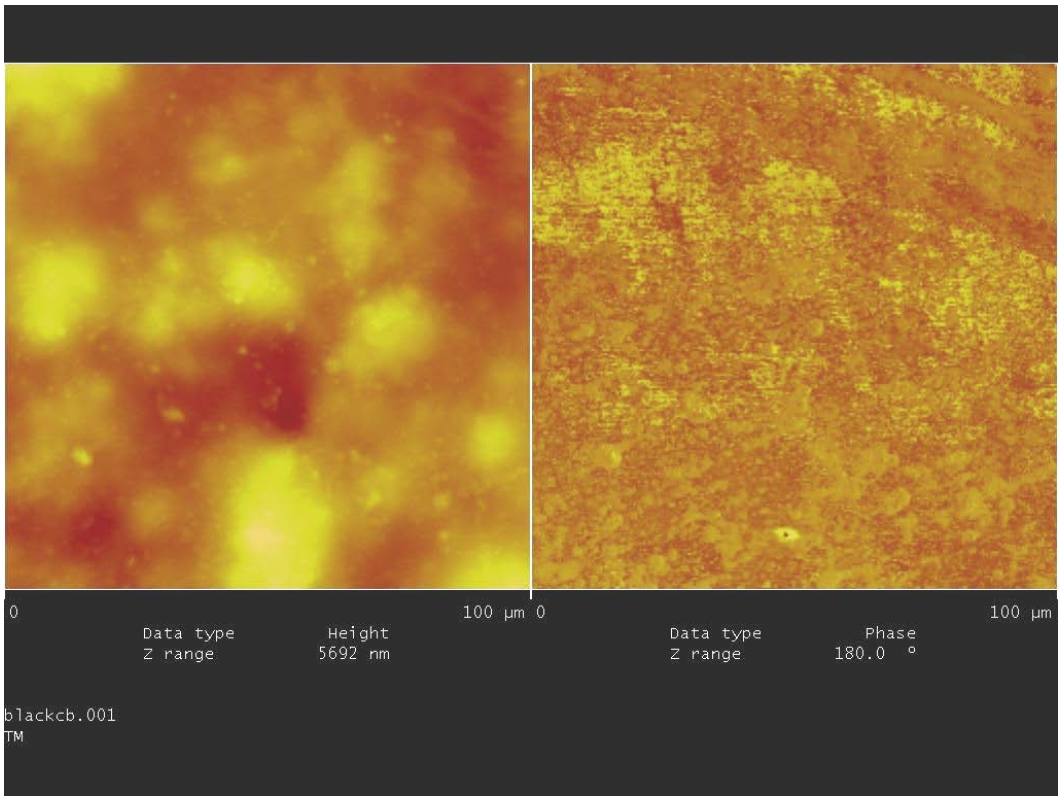

Figure 4.12: AFM tapping mode images for a black paint coating.

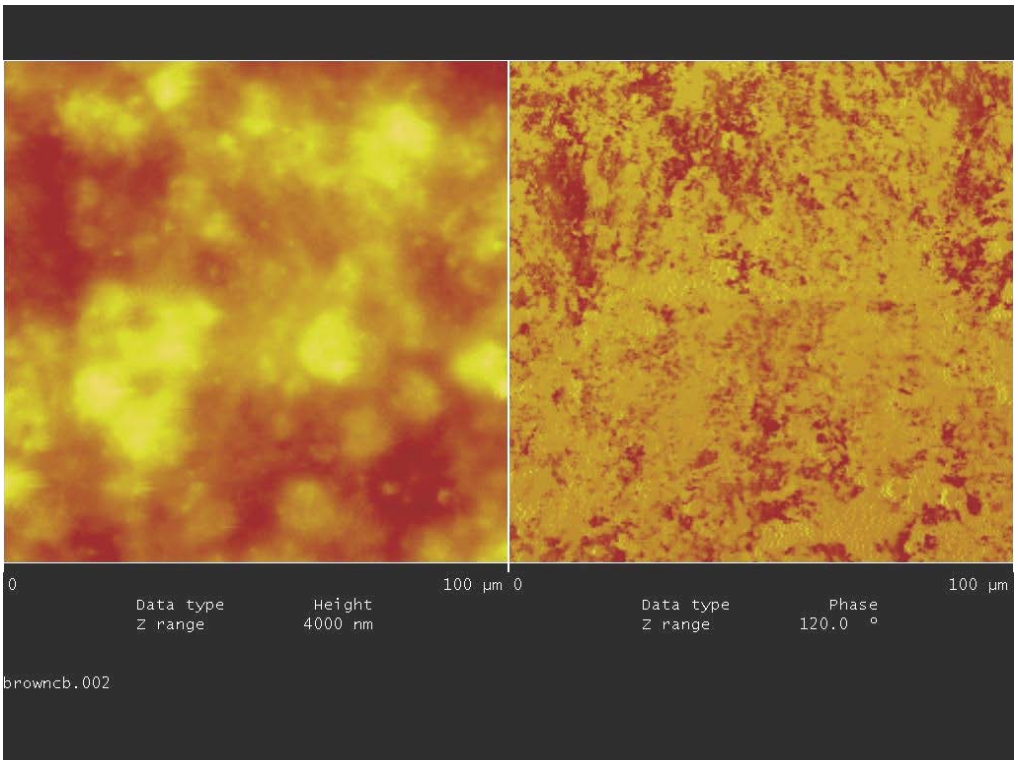

Figure 4.13: AFM tapping mode images for a brown paint coating.

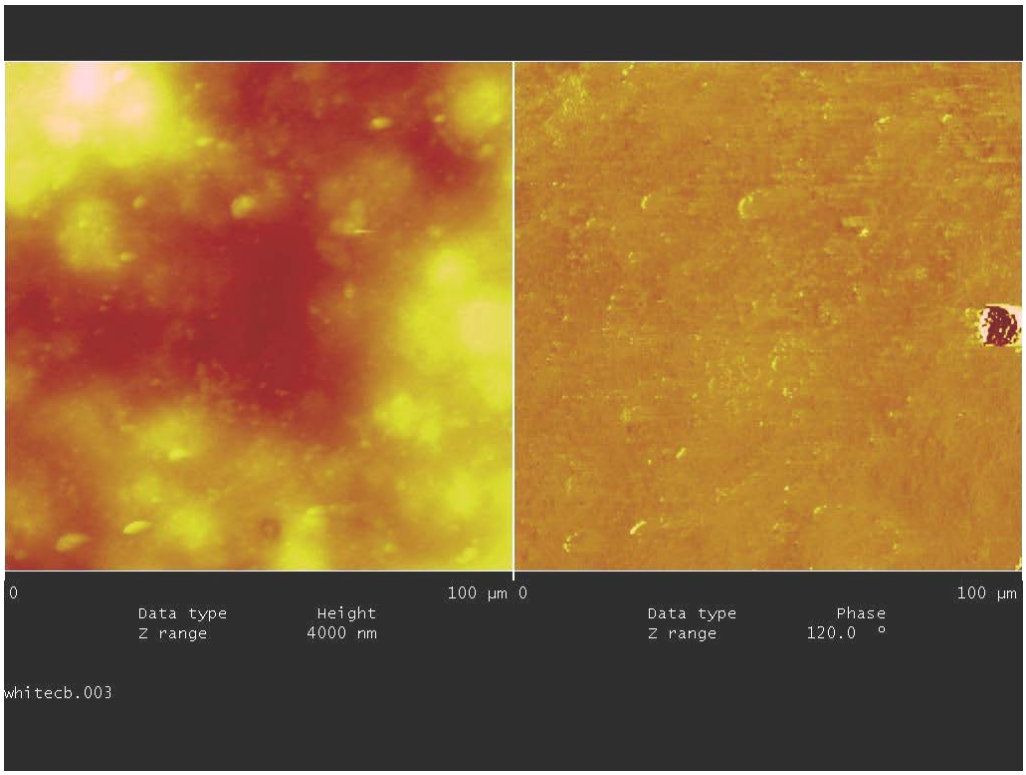

Figure 4.14: AFM tapping mode images for a white paint coating.

4.2.1 Force plots

As mentioned in the literature review, section 2.5.1, the force plot has become a common method to generate force-displacement data from which elastic modulus can be obtained, using appropriate analytical methods such as the Oliver & Pharr method or the Hertz elastic contact equation. A commercial AFM was first used to generate the force plots, using cantilevers with known stiffness. The cantilevers used for the experiments have stiffness values of 20.6N/m, 27.7N/m and 40.1N/m, as determined using the method outlined in section 3.3.3. Knowing the stiffness of the cantilevers, the deflection data can be converted to force data using Hooke's law (equation 2.27) once calibration on a Si substrate has been performed to establish the voltage to distance conversion for the photodiode. Calibration using Si was also

carried out to establish indentation into the paint material since the difference due to the data on the paint sample and the data on Si is due to the indentation of the material, assuming negligible indentation into Si. This assumption is reasonable since the maximum penetration recorded in a series of indentation into Si using a force of around 3.6μm resulted in a maximum penetration of only 4.5nm. In this part of the experimental work, the Si indentation curve showing negligible penetration was used.

Since the force plot data points for the test samples did not always coincide with those for the Si calibration sample, curve fitting and transposition procedures were carried out, resulting in the smooth appearance of the unloading curve (refer to section 3.3.3 ‘Data Processing’). The plot of cantilever deflection vs. piezo displacement is shown in Figure 4.15 for both silicon and polystyrene, while Figure 4.16 showed the unloading curve resulted from curve fitting (solid line). It is important to note that the curve fits the data point well except for the end of the unloading cycle, at low loads. However, this is not an issue as only the initial portion of the unloading slope is used in the modulus determination. Subtraction of the data for polystyrene from the data for Si gives the force-indentation curve for the polystyrene sample (Figure 4.17). The kinks observed in the loading curve in the final plot in Figure 4.17 were likely due to cantilever twisting, and was found to be more pronounced at higher loads and when hard materials such as polystyrene and Si were indented. The result showed an initial negative unloading slope, thus there was a need for a holding period before unloading, in order to counter the effect of creep.

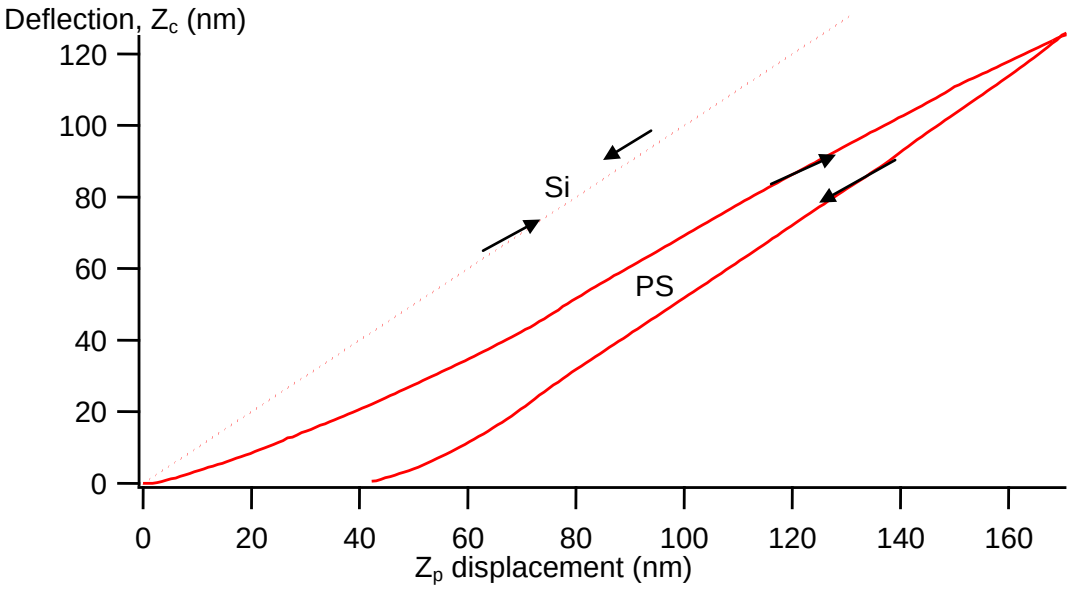

Figure 4.15: Force plot for silicon (dotted line) and polystyrene PS (solid line).

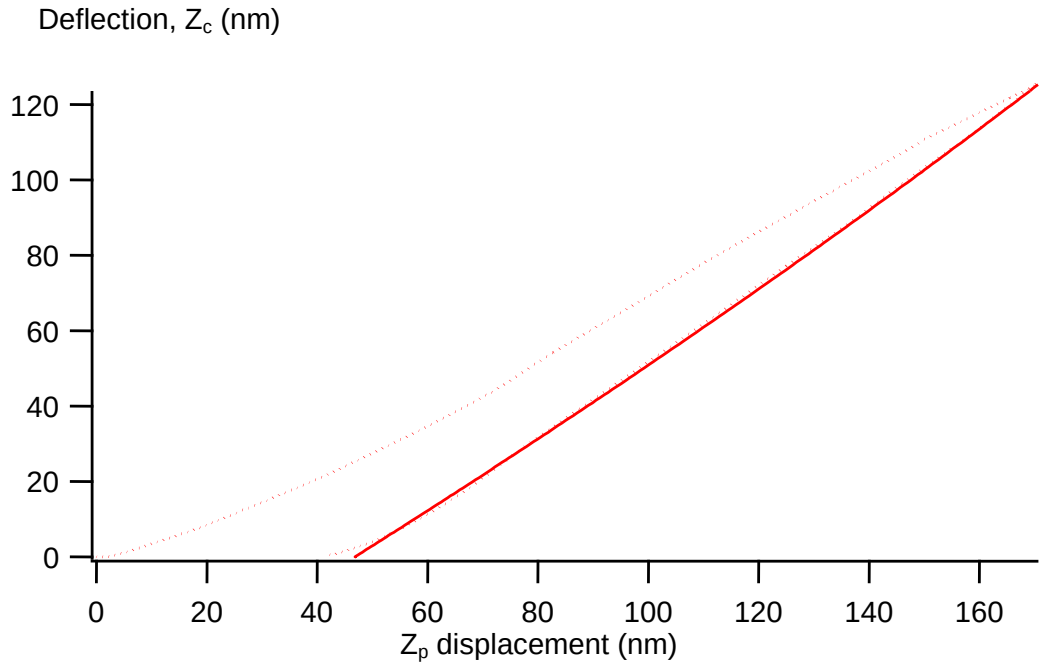

Figure 4.16: Force plot of polystyrene superimposed with unloading curve from curve fitting (solid line).

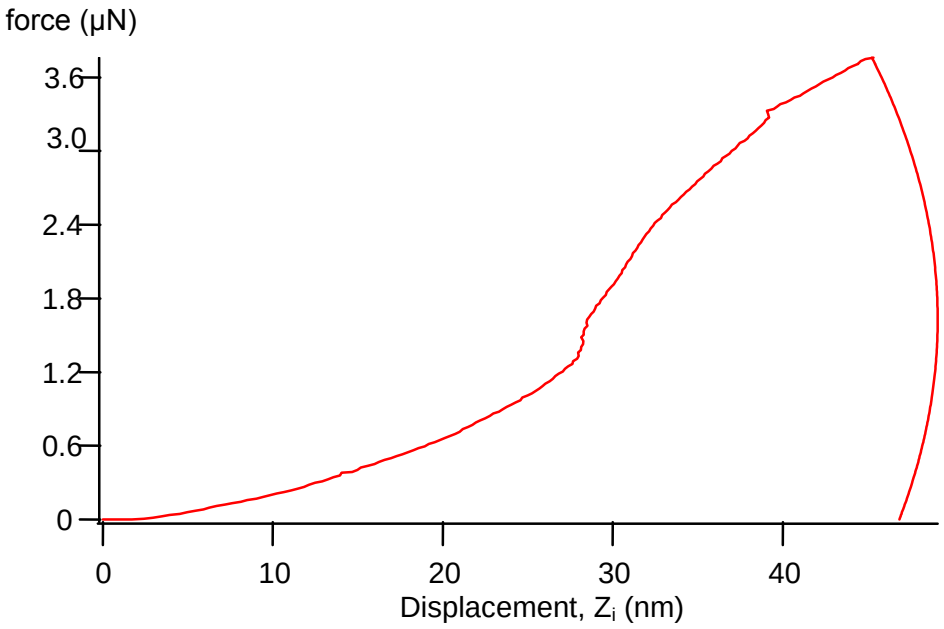

Figure 4.17: Plot of force vs. indentation displacement (Zi) for polystyrene.

Since the existing software on the AFM used did not allow for a holding period at maximum indentation, further experimentation work was carried out on the home-built AFM type equipment, the 'force rig'. The software on the force rig was altered such that the load-displacement data could be collected during loading, unloading as well as the holding period at maximum load.

A typical force rig plot generated for a black paint coating is shown in Figure 4.18. Two obvious observations can be made from this figure. Firstly, there is substantial noise in the deflection voltage signal; the vertical scattering is as much as 0.1V. Secondly, there is considerable drift in the deflection voltage signal over time, causing the voltage at the end of the unloading cycle to be higher than before the loading event. The noise problem in the deflection signal was further exacerbated after the Si subtraction step, as shown in Figure 4.19.

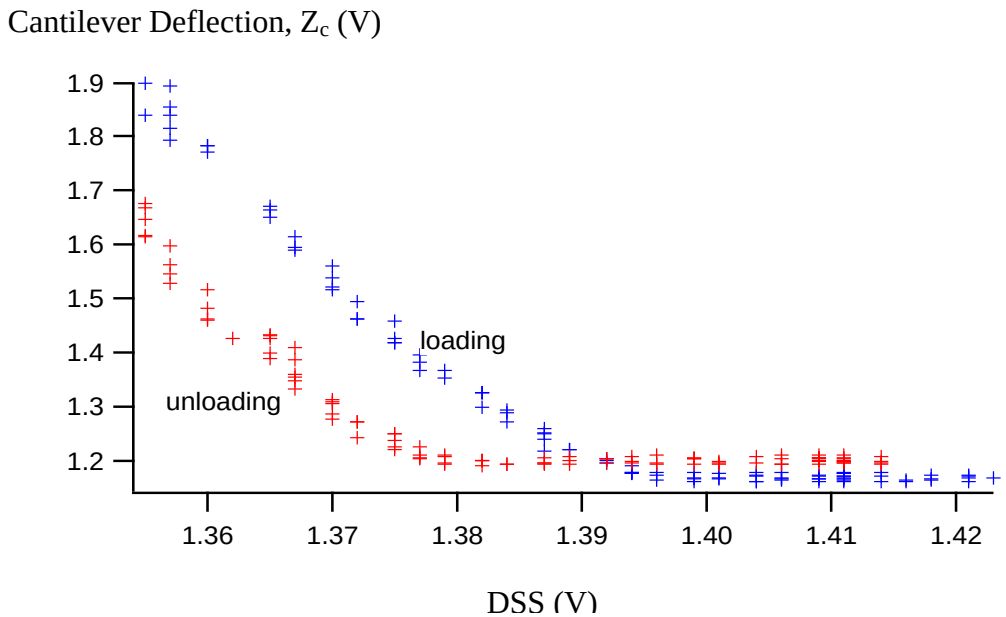

Figure 4.18: Raw data generated by the force rig on a black paint coating. Holding time before unloading – 3 minutes.

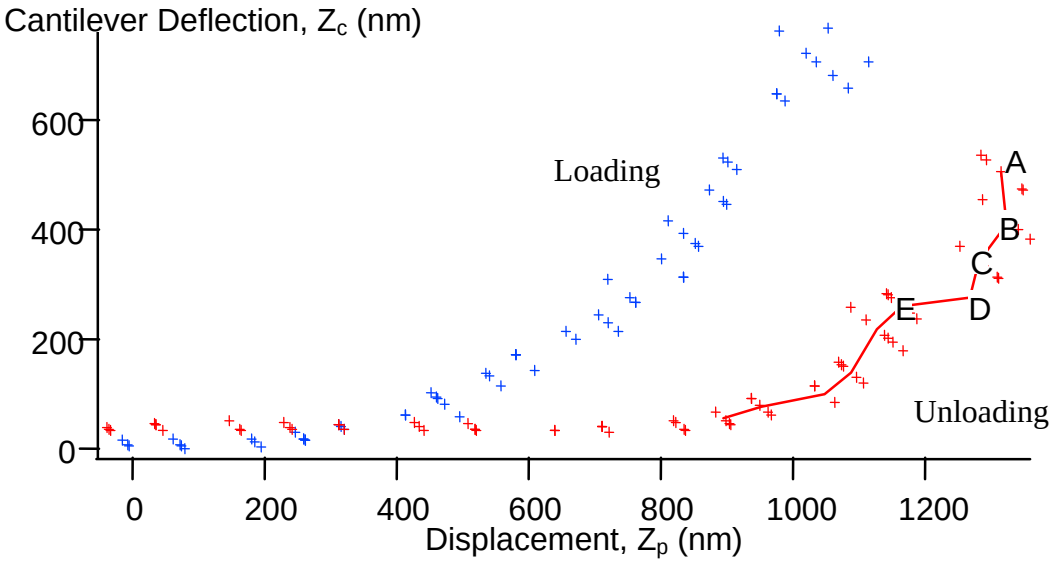

Figure 4.19: Cantilever deflection vs. displacement data for the same black paint coating (as in figure.4.18). A-E are points representing averaged values on the unloading curve.

The limitations of the equipment are immediately apparent from Figure 4.18. As mentioned before, the deflection noise is exaggerated after data processing. Even if this could be overcome by averaging, considerable error would be present. In Figure 4.19, the solid red line on the unloading curve represents averaged signals. This was an attempt to overcome the scattering in the data. Averaging was carried out on the original deflection signals (before the Si subtraction step) at the different DSS displacement point,. After using Hooke's law to convert the cantilever data on the y-axis to force and adjusting the zero position on the x-axis (zero position at around 400nm), the projected contact area can be calculated by analyses of the unloading data to obtain h_p, and using simple trigonometry to calculate the radius of the contact circle, since the indenter is a cone with known apex angle. This way, values of E* can be approximated at different positions (namely points A to E) on the unloading slope. In this case the plastic component of the indentation, h_p was estimated from the unloading curve in Figure 4.19 to be approximately 300nm. Hence the projected area would be 4206nm^2, and the E^* value can then be calculated using equation (2.10):

$$E^* = \frac{\sqrt{\pi}}{2}\frac{S}{\sqrt{A}}$$

The equation above shows the linear proportional relationship between E^* and S. It is evident from figure 4.19 that besides the large amount of scatter in the data, the shape of both loading and unloading curves near maximum loading (cantilever deflection) is irregular, possibly due to cantilever twisting. These effects on the determination of S and hence E^* by looking at hoe these values change at various points on the unloading curve (A-E). The modulus results estimated using different points (A-E) on the unloading slope are presented in Table 4.9. It should be noted that although using different points on the unloading curve (A to E) would result in

different h_p values and hence different contact areas, in reality the contact area resulting from the same indention test cannot change. Hence for the sake of illustration, a constant value is used for the projected contact area. The margin of error due to the estimation of the slope or stiffness S is large, and dependent on where on the unloading curve the slope was calculated, leading to large variations in the resultant E^* values.

Table 4.9: E* estimates at different positions on the unloading slope

Slope	Stiffness, S (N/m)	E* (GPa)
AC	51	0.69
AD	63	0.85
AE	24.4	0.33
AB	-238	-ve value
BE	16.8	0.23

The signal drift that caused the scatter in the original deflection data could only be corrected if it was shown to be some predictable function of time, and such predictable functions were not established. An even more serious shortcoming was that the initial unloading portion of the curve in Figure 4.19 was missing. This was caused by the probe sinking into the soft polymer due to creep, thus resulting in a decrease in cantilever deflection as creep progressed. Unfortunately, the combination of high stresses generated by the sharp cantilever tips and the compliant polymer material being tested would mean that creep would always be a serious issue. Unlike micro-indentation, the indenter in this instance was not rigid (since the cantilever bends and unbends) and there was no way for the applied force to be independently measured (except by the bending of the cantilever which deflects the laser spot). The missing data would mean that the slope of unloading curve at maximum load could

not be determined. From Table 4.9 it was illustrated that an accurate estimate of the slope was essential for an accurate estimate of the modulus value. Hence the creep phenomenon resulting in changes in the deflection or force data is a fundamental problem.

In summary, nano-indentation using AFM type equipment which relies on cantilever deflection to determine the applied force would always have the problem of decreasing deflection signal as the probe sinks into the material due to creep, thus causing the initial portion of the unloading data to be missing. A possible way to overcome this might be to reduce the load such that no permanent indentations are made, as per the work of Chizhik [63]. In their work on rubber and polystyrene, only the loading event was analysed, using appropriate elastic equations such as Hertz, JKR, or Sneddon. However, with compliant material such as polyester paint, having T_g close to ambient, low stress states might be difficult to attain with sharp cantilever tips. Increasing the tip diameter, such as by attaching particles to the end, might defeat the object of being able to isolate and probe the paint matrix properties in between pigment/filler particles. Due to these difficulties, further work on nano-indentation in this thesis was abandoned.

4. 3 Viscoelasticity in indentation

The mechanical properties of polymers are known to be time and temperature sensitive. When a polymer heats up to just below its T_g, for instance, it can be shaped and moulded quite readily. Also, a polymer sample subjected to tensile testing at a higher strain rate might appear stronger than at a lower strain rate. This time and temperature dependence is a consequence of the viscoelastic nature of polymers. In

indentation experiments, this viscoelasticity causes delayed indentation into the sample at the beginning of the unloading cycle, causing steeper, and even negative, unloading slopes. Since the Oliver and Pharr analysis method relies on the unloading slope to estimate the modulus of the material, viscoelasticity during unloading is clearly unacceptable if the O&P method is to be used. This section firstly examines the accuracy of the indentation technique in establishing the T_g of the material being examined. This verification was carried out using the DMA in indentation mode at elevated temperatures on reference polystyrene. The modulus results obtained at the various temperatures were then compared to those obtained on polystyrene using the same DMA in three-point bending for a bulk polystyrene beam. The second part of this section examines the accuracy of the various viscoelastic models in predicting the elastic modulus value. Lastly, attempts were made to use existing analytical methods to correct for creep in order that elastic equations (such as O&P) could be used to provide elastic modulus values in samples showing significant creep.

4.3.1 High Temperature Indentation

4.3.1.1 Establishing DMA Test Conditions

A commercial DMA instrument was used to investigate indentation of polystyrene at elevated temperatures. Temperature control was not available on the UMIS machine, so the first phase was to compare DMA and UMIS results on the reference sample (glassy polystyrene). Preliminary tests were carried out at 40 °C using the DMA with a spherical probe made of steel, at various loading conditions to establish suitable testing parameters. The radius of the spherical probe was measured by means of

optical microscopy to be 930μm with irregularities at the tip which will be discussed later on in this section. The indentation event can be separated into different components, viz., elastic, plastic (non-time dependent) and a delayed response, creep, which could be viscoelastic or viscoplastic. However, since creep displacement could be fully recovered during the unloading hold (refer to Figure 3.12 for an example load-displacement curve), and since a spherical indenter would generally induce less stress in the specimen beneath, one can assume that there was no significant visco-plasticity present. If the unloading rate was sufficiently fast to limit creep responses, then the elastic component would be immediately recoverable after unloading, and elastic contact equations, such as those employed in the Oliver and Pharr analysis method, could be valid.

The DMA provides indenter displacement data at incremental increases in force. An indentation test conducted at 40^{o}C to a maximum force of 0.5N at a loadind/unloading rate of 3N/min is shown in Figure 4.20 below. Manipulation of the raw data involved determining where zero indentation point is on the x-axis, and then converting the indenter displacement to positive values. From there the O&P analysis can be carried out.

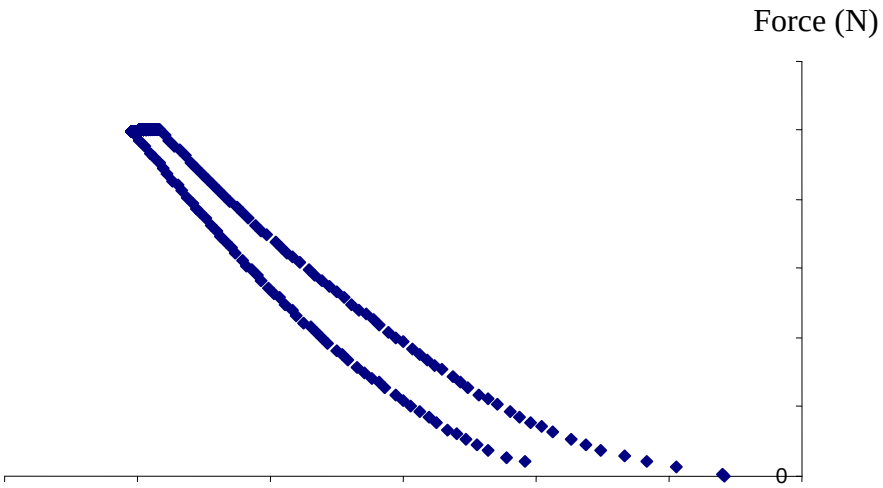

Figure 4.20: DMA indentation test raw data at 40°C.

The results for stiffness S and modulus E^* are shown in Table 4.10 for two different loading rates, several maximum loads and two different hold times.

Table 4.10: Preliminary test with varying loading conditions at 40°C

Loading/ unloading rate, holding time	Max. load (N)	S (mN/μm)	E*(GPa) – O&P
3N/min, 10 minutes	0.5	230.8 ±13.8	1.84 ± 0.13
	0.7	251.3 ± 5.5	1.89 ± 0.17
	3	293.3 ± 5.1	1.48 ± 0.07
	6	316.3 ± 11.4	1.16 ± 0.13
3N/min, 20 minutes	3	276.9	1.39
18N/min, 10 minutes	0.7	250.8 ± 8.7	2.03 ± 0.08

Overall the E* results, were low (1.16 – 2.03 GPa) as compared to previous results obtained using the UMIS, which gave E* values close to 4GPa. Both experiments (DMA and UMIS) were conducted well below the T_g of polystyrene where the modulus is expected to be 3-4GPa. In the open literature, work by Rudd and Gurnec [106] indicated that the flexural elastic modulus of polystyrene decreases linearly with temperature from -198^{o}C to 24^{o}C, which meant a decrease of 5.31 MPa/^{o}C and a total decrease of 85MPa from 24 to 40^{o}C, if the linear relationship was extrapolated to 40^{o}C. In section 4.3.1.2 modulus values obtained using 3-point bent test indicated a decrease of around 10MPa/^{o}C at around 40^{o}C. If we use the E* value of 4.3GPa obtained in section 4.1.1, and assume an overall decrease in E* value of 0.1GPa from room temperature to 40^{o}C, then the modulus value of 4.2GPa would be expected from indentation test at 40^{o}C.

The slow data acquisition speed available in the DMA system has placed a bottom limit to the lowest maximum load that could be used in order to generate sufficient data points for regression analysis of the unloading slope. A higher maximum load would take longer time to attain and thus a larger component of creep would be present in the displacement data. At the loading rate of 3N/min, the time to reach maximum loads of between 0.5N and 6N would be from 10 seconds (for 0.5N) to 2 minutes (for 6N). In comparison, a typical indentation test using the UMIS would take around 2 seconds to reach the maximum load of 5mN. Therefore creep can no longer be ignored in the displacement data for the higher maximum loads using the DMA.

In the case for the O&P analysis, E* is proportional to $\frac{S}{h_p}$. The increase in the unloading stiffness or slope S with increasing maximum load (Table 4.10) is indicative of increasing creep, since longer times are required to attain higher maximum loads. However, the overall E* values decreased slightly with increasing maximum load, thus suggesting that the error in h_p due to creep is affected to a larger extent by the maximum load. Indeed, higher load would result in higher stress and strain in the specimen under the indenter, to an extent that creep could be significant in the loading and unloading segments. The steeper unloading slope would cause h_e values to be lower than expected, while the h_p value would be over estimated, not only by the error in h_e, but also by having an added creep component. When different loading rates were used, the faster loading rate (18N/min) appeared to yield a higher value of E* since less error would be expected in the displacement data due to creep. However, the difference in E* were not statistically significant once the standard deviation was considered. Thus it could be concluded that for the experimental conditions considered, the maximum load affected the E* values most significantly. The differences between the loading rates and the holding times used were not a significant factor contributing to the differences in the observed E* results, in this instance. In addition, the surface roughness effects of the specimen were masked by the increasing creep effects, with increasing maximum load.

The generally low modulus values were most likely due to the imperfect indenter shape. A profile of the indenter tip is shown in Figure 4.21. Figure 4.21 showed that the indenter has a flat spot at the tip, at a distance of about 20μm from where the tip should have been. On rotating the probe by 180^o, the flat spot was no longer observed; instead, a slight ‘hump’ was evident. This ‘hump’ protruded at roughly 25

to 30μm from the tip and had a radius of around 590μm, as opposed to the larger radius of 930μm for the indenter. The imperfect shape at the tip was probably a manufacturing fault and area correction was attempted. If the expected modulus result is denoted E_i^* and the ideal radius of the contact circle is a_i, then

$$E_i^*/E^* = a/a_i$$

Using the above equation and different maximum loads to induce different plastic displacement, h_p, and knowing the ideal modulus value of a reference material, then the correction factor (a/a_i) could be determined for a range of h_p. It should be noted that area corrections, in fact, is a standard feature in commercial indentation software to correct for imperfect indenter shapes. The correction factor (ratio of actual to ideal area) is stored as a function of plastic deformation depth.

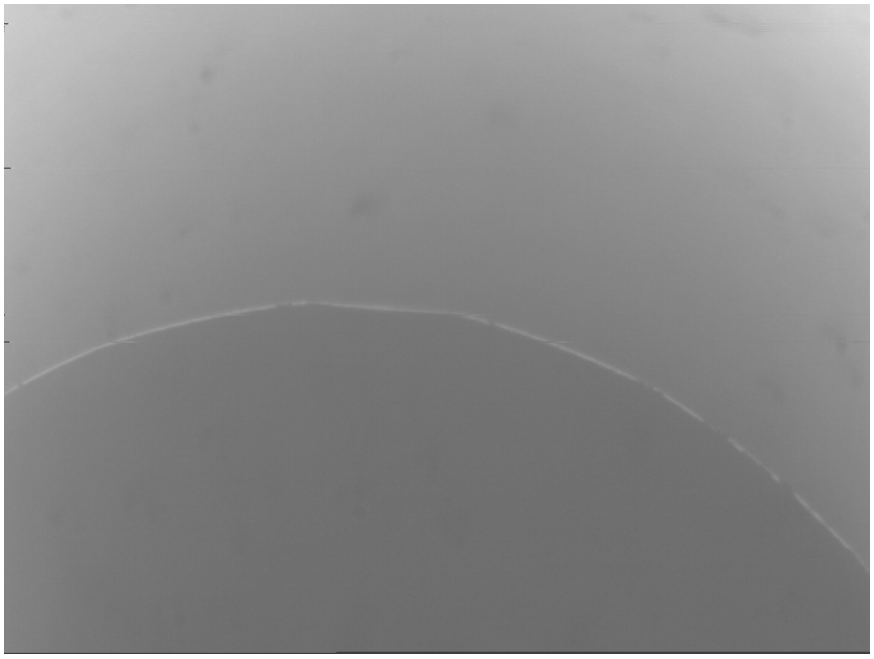

Figure 4.21: Showing flat spot at the indenter tip. 100X

Using the indentation test results for the lowest indentation loads of 0.5N and 0.7N and the loading rate of 18N/min (to ensure validity of the O&P method), a plot of

correction factor a/a_i vs. h_p was constructed, as shown in Figure 4.22 below. The correction factor for h_p in the range 2.5-3.5 was determined to be 2.42 (± 0.08), and for h_p between 1.5 – 2.4, the correction factor was slightly lower, at an average value of 2.16 (± 0.10).

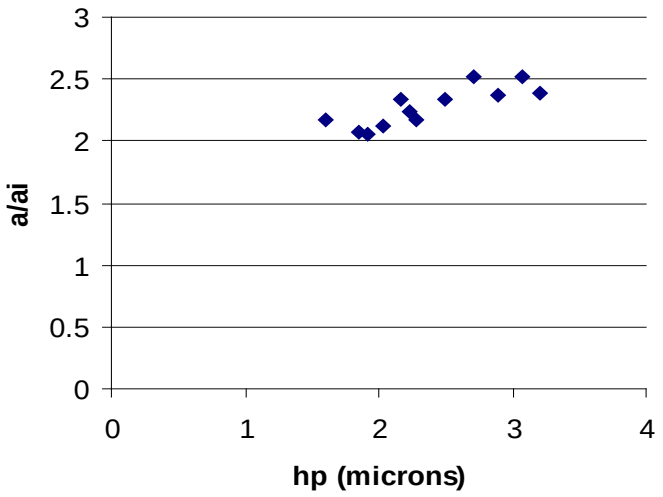

Figure 4.22: plot of correction factor vs. plastic displacement, h_p for the spherical indenter used on the DMA equipment.

It would appear that lower loads were more suitable since they yield better E* values. Using the correction factor, the revised modulus values are 4.13 ± 0.16 GPa and 4.07 ± 0.36GPa, respectively, for the maximum load of 0.5 and 0.7N (at 3N/min loading rate), and 4.39 ± 0.17 GPa for a maximum load of 0.7N at the higher loading rate of 18N/min. Since the results for 0.5N and 0.7N were similar, the latter was chosen as more data points could be captured during the loading and the unloading cycle. At higher temperatures (110°C and higher), the load was decreased to 0.2N in order to attain similar penetration depths (before creep) when compared to the 40°C penetration tests. A loading rate of 18N/min was selected to reduce creep effects,

particularly at the higher temperatures. The holding time of 20 minutes did not have a significant effect on the modulus values and for practical reasons a shorter holding time of 10 minutes was selected.

4.3.1.2 Effect of Temperature on Indentation Behaviour of Polystyrene

DMA results at varying temperatures are tabulated in Table 4.11, obtained using a loading (and unloading) rate of 18N/min to a maximum load of 0.7N and holding for 10 minutes before unloading. At higher temperatures of 105^{o}C and above, the resultant indentation could be directly observed (whereas at lower temperatures, elastic and visco- elastic recovery rendered the resultant residual indent too shallow to be determined optically). Assuming that elastic recovery occurs along the axis of indentation, then the radius of the contact patch, *a*, would remain unchanged upon unloading, and would be equivalent to the radius of the residual impression which could be determined using an optical microscope. Thus more accurate values for modulus could be obtained. The measurements were done after the sample had cooled sufficiently and after sufficient time (at least 10 minutes) had lapsed to allow for viscoelastic recovery. The revised modulus values based on the direct measurement of plastic deformation are also shown in Table 4.11, marked with †.

Table 4.11: DMA results - modulus values obtained at different temperatures.

Temperature (^oC)	S (mN/μm)	E* (GPa)-O&P	E* (GPa) –O&P, contact area corrected
40	250.8 ± 8.7	2.03± 0.08•	4.39 ± 0.17
60	256.8 ± 2.3	1.86 ± 0.19	4.01 ± 0.40
80	280.0 ± 7.0	1.94 ± 0.08	4.19 ± 0.17
100	312.7 ± 1.0	1.60 ± 0.16	3.46 ± 0.35
105	342.5 ± 61.8	1.86 ± 0.23	0.35 ± 0.05†
110	247.5 ± 37.4	1.40 ± 0.52	0.22 ± 0.03†
115	150.0 ± 51.1	0.47 ± 0.23	0.12 ± 0.04†

•value as shown previously in Table 4.10 for a loading/unloading rate of 18N/min, 10 min holding time.

The results from classical three-point bend test on a polystyrene (PS) beam are shown in Figure 4.23. Note that at 115^{o}C, the software returned a negative value for storage modulus, since the sample was too soft to be tested. Examination of the raw data showed that these negative modulus values were the result of negligible negative forces in the order of 10^{-4}N. Thus, for the sake of representing this low value in the plot, it was shown as having a zero value. For comparison, the modulus values obtained after correcting for contact area are also shown in the same figure. The T_g obtained from both methods and taken as the temperature of rapid decrease in E^* was similar, at 105^{o}C – 110 °C. It should be noted that the modulus values obtained in the three-point bend test are similar to those obtained using the indentation method.

Error!4.5

4.5

4.5

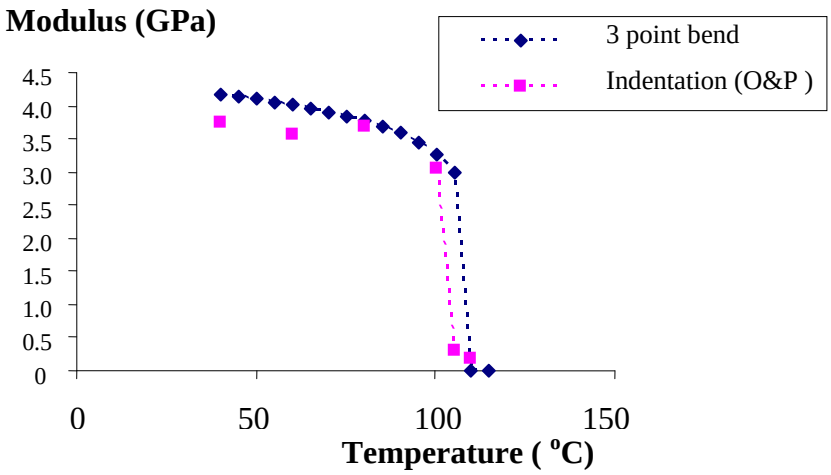

Figure 4.23: Showing T_g as the sudden decrease in modulus obtained from different testing modes using the DMA.

The T_g for polystyrene determined from indentation methods using the Oliver and Pharr analysis technique, compared well to that obtained using the three-point bend test, after area correction. Errors for the 3-point bend test would most likely come from dimensions of the sample, estimated to be in the order of ±0.01mm, resulting in modulus errors of +0.36GPa and -0.31GPa, an error band of 0.7GPa. The O&P method (before area corrections) predicted a T_g at over 115 °C, since the E* values only began to drop at this temperature. From the data given in Table 4.11, it can be seen that the value of S steadily increases, as temperature was increased up to 105 °C. A larger value of S due to creep would result in an underestimation of h_e, from regression analysis. However, h_p values would be over-estimated. The overall effect could be a decrease in modulus, as already shown in the preliminary test results (Table 4.10). Thus the decrease in E* was likely to be a result of a combination of creep effects on the analysis as well as of actual changes in materials properties. As

temperature was increased further, the material behaved more like a viscous fluid, resulting in a drastic increase in creep. The extent of creep with increasing temperature could be observed by comparing the creep displacement during the holding period of 10 minutes. The creep displacement increased from around 0.3μm at 40 °C to over 10μm at 105 °C. Despite the reduction in maximum load at 110 °C and 115°C, the creep displacement during the holding period increased drastically to over 200μm and over 300μm, respectively. This drastic increase in creep displacement, in itself, would indicate changes in material property and behaviour, indicating that T_g has been reached.

In the O&P analysis, error in the estimation for both the S and the h_p values at temperatures close to T_g would both affect the E* results. Fortunately, the contact area (affected by h_p) at higher temperatures could be directly determined by measuring the size of the residual indentation; and the error in the S value could be further corrected using the Boltzmann superposition principle, which will be presented later in section 4.3.3.2. Thus, corrections could be applied to yield more accurate E* values using the O&P method. For example, at 105°C the estimated contact area was ~92μm, but the actual area measured was ~490μm. This 5 fold increase in contact area resulted in a five fold decrease in the estimated E* value, from 1.86GPa to 0.35GPa. Similar drastic changes in contact area was observed at the higher temperatures of 110 and 115°C, resulting in lower and more accurate values of E*.

In summary, the Oliver and Pharr method yielded reasonable results once the contact area correction was applied (to correct for the flat spot at the indenter tip). At higher

temperatures, creep deformation became dominant, and although a decrease in modulus was shown, the error due to creep in both the loading and the unloading segment would be expected and should be bear in mind. Despite this, the indentation tests gave reasonable estimates of T_g for polystyrene. The accurate determination of modulus, however, was shown to be strongly affected by creep, especially at temperatures close to T_g. Thus, models that include a time-dependent strain were considered for better analysis of indentation of polymers.

4.3.2 Mechanical models

4.3.2.1 The EVEV model

As mentioned earlier, the major drawback in using elastic contact equations in indentation analysis for compliant polymeric materials is the materials' tendency to creep at ambient temperature. Thus the measured elastic modulus is dependent on holding time (at maximum load), maximum load, and loading/unloading rates. Attempts have been made to derive empirical models to fit the creep data during indentation. Such models would give viscoelastic parameters of the material so that time-dependent modulus, creep and stress relaxation could be calculated for any loading condition. This section describes the work by Yang et al. [84] in which an elastic-viscoelastic-viscous (EVEV) model to describe the creep behaviour of polymers was proposed, for a flat-ended punch indenter and a Bervovich tip. The authors claimed that the elastic modulus could be calculated using the empirical formula derived from their model. Thus, the derived elastic modulus would be

independent of the unloading data, i.e., independent of holding time and unloading rate.

Using a generalised Kelvin model for a flat punch indenter, an equation for indentation strain, ε, could be derived as shown in equation (2.64), Section 2.6.1. Furthermore, by introducing the concept of virtual length, h_{in}, such that $\varepsilon = h/h_{in}$, an equation for the indentation displacement h could be obtained (refer to equation 2.67). Virtual length h_{in} was defined as the displacement before creep begins. The equation could then be used to fit the creep data; and the elastic modulus could be obtained from the first term of the equation, i.e., from the instantaneous displacement of the first spring element, equivalent to the elastic displacement of the system, in accordance with equation (2.68);

$$E_0 = \frac{P_0 h_{in}}{A_0 h_e}$$

where A_0 is the contact area at the end of the loading cycle when maximum load, P_0, is reached.

Yang et al. applied their EVEV model to analyse the indentation of PMMA, PS, PET, PC and Epoxy, using both a flat punch and a Berkovich indenter. The authors noted two major differences in the experimental results obtained with the two types of tips. Firstly, the Berkovich tip caused more significant plastic deformation during loading. The plastic deformation h_p was, therefore, subtracted from the total displacement prior to modelling of the indentation creep data. The elastic deformation (and hence the plastic deformation) was determined using the unloading data, using the Oliver and Pharr method. Secondly, the contact area would no longer be a constant, but instead would change with indentation depth for the Berkovich tip.

The authors defined A_0 as the contact area before creep and in the experimental work outlined in this thesis; A_0 was calculated using the Oliver and Pharr area function, assuming an ideal Bervokich tip, as mentioned previously in section 2.4.3.1:

$$A_0 = A(h_p) = 24.5h^2_p$$

More specifically, the plastic displacement, h_p, is related to the displacement before creep, h_{ep}, and the elastic displacement, h_e, through:

$$h_{ep} = h_e + h_p$$

Since the value of h_{ep} can be directly obtained in an indentation test, the estimation of the elastic displacement using the Oliver and Pharr analysis of the unloading slope will yield h_p and then A_0.

In order to restrict the creep response to the holding (constant load) segment, a fast loading and unloading rate should be used, and the holding time should be as long as possible. However, in practice the loading rate and unloading rates are limited by equipment capabilities. The maximum load is sometimes not attained or load overshoot may result if too fast a loading rate is used. Also thermal fluctuations can occur during long holding periods. Therefore, the effect of loading conditions is also considered in this section, together with the results attained for polystyrene and paint coatings.

Effect of Maximum Load and Loading Rates

Polystyrene was indented using a Berkovich indenter at 10mN and at 5mN maximum loads, and at the loading rates of 2.5mN/s and 5mN/s for both loads, using the UMIS 2000 at ambient temperature. Besides employing different loads and loading rates, the technique employed was as described in section 3.2.3. The samples were allowed to creep at the maximum load for 20 minutes. The unloading rate used for all the tests reported in this section was the same as the loading rates. The creep results were fitted using the EVEV model and the resultant E^* values are tabulated in Table 4.12.

Table 4.12: E^* values obtained for polystyrene at ambient temperature at different maximum loads using the EVEV model.

Maximum load	Loading rate	
	2.5mN/s	5mN/s
10mN	2.05 ± 0.14 GPa	2.16 ± 0.08 GPa
5mN	2.47 ± 0.17 GPa	2.39 ± 0.18 GPa

The results indicate that there was a slight decrease in the modulus values as the maximum load was increased, for both loading rates, while the results at the same maximum load for the different loading rates were similar. The overall modulus values obtained were at the lower end of the range quoted in the literature [104] of 2.3 - 4.1GPa for polystyrene (obtained through tensile testing of bulk material). Also the E* values were lower than those obtained with the Berkovich indenter using the UMIS 2000 (E* = 4.3GPa), as shown in section 4.1.1 and analysed using the O&P method.

One possible explanation for the different results reported in this section (EVEV model) and section 4.1.1 (O&P analysis) relates to imperfections in the Berkovich indenter shape. Since the contact area calculation assumed a perfect tip shape, deviations of the actual contact area, A_r, from the ideal contact area, A_i, were considered. Also, indentation tips are prone to damage with extensive use, and hence the E* results were routinely checked using reference polystyrene; using the same testing conditions as for the repeatability test (refer to section 3.2.3). Since large deviations were observed, more extensive testing over a range of maximum loads (to cover a wide range of penetration depth) was carried out on polystyrene. The E* result from the software, E_r*, obtained using the O&P method, was compared to the expected E* result of 4.3GPa for polystyrene (obtained previously from repeatability test, section 4.1.1). The ratio E_r*/4.3 was then used as a correction factor. In addition, according to the O&P analysis:

$$E^* \propto \frac{1}{\sqrt{A}}$$

Therefore

$$\frac{4.3}{E_r^*} = \frac{\sqrt{A_r}}{\sqrt{A_i}}$$

which means that the correction factor $\left(\frac{\sqrt{A_r}}{\sqrt{A_i}}\right)$ directly relates to the tip imperfections. Figure 4.24 represents the deviation of the ratio $\sqrt{A_r/A_i}$ as a function of h_p. The ratio corresponding to a certain plastic penetration depth can then be used as a correction factor in the E* calculation in the EVEV model to yield better estimates of E* (Figure 4.24). As shown in Figure 4.23 the error introduced by the

tip shape is more significant at smaller indentation depths, but approaches the ideal shape (A_i=A_r) for plastic indentations greater than 2µm.

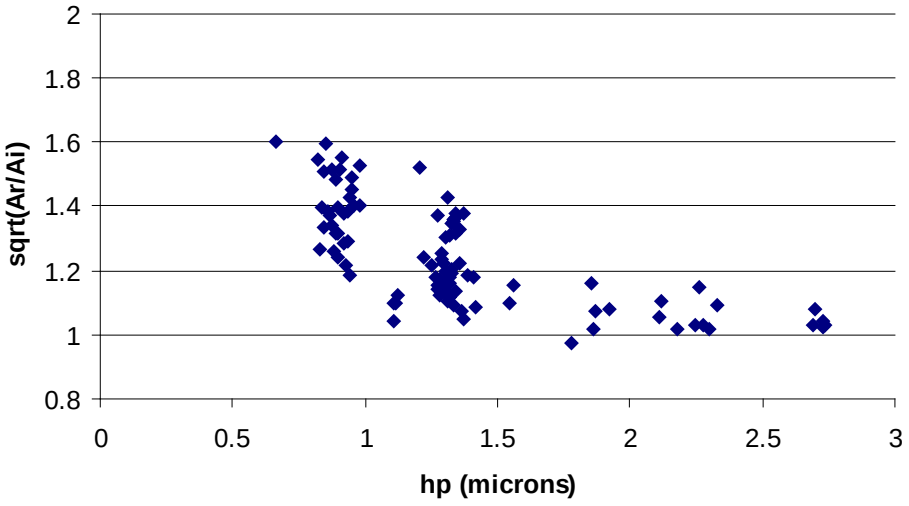

Figure 4.24: Showing deviations from ideal tip shape ($\sqrt{A_r / A_i} = 1$) as a function of plastic penetration depth.

Indentation tests used to generate data for the EVEV model analysis used maximum loads to 10mN. For the maximum load of 10mN, the amount of plastic penetration ranged from around 1.16 to 1.30µm. Unfortunately, there appeared to be a large amount of scatter in the results shown in Figure 4.24 for this range of plastic penetration. The corresponding correction factor lies within the values of 1.02 to 1.52. Taking the average E^* value for the maximum load of 10mN at the two loading rates to be 2.1GPa, and applying the correction factor, results in a corrected E^* value anywhere between 2.1 and 3.2GPa. Similarly, for the maximum load of 5mN, the h_p range lies between 0.74 and 0.8µm, with the corresponding correction factor lying within the values of 1.2 and 1.6. The revised E^* value for an average E^* of 2.43GPa would be 2.9 to 3.9GPa. The corrected E^* values are more reasonable, and compare

better to the range of modulus values reported in section 4.1.1 using the O&P analysis and the UMIS 2000 (E*=4.3GPa). However, due to the large amount of scatter in the correction factors used, clear conclusions cannot be drawn regarding the effect of maximum load and loading rate for polystyrene at room temperature. Given that creep effects are likely to be small for polystyrene at room temperature, it is perhaps not surprising that the EVEV model did not show any advantage over the Oliver and Pharr method. Further evaluation of the EVEV model was undertaken on the more viscoelastic paint coatings.

Paint coatings

These tests were carried out using the slower loading rate of 2.5mN/s to avoid load overshoot and at a range of loads to balance surface roughness effects and substrate effect. Elastic modulus values for the different paint coatings tested at different loads, but using the same loading rate of 2.5mN/s and extended holding time of 40 minutes, are summarised in Table 4.13, after correction for the contact area. For each correction, the mean correction factor corresponding to the range of plastic penetration was used. For example, the white coating tested at the maximum load of 5mN exhibited plastic penetration ranging between 0.86 and 1.18μm, and the corresponding correction factors would be in the range of 1.2 to 1.6. Hence the mean value of 1.4 was used for the correction factor. The same test data were re-analysed using the classical Oliver and Pharr method for comparison, and the results are also shown in Table 4.14. Again, the results have been corrected for deviations from the ideal contact area. It should be noted that the total penetration for all the paint coatings were close to and, in the case of the clear coat, exceeded 1/10 the coating thickness, which was at around 20μm. It should be noted that the 1/10 thickness rule

is only a rough guideline. In the case of soft coatings on steel, using a sharp indenter, the substrate influence might be felt at lower indenation depths. The results may, therefore, be influenced by the substrate. In general, EVEV model gave larger E* values than the classical O&P method. Surprisingly, the E* values appeared to decrease with increasing maximum load for the EVEV model, but increased with increasing load for the O&P method. For both methods, the clear paint appeared to have a larger E* value than the black coating. The unreasonably high value for the clear paint could be a combination of substrate effects and significant creep in the unloading segment. Lower loads were not considered due to the high standard deviations for the results. Both O&P method and EVEV model, therefore, could not provide acceptable modulus determinations for highly viscoelastic coatings.

Table 4.13: E* values of the three paint coatings at varying maximum load, using the EVEV model.

Coatings	Maximum load			
	5mN	2.5mN	1.5mN	1mN
White	6.76 ± 1.09GPa			
Black	3.54 ± 0.31GPa	4.55 ± 0.80GPa	5.83 ± 1.16GPa	4.57 ± 0.74GPa
Clear				5.78 ± 0.90GPa

Table 4.14: E* values of the three paint coatings at varying maximum load, using the Oliver and Pharr method.

Coatings	Maximum load			
	5mN	2.5mN	1.5mN	1mN
White	6.08 ± 1.32GPa			
Black	3.65 ± 0.54GPa	3.30 ± 0.71GPa	3.06 ± 0.61GPa	2.08 ± 0.42GPa
Clear				2.21 ± 0.88GPa

Discussions on the EVEV model

The EVEV model fitted all the creep data well. Some typical curves are shown in Figure 4.25 and Figure 4.26. The h_e value obtained from curve fitting was comparable to that obtained from the Oliver and Pharr method, particularly as the number of elements used was increased for the generalised Kelvin model (Table 4.15). Recall from equation (2.67) that

$$h = h_e + \sum_{1}^{n} h_i (1 - e^{-t/\tau_i}) + t/\mu_0$$

Also,

$$\tau_i = \frac{E_i}{\eta_i} \quad \text{and} \quad \mu_0 = \frac{\eta_0}{h_{ep}},$$

where E and η represent elastic modulus and viscosity coefficient, respectively. Table 4.15 shows the changes in parameters (the most important being the h_e values) as the number of exponentials, n, or elements was changed in the analyses of a number of creep experiments for polystyrene. Note that there were slight differences in the values of h_e derived between using three and using five exponentials in the model, and the five exponentials were used for all curve fitting purposes. The h_e values obtained from the EVEV model compared well with those obtained from the O&P method. The latter are also shown in Table 4.15. Note that the values h_1 to h_5 are quite small compared with the h_e value, indicating that there was not much time-dependent indentation occurring in this material. Also, μ_0 is high, so viscous flow is small. The retardation time τ_1 is much smaller than τ_2 to τ_5, suggesting movement of the segments of main-chain and side groups. Large τ_2 to τ_5 values, on the other hand, might suggest movement of large molecular structures.

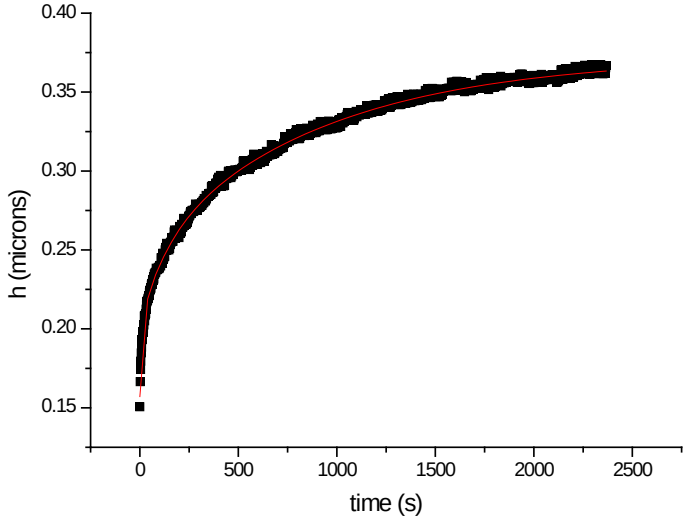

Figure 4.25: Typical plot obtained from creep experiment on polystyrene. Curve fitting using the EVEV model is shown as the superimposed line.

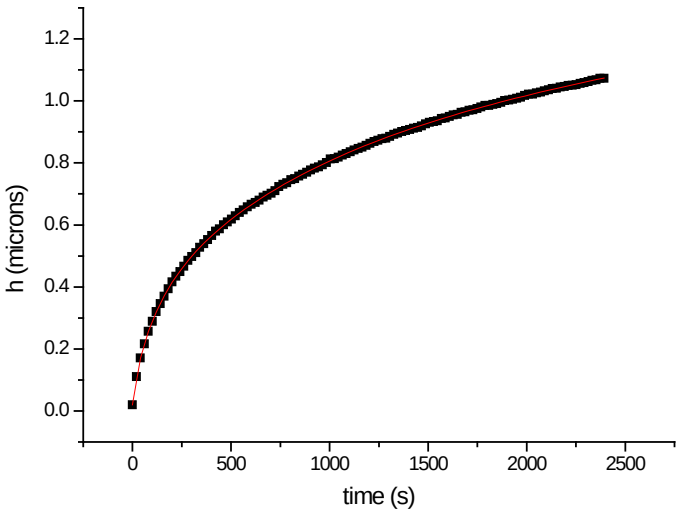

Figure 4.26: Typical plot obtained from creep experiment on a paint coating. Curve fitting using the EVEV model is shown as the superimposed line.

Table 4.15: Parameter values obtained using different number of exponents in the EVEV model, for 3 indentation tests on a polystyrene sample, using the same test conditions. The elastic displacement, h_e, obtained from the O&P method is also shown.

Indent	n	h_e O&P (μm)	h_e EVEV (μm)	h_1 (μm)	h_2 (μm)	h_3 (μm)	h_4 (μm)	h_5 (μm)	τ_1 (sec)	τ_2 (s)	τ_3 (s)	τ_4 (s)	τ_5 (s)	μ_0 (s/μm)
1	3		0.2054	0.027	0.046	0.048			42.54	309	1056			$3.1x10^7$
	4		0.2054	0.029	0.026	0.026	0.02		44.63	430	430.1	430		$1.6x10^5$
	5	0.2057	0.2054	0.029	0.018	0.018	0.02	0.018	44.63	428	429.3	431	431	$1.6x10^5$
2	3		0.2037	0.040	0.058	0.017			46.29	513	271.8			$2.1x10^5$
	4		0.2032	0.029	0.029	0.032	0.04		33.43	159	976.1	519		$1.6x10^6$
	5	0.2032	0.2033	0.030	0.03	0.024	0.02	0.014	34.58	166	650.9	620	713	$5.1x10^6$
3	3		0.2049	0.050	0.046	0.042			59.29	520	1108			$3.7x10^6$
	4		0.2053	0.050	0.032	0.022	0.02		60.1	522	714.4	721		$2.7x10^5$
	5	0.2037	0.2052	0.049	0.022	0.02	0.02	0.020	58.54	383	684.5	893	893	$4.8x10^5$

Figure 4.27 highlights an instrumental difficulty that complicates the EVEV creep analysis. The EVEV model relies on fast loading to the constant load (creep) condition. This procedure ensures that most of the viscoelastic response of the material is displayed in the creep response. Unfortunately, the UMIS 2000 instrument adjusts the load ramp speed for the final loading increment to avoid load overshoot. In Figure 4.27 point B denotes the end of the loading segment, and the corresponding displacement is h_{ep} (= h_{in} , and is the sum of the elastic, he, and the plastic displacement, h_p). This point also corresponds to the beginning of the creep segment. However, between point A and point B, significant creep occurred when a compliant coating was tested during the slow final loading. This substantial displacement was not accounted for as creep in the curve fitting, but instead it was included in the value of h_{ep}, i.e., as part of the elastic-plastic displacement. These parameters were defined earlier in Figure 2.3, under the Experimental section.

An attempt was made to correct for the slow final loading by extrapolation. By extrapolating the loading curve and creep curves, the start of the creep can be estimated as point B' as shown in Figure 4.27. The results for the paint coatings were re-analysed by extrapolating and shifting the h_{ep} value to point B', as shown in Table 4.16. Since the h_p values will no longer be the same, and hence the area correction factor will also be different, for the purpose of illustrating the effect of the correcting for point B (h_{ep}), the values without area corrections are shown in the table (hence the values differ from those given in Table 4.13). Note that this exercise was not carried out for polystyrene as the creep component during loading was small (refer to Figure 4.1 at the beginning of the Results section, where the creep displacement for polystyrene tested at a maximum load of 5mN is just over 100nm).

The results in Table 4.16 showed that the h_{ep} correction did not improve the accuracy of the EVEV model; and the modulus values were considerably higher, especially at low loads compared with the analysis taken without extrapolation (i.e. when h_{ep} was determined at Point B). This difference can be expected when the equation for the EVEV model (equation. 2.68) is examined:

$$E_0 = \frac{P_0 h_{in}}{A_0 h_e}$$

And $h_{in} = h_e + h_p$ or $h_{in} \approx h_p$ when $h_p >> h_e$; $A_0 \propto h_p^2$

Also h_e is obtained from the unloading curve and therefore unaffected by the changes in h_{ep}. Therefore, for the systems that shows different amounts of plastic indentation:

$$E \propto \frac{h_p}{h_p^2} \propto \frac{1}{h_p}$$

Thus decreasing h_{ep} would directly decrease h_p by an equal amount, leading to an increase in E values.

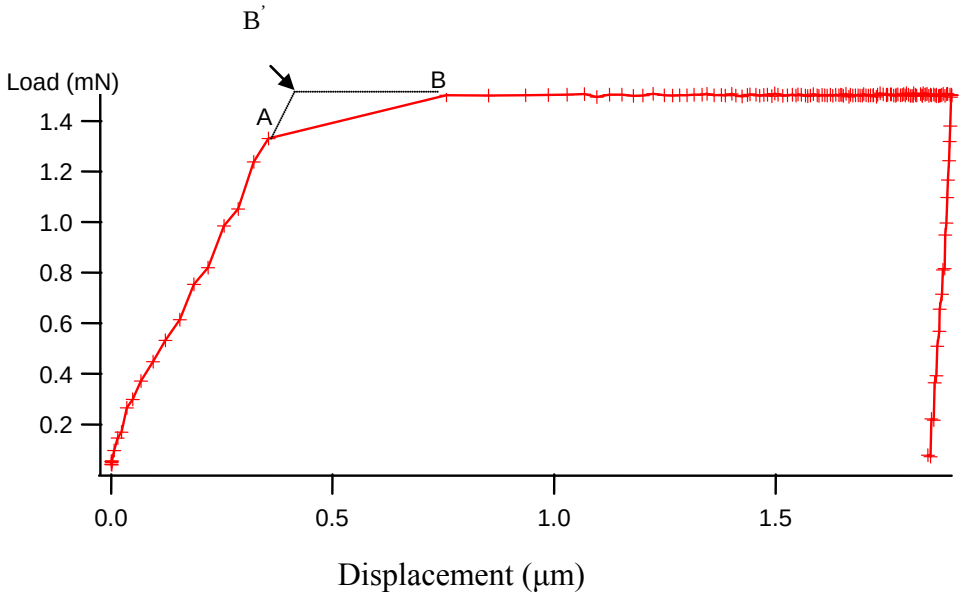

Figure 4.27: Indentation plot for a black coating, loading rate @2.5mN/s.

Table 4.16: E^* values of paint coatings obtained using different h_{ep} values with the EVEV model, without area correction.

Coatings		Maximum Load			
		5mN	2.5mN	1.5mN	1mN
White	h_{ep} = B	4.83±0.24GPa			
	h_{ep} = B'	6.53±1.09GPa			
Black	h_{ep} = B	2.81±0.24GPa	3.25±0.64GPa	3.64±0.72GPa	2.86±0.46GPa
	h_{ep} = B'	4.34±0.50GPa	5.74±1.10GPa	6.10±0.45GPa	9.18±1.60GPa
Clear	h_{ep} = B				3.58±0.56GPa
	h_{ep} = B'				9.81±1.82GPa

Another source of error could be attributed to creep during unloading, which would affect the estimation of h_e. As mentioned previously, creep would lead to a steeper unloading slope and hence a lower h_e value, and consequently a higher h_p value (as illustrated in Figure 4.28) Modulus values are directly affected by errors in estimating the plastic deformation, as discussed in the paragraph above. In this instance, the modulus value should decrease as h_p increases as a result of creep during loading. Comparison of the modulus values obtained from the compliant clear coating and the less compliant black coating were inconclusive due to large variability. A maximum load of 1mN was all that could be applied to the clear coat to avoid pronounced substrate effects using the pointed Berkovich indenter. Such low loads lead to considerable variability in the data collected.

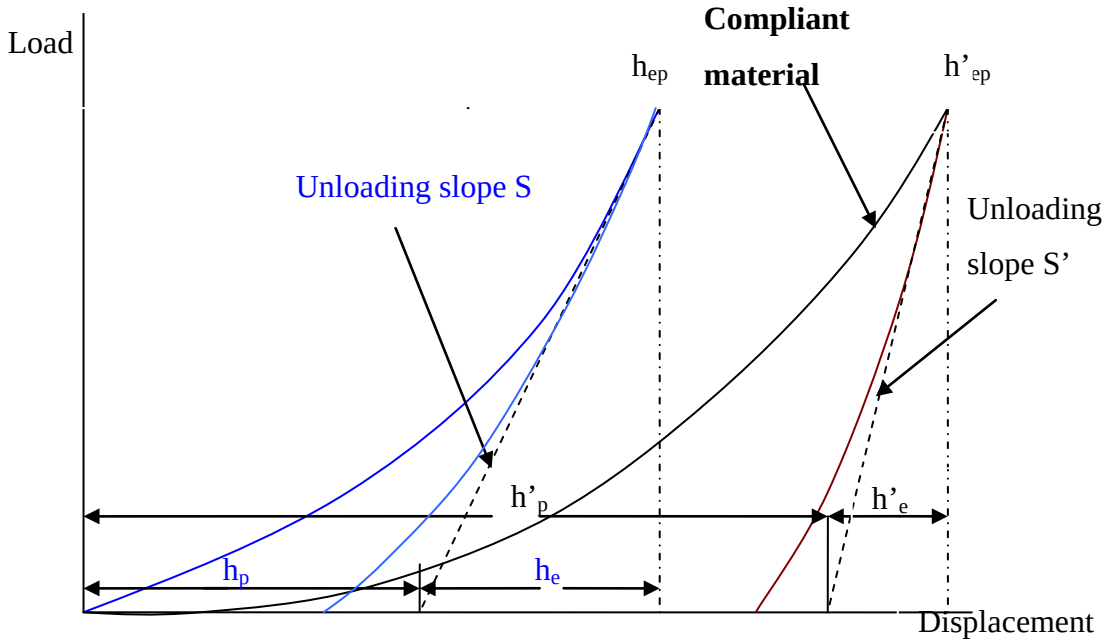

Figure 4.28: Schematic representation of the force-displacement curve for two materials with different compliance**.**

For other pigmented paint coatings it was possible to apply higher loads without penetrating too deeply. It was found that decreasing the maximum load resulted in an increase in the modulus value when the EVEV model was applied. This effect could be explained by the increase in creep due to the increase in maximum load. The increase in the time taken to reach a higher maximum load (at constant loading rate) also resulted in more creep occurring during the loading and unloading cycles. Thus, h_{ep} and h_p are overestimated; and the net effect is a lower calculated value for the modulus at higher loads. As shown in Table 4.14 for the black coating tested at a maximum load of 5mN and 2.5mN, the calculated moduli are 3.54 and 4.55GPa, respectively (after correcting for the indenter tip imperfection). The difference in

modulus is directly reflected by the large difference in creep displacement from the two maximum loads. For the higher maximum load of 5mN, the average creep displacement was 2.14μm; whereas the average creep displacement at the lower maximum load of 2.5mN was only 1.52μm. The average creep displacement for the black coating at even lower maximum loads of 1.5mN and 1mN did not differ much from that obtained at the maximum load of 2.5mN; and the modulus values were not that different once the standard deviation was taken into account. For the stiffer polystyrene, the results at the maximum load of 10mN and 5mN were similar, once the standard deviation was taken into account (Table 4.12). In the case of the O&P method, for the paint coatings, the reverse was observed (Table 4.14). In this instance, higher loads resulted in higher modulus values. This trend be attributed to surface roughness effects (also refer to section 4.1.1).

Indentation of compliant materials invariably led to excessive depth of penetration, which necessitated testing at low loads, where surface roughness effects become significant. This, in turn, led to asperity loading resulting in larger than expected stresses, and hence larger penetration depth. At the same time, the contact area could no longer be calculated using equation (2.14), as the area function would change due to deviations from ideal contact surface geometry (constant 24.5 for a perfect Berkovich tip would no longer hold true) and from larger than normal penetrations, which would result in large deviations in the estimation of h_e. This error would affect the calculation of h_p, causing error in the area correction factor.

Despite the instrumental problems the EVEV model did provide a measure of modulus that was different to that obtained by the classical Oliver & Pharr method.

For the low creep polymer (polystyrene tested at room temperature) there was no discernable difference obtained by the EVEV model compared with the O&P method (after area corrections was applied). However, tests on the high creep paint coatings showed significant differences in modulus obtained by the EVEV and the O&P method.

The higher values obtained for the more compliant paint coatings using the EVEV model as compared to the O&P method can be explained by examining the equations for E* for both methods:

For O&P method, in general,

$$E^* \propto \frac{S}{h_p}$$

Also the slope S can be approximately equated to P/h_e, where P is the maximum load. Thus

$$E^*_{O\&P} \propto \frac{P}{h_p h_e} \qquad \text{(A)}$$

For the EVEV model,

$$E^*_{EVEV} \propto \frac{P h_{ep}}{h_p^2 h_e} \qquad \text{(B)}$$

or

$$E^*_{EVEV} = E^*_{O\&P}\left(\frac{h_{ep}}{h_p}\right)$$

Comparing equations A and B, equation B has the extra term h_{ep}/h_p. Since h_{ep} is greater than h_p, this extra term h_{ep}/h_p is greater than 1. Hence the E* obtained from equation B will always be greater than that obtained from equation A. Thus the EVEV model will yield a larger E* value than the O&P method. For the more compliant material, the discrepancy might be larger since the determination of h_{ep}

becomes more inaccurate as the creep component cannot be easily determined; and slow loading rates cannot totally counter the effect of creep.

It is also worth mentioning that since ultra-indentation methods cannot selectively probe between pigment particles to directly test the modulus of the paint matrix, the results are dependent on pigment distributions at the point of indentation for each test, hence contributing to the observed scatter in the modulus results.

4.3.2.2 The Fischer-Cripps model

Fischer-Cripps [83] also attempted to model the creep behaviour of polymeric and metallic materials under indentation loading using variations of both the Maxwell and the Voigt models. Equations for both the conical indenter and the spherical indenters were developed. The study showed that the models provided good fit for the creep responses of materials tested. Furthermore, due to the initial plastic deformation, which occurred with the sharp conical indenter, the initial response in displacement was found to be substantially larger than the predicted values, and the calculated modulus could be significantly smaller than the true value. Hence, the author found the model to work better for the spherical indenter, where plastic deformation is less severe. Fischer-Cripps applied the model to two acrylic co-polymer films (of 100-150μm thickness). The author claimed to have obtained acceptable results, although these results were not compared to any known standards or values.

The current work was restricted to the use of a spherical indenter. The results generated were compared to those obtained using the standard Oliver & Pharr analysis method on the unloading slope, as well as from tensile tests of bulk materials. Note that the E^* in this model referred to the combination of the elastic

modulus and the Poisson's ratio of the specimen material ($E^* = E / (1-\nu^2)$), and not the combined modulus of the material and the indenter. However, since a diamond indenter was used which is much stiffer than the polymer samples tested, E^* in this instance would be approximately equivalent to the combined modulus value. Hence the E^* obtained using the model could be directly compared to previous values obtained using the Oliver & Pharr method. Similar to the EVEV model, the value E_1 in the mechanical model in the Fischer-Cripps (F-C) theory would represent the elastic modulus of the first spring element. This instantaneous spring response can be interpreted as the E^* value of the material. An example fit of the F-C model to creep data generated for the polystyrene reference sample is shown in Figure 4.29.

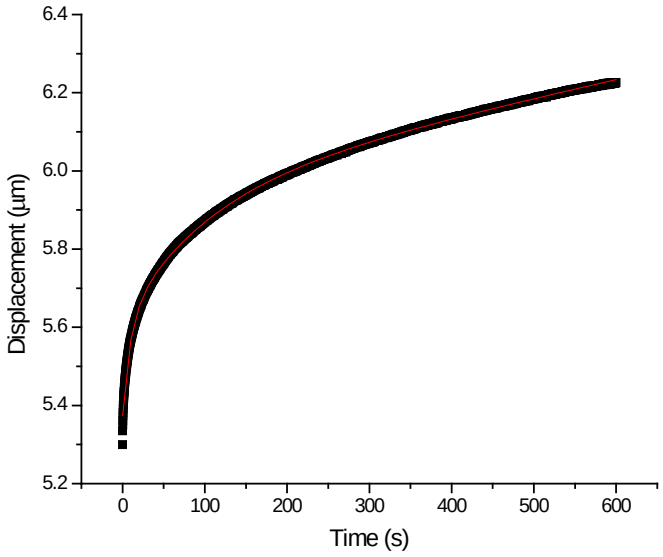

Figure 4.29: Creep data for polystyrene tested using the DMA at 40°C. Curve fitting line is superimposed.

Values of E^* generated from the mechanical model for the high temperature DMA testing of polystyrene are compared with those generated using the classical Oliver and Pharr method (refer to Table 4.11) and are shown in Table 4.17. The F-C modulus values were observed to be slightly lower, but very close to those obtained for the O&P method when the results without contact area corrections were compared. Strictly speaking, direct contact area corrections cannot be employed for the F-C model since the equation makes use of the indenter radius rather than the actual contact area. However, once the contact area has been corrected, this can be used to find a new value for indenter radius. This radius would represent an equivalent indenter of ideal shape that would yield the corrected projected contact area. Since the same DMA indenter was used to generate data for both the O&P and the F-C analysis, area correction (for O&P results) and the radius correction (for the results using the F-C model) were carried out to compare the two sets of results (Table 4.17). Note that the estimation of T_g itself is similar for both methods (with or without area correction), with the onset of the transition indicated by a decrease in E* and this decrease was noted at 100^{o}C when the data was analysed using both models

Table 4.17: E* values generated for polystyrene by the Fischer-Cripps model compared with those from the Oliver & Pharr method.

Temperature(^{0}C)	E*(GPa) – F-C model	E*(GPa) – O&P	E*(GPa) – F-C Contact area corrected	E*(GPa) – O&P Contact area corrected
40	1.89	2.03± 0.08	4.09	4.39 ± 0.17
60	1.78 ± 0.17	1.86 ± 0.19	3.84 ± 0.37	4.01 ± 0.40
80	1.77 ± 0.11	1.94 ± 0.08	3.82 ± 0.24	4.19 ± 0.17
100	0.90 ± 0.18	1.60 ± 0.16	1.95 ± 0.39	3.46 ± 0.35
105	1.17 ± 0.09	1.86 ± 0.23	0.22 ± 0.02	0.35 ± 0.05
110	0.22 ± 0.08	1.40 ± 0.52	0.03 ± 0.01	0.22 ± 0.03
115	0.02 ± 0.00	0.47 ± 0.23	0.005 ± 0.00	0.12 ± 0.04

Similar to the EVEV model, the Fischer-Cripps model provided fairly good curve-fitting to the creep curves, except for the initial portion, as shown in Figure 4.29. The poor fit of the initial portion of the curve resulted in a higher starting displacement value, h (at t=0). Thus the first term of the equation for the model,

$$h^{3/2}(t) = \frac{3}{4}\frac{P_0}{\sqrt{R}}\left[\frac{1}{E_1^*} + \frac{1}{E_2^*}\left(1 - e^{-tE_2^*/\eta_2}\right) + \frac{1}{\eta_1}t\right],$$

would be overestimated, and the E^* value obtained would be too low.

In addition, the limitation on the data capturing speed of the DMA equipment (~7 data points/s) led to further error as there was a substantial time delay in the capturing of the first creep displacement point. That delay would lead to further discrepancies in the h_1 value, and thus the elastic modulus estimation was under estimated even further using the F-C method. To illustrate the magnitude of the error, in the case of the test carried out at 40^oC, the error contribution with respect to the determination of h from the curve fitting would amount to roughly 1.5%; and from the time delay in data capturing would contribute to an error of only 1.2%. Even with the exponent of 3/2, the error in E^* should only amount to less than 7%. From Table 4.17, it would appear that the error contribution is largely from the imperfect indenter shape, since the results of the F-C method compares well to those of the O&P method, before area correction. In fact the F-C method appears more accurate at temperature close to and, particularly, above the T_g.

With the slower data capture, the nose effect which would normally be observed in polystyrene above T_g, due to extensive creep, was not noticeable, since the data for the 'nose' region was not captured. Thus the O&P method could be used, but with increased error at higher temperatures, since creep would still cause the unloading slope to appear steeper. As a result the O&P method gave larger than expected E* values above T_g when creep effects are most prominent. The F-C method, however, gave more acceptable estimates of the modulus above T_g, with the lowest modulus of 5 MPa determined at 115^{o}C.

Average values for all the parameters obtained for the model at the various temperatures are shown in Table 4.18. From Table 4.18, it can be observed that not only did E_1 (elastic modulus) decrease with increasing temperature, but all other parameters followed the same trend too (Figure 4.30 & Figure 4.31). The log values of the parameters decrease sharply at around T_g , at 100 to 105°C. Relaxation times were calculated and included in Table 4.18. All three relaxation times showed a peak value at or near T_g (105^{o}C). A major advantage of the F-C model compared with simpler O&P method is the availability of viscosity and viscoelastic parameters that may be used to more fully analyse the polymer mechanical behaviour.

Table 4.18: Values of parameters for polystyrene obtained using the Fischer-Cripps model at various temperatures.

Temperature (^{0}C)	E_1^* (GPa)	E_2^* (GPa)	η_1 (GPa s)	η_2 (GPa s)	τ_1 (s)	τ_2 (s)
40	1.89	52	7.0×10^6	2650	3.7×10^6	32
60	1.78	33	1.7×10^4	2514	6.2×10^3	76
80	1.77	14	1.4×10^4	521	7.9×10^3	42
100	0.90	0.25	120	218	1.3×10^2	872
105	1.17	0.025	4.8	31	4.1	1240
110	0.22	0.0042	3.3	1.1	1.5×10^2	262
115	0.02	0.0023	2.0	0.078	1.0×10^2	34

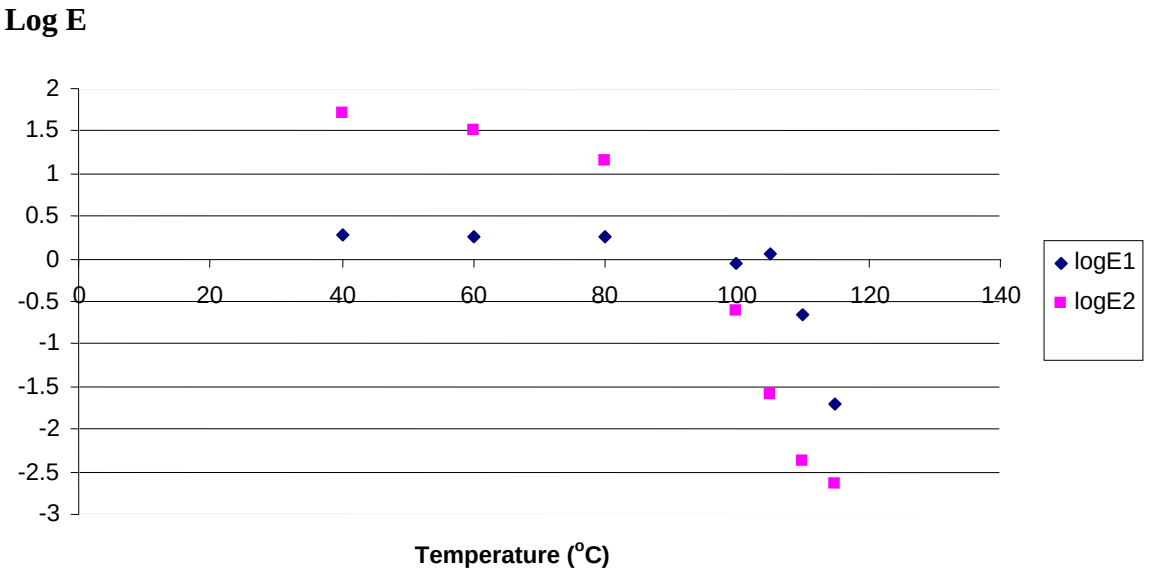

Figure 4.30: Log (E_1^*, E_2^*, E_3^*) at various temperatures, obtained using the F-C model.

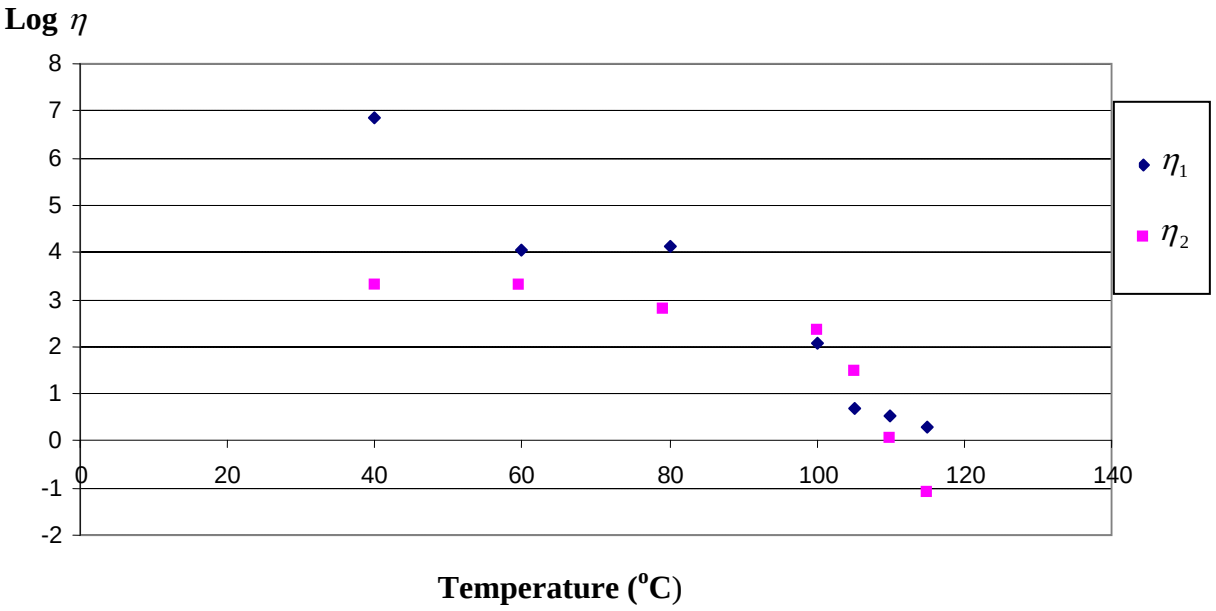

Figure 4.31: Viscosity parameters plotted as log values against temperature.

Tensile creep tests on bulk polystyrene were carried out at various temperatures using the DMA, using the same loading/unloading rates and the same holding time at temperature, and the results were analysed using the F-C model (modified for simple tension) for comparison. The results are shown in Table 4.19. The tensile modulus values obtained directly from the loading slope, and the E_1^* values obtained from the F-C model applied on the tensile creep data were, in general, low compared to known results for polystyrene.

The discrepancy could be due to slipping of the samples in the grips. This problem was common near room temperatures and was exacerbated by the smooth surface of the samples cut from the moulded polystyrene. At higher temperatures the gripping was improved as plastic deformation at the grips would prevent the samples slipping.

However, excessive plastic deformation also made the determination of the linear loading slope more difficult, and thus error was introduced at high temperatures too.

Table 4.19: Modulus values obtained from tensile tests, as well as average parameters obtained from tensile creep tests, using the F-C model, at various temperatures.

Temperature (°C)	Tensile Modulus (GPa)	E_1 (GPa)	E_2 (GPa)	η_1 (GPa s)	η_2 (GPa s)	τ_1 (s)	τ_2 (s)
40	2.1	1.8	4.2	$1.7x10^4$	$3.5x10^3$	$9.4x10^3$	833
60	2.1	1.5	2.0	$5.5x10^3$	$1.6x10^3$	$3.7x10^3$	800
80	1.2	1.0	1.1	$3.1x10^3$	$0.9x10^3$	$3.1x10^3$	818
100	0.5	0.6	0.7	60	506	100	723

The tensile modulus results obtained using the F-C method were in general lower at the lower temperatures than the tensile modulus, obtained using the standard method of estimating the slope of the stress-strain curve. The results, however, are fairly similar at the higher temperatures. These results are shown in Table 4.19. Both sets of results are lower than expected for polystyrene at temperatures below the T_g and the possible reason was discussed in the previous paragraph.

The same trend was observed for both indentation and tensile tests (refer to Table 4.18 and Table 4.19), with the parameters showing decrease at 100°C, close to T_g (Figure 4.32).

UMIS creep experiments were also conducted at room temperature using spherical indentation on bulk polystyrene reference sample and a clear coating and these data were analysed with the F-C model. The results for polystyrene were compared to that

obtained using the O&P method, shown in Table 4.20 (also shown in Table 4.7). The E* results from the F-C method appeared to be less sensitive to maximum load than the O&P method and the variability of results was generally smaller with the F-C method. As with the O&P results, the F-C results at lower maximum load (20 mN) were still lower than higher maximum loads, probably due to surface roughness effects. In addition, the results from F-C method compared well to other methods and to values quoted in the literature for polystyrene. The standard deviations were small, indicative that the results were reproducible under the same testing conditions.

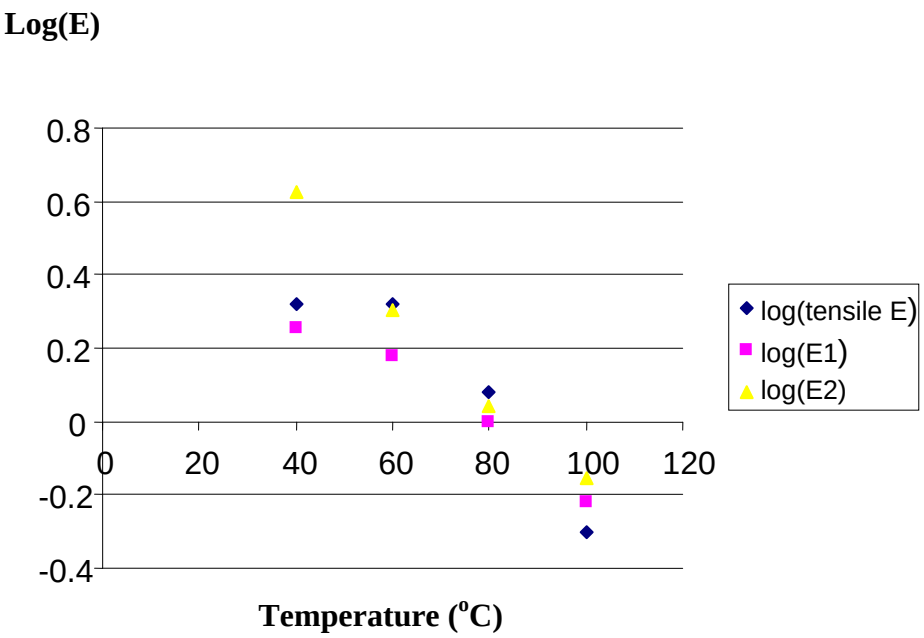

Figure 4.32: Modulus values obtained from tensile test and from F-C model, plotted as log values against temperature.

It should be noted that the results for the F-C model shown in Table 4.20 are higher than the results shown in Table 4.18. Those in Table 4.20 were carried out at ambient conditions, and therefore its behaviour would be less compliant than at higher

temperatures. Also, different indenters were used to generate the two sets of results. The DMA (Table 4.18) used a steel indenter and as was mentioned earlier, this indenter had a flat spot and was thus not of the ideal spherical shape. The diamond indenter used in the UMIS test (Table 4.20), on the other hand, was more ideal in shape.

Table 4.20: Comparison of E* values for polystyrene using O&P and F-C method.

Max. Load (mN)	E* from F-C method (GPa)	E* from O&P (GPa)
20	2.7 ± 0.05	2.65 ± 0.08
100	2.7 ± 0.05	3.27 ± 0.54
250	3.1 ± 0.06	3.50 ± 0.05

The most significant contribution of the F-C model was observed in the analysis of the highly viscoelastic clear coating tested at ambient temperature using the UMIS. Two clear coatings made using the standard 36 drawbar and a thicker coating made from a 48 drawbar was tested. The results are shown in Table 4.21. These results show that the F-C model worked better than the O&P method for materials that creep at ambient temperatures. The O&P method over-estimated the modulus due to the contribution of creep making the unloading curve steeper than would be expected from purely elastic recovery. In some cases, the “nose” on the unloading curve gave a negative slope meaning that the calculated modulus was infinite. In contrast, more realistic E* results were obtained using the F-C model in the case where the unloading slope formed a ‘nose’ due to excessive creep. The E* values obtained from multiple tests on the same sample and on tests on the two different coating thicknesses gave very reproducible results when the F-C method was used.

Table 4.21: Comparison of E* results from F-C model and O&P method for clear paint coatings.

Coating thickness	E* from F-C (GPa)	E* from O&P (GPa)
Standard	0.49 ± 0.01	2.41 ± 0.05
Thick	0.45 ± 0.02	1.2 to ∞ (due to 'nose')

4.3.3 Analytical methods to correct for viscoelasticity

4.3.3.1 The Feng and Ngan method

In section 2.6.2 the method used by Feng and Ngan to correct for the creep effect during unloading was described and the derivation of the final equation was given as:

$$\left.\frac{dh_e}{dP}\right|_u = \left.\frac{dh}{dP}\right|_u - \left.\frac{dh_v}{dP}\right|_u \qquad (2.74)$$

where $dh_e/dP|_u$ is simply the reciprocal of the elastic recovery stiffness S, $dh/dP|_u$ is the reciprocal of the observed initial unloading contact stiffness S_u, and $dh_v/dP|_u$ is the correction term due to time dependent effects. It was further shown that

$$\left.\frac{dh_v}{dP}\right|_u = \frac{\dot{h}_v|_{hold}}{\dot{P}} = \frac{\dot{h}|_{hold}}{|\dot{P}|} \qquad (2.75)$$

where $\dot{h}|_{hold}$ is the creep rate at the end of the holding period, $\dot{P}$ and $|\dot{P}|$ are the unloading rate and the absolute value of the unloading rate, respectively.

$$\frac{1}{S} = \frac{1}{S_u} + \frac{\dot{h}|_{hold}}{|\dot{P}|} \qquad (2.76)$$

Using the method of Feng and Ngan, in accordance with equation (2.76), the unloading contact stiffness was corrected using the measured creep displacement at the end of the holding period. The ratio S/S_u will give a direct indication of the reduction in E^* due to creep, since E^* is directly proportional to S. Table 4.22 shows the extent of this correction with temperature, and the revised value for E^* for polystyrene tested using the DMA indentation method.

Table 4.22**:** Showing revised E* on the DMA results for polystyrene indented with a spherical indenter.

Temperature (^oC)	S_u (mm/N)	S (mm/N)	S/S_u	E* (GPa)	E* revised
40	250.8 ± 8.7	250.8 ± 8.7	1.00	4.26	4.26
60	256.8 ± 2.3	256.8 ± 2.3	1.00	4.01	4.01
80	280.0 ± 7.0	280.0 ± 7.0	1.00	4.19	4.19
100	312.7 ± 1.0	305.0 ± 0.8	0.98	3.46	3.39
105	342.5 ± 61.8	277.4 ± 50.1	0.81	0.35	0.28
110	247.5 ± 37.4	225.2 ± 34.0	0.91	0.22	0.20
115	150.0 ± 51.1	144.0 ± 49.1	0.96	0.12	0.12

The value of the observed stiffness, S_u, increased with temperature until near the T_g when the sample begins to soften and there was an associated decrease in the observed stiffness. The actual stiffness of the material, on the other hand, should decrease steadily with increasing temperature, followed by a drastic drop at the T_g. The corrected stiffness, S, however, did not reflect this expected trend below T_g, although the extent of the correction had increased with temperature up to T_g. It is therefore evident that the extent of the correction offered by the method was insufficient to totally account for the effect of creep. Also, the extent of correction was small at temperatures above the T_g, which might indicate the invalidity of the method when the material behaviour changed to that of a viscous liquid.

Similar analysis was carried out on polystyrene and a black paint coating tested with the Berkovich indenter using the UMIS system. The results showed insignificant E^* changes in both samples at room temperature, as the ratio S/S_u were greater than 0.99 in all the test data evaluated.

4.3.3.2 Superposition Principle

The principle was applied to the experimental data generated using the DMA for testing of polystyrene, at temperatures close to the T_g, where creep is prominent, even after applying a long holding period at maximum load. The equations for the individual creep curves obtained by curve fitting (Fischer-Cripps model) were applied and the creep displacement during the unloading event was then subtracting off the measured unloading curve, as shown schematically in Figure 3.17 and Figure 3.18. The revised stiffness, S_r, as well as revised composite modulus E_r^* were tabulated in Table 4.23.

Table 4.23: Showing values for S and E^* corrected using the superposition principle.

Temperature	S (mm/N)	S_r (mm/N)	S_r/S	E^* (GPa)	E_r^* (GPa)
115^{o}C	157.9 ± 60.5	150 ± 51.05	0.96 ± 0.04	0.12 ± 0.04	0.12 ± 0.04
110^{o}C	308.2 ± 87.6	247.5 ± 37.4	0.83 ± 0.13	0.22 ± 0.03	0.17 ± 0.03
105^{o}C	498.3 ± 1.3	342.5 ± 61.8	0.69 ± 0.12	0.35 ± 0.05	0.24 ± 0.07
80^{o}C	254.4	227.5	0.89	3.35	2.98

The superposition method was applied to indentation data for polystyrene tested over the temperature range 80^{o}C – 110^{o}C, with the results given in Table 4.23. The data show a significant decrease in modulus values with the creep-corrected modulus E_r^* significantly smaller than the uncorrected modulus E^* at temperatures below 115^{o}C. Since it is known that continued creep during the unloading process increases the unloading slope and gives a larger than expected modulus, the results given in Table 4.23 suggest that the superposition method can be useful in correcting for creep effects near T_g. It should be noted that the long hold period used in these tests before unloading also reduced the creep effects. Without a hold period a “nose” or negative

slope appears in the unloading curve. The appearance of a “nose” is an obvious indication of creep; however, the nose is usually eliminated by an extended hold period before unloading. A positive unloading slope is then obtained, but the effects of creep can still be significant although not obvious from the shape of the curve.

At temperatures above the T_g, viz., 115^{o}C, the superposition method did not have any impact on the unloading slope, or the modulus value, since the corrected values were similar to the original values. This is due to the more rubbery nature of polymeric materials above T_g with less viscoelasticity.

The applicability of this method for polystyrene at a lower temperature of 80°C, where creep is less prominent, was also evaluated. The creep behaviour with time was established by conducting an indentation creep experiment using the DMA; and by curve fitting using the F-C model. Another indentation test was then conducted using the same sample and in a different location, but without any holding time. The creep component in the unloading displacement was then subtracted from the measured data, since the creep displacement with time could be estimated using the F-C model. The result is also tabulated in Table 4.23. Again, the creep-corrected modulus was lower than the uncorrected value which illustrates that the creep is influencing the measured modulus even at temperatures as low as 80^{o}C.

5 DISCUSSIONS

Paint coatings are a vitally important protection system for many engineering structures and the mechanical properties of paint need to be tuned to meet the application requirements. Baked on “enamel” type paints are typically hard and scratch resistant and are used for cars and other painted metal structures. These paints form crosslinked three-dimensional polymer matrices that bind together various pigment and filler particles. The relationship between crosslink density in the polymer matrix and mechanical properties is well-known [1], but the determination of the paint mechanical properties is not trivial. Simple tests like scratch resistance can be correlated to the degree of paint cure (i.e. crosslinking). However, such correlation has been difficult to establish in pigmented paint coatings as dislodgement of pigments during scratch tests sometimes led to accelerated wear. Recent developments in micro-indentation methods have provided means by which thin layers can be mechanically analysed. Indentation testing would yield information on paint properties, without causing the dislodgement of pigments. Each indentation test typically takes a few minutes, making it an ideal candidate as a rapid quality control tool.

The aim of this work was to investigate the suitability of indentation methods for determining the mechanical properties of paint systems containing hard filler particles. Further, it was desirable to determine these mechanical properties over a range of temperatures, since the “thermo-mechanical” behaviour of polymers is

particularly informative. The major drawback in using indentation techniques on soft, compliant materials such as polymers are the time-dependent response (creep at fixed load or stress relaxation on fixed displacement), leading to ambiguity in the interpretation of load-displacement traces from which the mechanical properties are calculated. Mechanical models using springs and dashpots to estimate elastic modulus values from the creep response were investigated, as were analytical methods to nullify the effect of creep in the unloading response.

Both micro- and nano-scale indentation methods were used. Experimental work on micro-indentation testing was carried out on a commercially available system, the UMIS-2000, using a pointed Berkovich as well as spherical indenters. Polystyrene was used as reference sample, to examine the repeatability of the technique, as well as to examine the effect of surface roughness. The latter is important, as the surfaces of the industrial paint coatings being examined would be inherently rough, in the micron scale. The feasibility of using a commercial atomic force microscope (AFM) and a home-built 'force-rig' for the nano-indentation work was also examined. High-temperature indentation work was carried out on bulk polystyrene using a commercial dynamic mechanical analyzer (DMA), to examine the applicability of the indentation technique at temperatures close to the glass transition temperature (T_g). These results were compared to other known methods such as three-point bend testing and tensile testing. Various mechanical (creep) and analytical models were examined for their merit in estimating the elastic modulus of paint coatings; and also in nullifying the effect of viscoelasticity, such that elastic contact equations (such as those used in the Oliver and Pharr and Field and Swain method), would still be valid in yielding elastic modulus values.

5. 1 Ultra-microindentation

Using the commercially available UMIS 2000 micro-indentation system, with the attached software which makes use of the Oliver and Pharr analysis of the unloading slope, the elastic modulus results obtained on the model polystyrene material at ambient conditions were accurate and repeatable, yielding a reduced modulus, E*, of 4.3GPa with immeasurably small standard deviation (refer to section 4.1.1 and Figure 4.1). However, surface finish was found to play an important role in the accuracy of the results. Analysis showed that the error did not lie in the determination of the unloading slope, but rather, in the determination of the initial displacement. Table 4.1 showed that the E* values for 5 indentation tests ranged from 1.48 to 4.56, but the unloading slope values were fairly similar, between 28.08 and 35.39. In fact, asperity loading was found to be the major contributor to this error. Using spherical indentation and the Field and Swain method, it was shown that once these asperities have been sufficiently flattened such that full contact between the indenter and the sample surface occurred, correct modulus values could be obtained (Figure 4.5). A consequence of this finding is that a sufficiently large load and/or plastic preloading can reduce the error arising from surface roughness issues.

Due to the inherent roughness (micron scale) of the pigmented paint coatings, micro-indentation methods might not be suitable as application of large loads to flatten the asperities might introduce substrate effects. In Tables 4.7 and 4.8, E* values obtained using 100μm radius indenter, for polystyrene and a clear coating, were shown and the E* values for the clear coat were lower than for polystyrene, as expected. The total penetration attained for the maximum loading of 3mN, with 10 minutes holding time, for the clear coat was around 1.2μm. This penetration depth is acceptable to

limit substrate effects (less than a tenth of the coating thickness). For the most compliant pigmented paint coat (viz., black coat), a 5mN maximum load gave a penetration depth of just under 2μm. This penetration was just over 1/10 of the coating thickness, and hence substrate effects might be an issue. Despite these limitations, the method was useful in qualitatively differentiating differences in the degree of curing as well as in different pigment contents in various paints. Another limitation of the UMIS when the Berkovich indenter was used was the excessive depth of penetration on the more compliant paint coatings. For example, the total penetration of the brown coating was between 1.8 and 1.9μm, using a maximum load of 5mN and a holding time of 10 minutes. The E* results obtained appeared high – around 5.8GPa for the brown coating, and 6.6 GPa for the white coating. The high results might be a consequence of substrate effects, or the pigments and flattening agents might act as 'stiffeners' for the materials. These particles might also act as micron size platelets or pistons beneath the sharp indenter, thus redistributing the load and stress directly beneath the indenter. However, a more reasonable suggestion for the high values might be that creep effects could not be fully nullified, even with a ten minute holding time, so that the unloading slope values were high, resulting in high E* values. The creep effect would explain the reason for the lower E* values generally observed when a spherical indenter was used, since a sharp indenter would induce higher stress and more creep effects.

In summary, indentation testing using commercially available ultra-micro indentation systems at ambient temperature could yield accurate and repeatable modulus values for less compliant polymers such as polystyrene, provided that asperity loading due to surface roughness was not present. This commercial instrument used the Oliver &

Pharr as well as the Field and Swain methods for determining the elastic modulus from the unloading curve and this method has been developed for elastic-plastic materials. For paint coatings, two issues were apparent: first, the inherent surface roughness (in micron scale) and second, the low T_g close to ambient temperature, causing creep. Despite these problems, the UMIS method was sufficiently sensitive to yield modulus values that reflected differences in degrees of cure and the volume of pigment within the paint. It can thus be proposed that using spherical indentation at the same loading conditions (5mN @2.5mN/s) instead of a sharp indenter, in a low temperature controlled environment (for example 20^oC below the T_g), and using suitable holding times to reduce the creep effects, quantitative modulus results could be obtained. By controlling and lowering the testing temperature, the large standard deviations observed when the Berkovich indenter was used (of over 20% of the modulus values) for paint coatings should be significantly reduced. Standard deviations could be further reduced through examination of individual force-indentation depth to identify the presence of asperity loading. Should poor contact due to asperity loading be identified, the results should be discarded or rectified by subtracting the displacement due to asperity loading, prior to analysis using the Oliver and Pharr method.

5. 2 Nano-indentation

Nano-indentations of polymeric materials on commercially available AFM equipments were unsuccessful due to software limitations with no allowance for a holding time to counter creep effects. Even with the in-house-built ‘force-rig’ equipment which allowed for a holding time, the nature in which the force data was

generated was not suitable for materials which would undergo creep. This problem occurred as the indenter attached to the cantilever sinks into the material due to creep, the deflection recorded via the position of the laser spot would change accordingly. Thus, nano-indentation using AFM type equipment which relies on cantilever deflection to determine the applied force would always have the problem of decreasing deflection signal as the probe sinks into the material due to creep, thus causing the initial portion of the unloading data to be missing. A possible way to overcome this might be to reduce the load such that no permanent indentations are made, as per the work of Chizhik et al. [63]. In their work on rubber and polystyrene, only the loading event was analysed, using appropriate elastic equations. However, with compliant material such as polyester paint, having T_g close to ambient, low stress states might be difficult to attain with sharp cantilever tips. Increasing the tip diameter, such as by attaching particles to the end, might defeat the object of being able to isolate and probe the paint matrix properties in between pigment/filler particles.

5. 3 High temperature indentation

High temperature indentation using a commercially available DMA instrument was carried out to examine the applicability of indentation testing for determining T_g, as well as elastic modulus near T_g. Since the DMA instrument could not operate at low loads the high temperature tests were not applied to the paint coatings and were only evaluated on bulk polystyrene. The results showed that the method was successful in obtaining T_g in the reference bulk polystyrene material which was comparable to the T_g obtained using a conventional three-point bend test on the same equipment. In

addition, the E* values obtained using indentation testing was similar to those obtained using three-point bend test, with the expected large decrease occurring through the glass transition. At temperatures close to the T_g, the modulus values appeared slightly higher for the indentation tests, possibly due to increased creep effects.

Other limitations associated with indentation testing using the commercial DMA instrument were:

- Slow data capturing speed which placed a bottom limit to the lowest maximum load that could be applied (at the loading rate of 18N/min). Low applied loads would result in insufficient data points in the unloading data which would in turn cause huge error in the determination of the unloading slope, while too high a maximum load would increase the creep component in the unloading data.
- Where excessive creep is expected, even after a holding period before unloading, such is generally the case for polymers tested near the T_g, additional correction by means of using the Superposition Principle, is proposed to subtract the expected creep displacement in the unloading slope, so as to yield more accurate elastic modulus values, using the Oliver and Pharr method.

As indenters are seldom perfect, especially at the tips, area corrections as described in section 4.3.1.1 was carried out. At high temperatures where the contact area was visible on the sample after indentation, direct measurement of the contact patch could be used to more accurately determine the modulus values.

5. 4 Viscoelastic models and analytical methods for creep correction

A main aim of this thesis was to evaluate methods to obtain elastic modulus values from visco-elastic polymers. One method that was found suitable for polymers that displayed relatively small creep rates was to hold the load at the maximum level so that the creep reduces to a small percentage of the overall deformation. It was shown that unloading after such a hold could be evaluated with the Oliver and Pharr elastic-plastic model to yield acceptable elastic modulus values. The “hold” method was not suitable, however, for polymers tested close to their T_g or above since creep rates were excessively high. In such cases, alternative analytical models were used to extract the elastic and viscous components from the deformation data. The analysis methods used were the EVEV method, the F-C method, the Feng and Nan method and the Boltzmann superposition principle.

The EVEV model gave similar modulus values compared to the classical O&P method on bulk polystyrene tested at room temperature. However, on the more compliant paint coatings, the modulus values obtained were much higher, and were much more inaccurate. This inaccuracy was shown in section 4.3.2.1 to be due to the extra h_{ep}/h_p term in the EVEV equation, as compared to the O&P equation. As creep became more significant, such as the case for the paint coatings tested at higher loads and close to T_g, the determination of the term h_{ep} became more inaccurate. Also the ratio h_{ep}/h_p became larger and greater than unity. Hence E^*_{EVEV} for the compliant materials was always greater than $E^*_{O\&P}$, and also less accurate.

The F-C method, when applied to DMA indentation on bulk polystyrene tested at room temperature, compared well to the classical O&P method. The former gave

slightly lower results than the O&P method at temperature closer to T_g, and closer to the modulus results obtained from three-point bend test. Also, the F-C method was not affected as much by the maximum load applied. This method is not reliant on the overall indentation depth, and thus not affected by asperities loading. However, higher loads would increase the time to reach maximum load, thus the load application would deviate more from the ideal instantaneous loading condition required for the creep model. Also, for the clear paint coating indented at room temperature, the modulus values obtained using the F-C method was more believable than those obtained when the O&P method was employed. This is due to the steep or negative unloading slope that results due to excessive creep, which invalidates the O&P method.

An added bonus of the viscoelastic models is the determination of parameters relating to viscosity which describe the time-dependent property of the material. High viscosity coefficients values implies small viscous flow, and can be linked to cross-linked density, while retardation times, τ, could be related to molecular movements and structures, as in the case for tensile creep. Small τ_1 compared to τ_2 (and τ_3, etc), would suggest movement of main-chain and side groups, while large τ_2 values might suggest movement of large molecular structures.

Tensile creep test, using the DMA, at various temperatures, analysed using the F-C method, were in general only slightly lower than the modulus values obtained directly from the tensile loading slope. However, the modulus values from the tensile data were low compared to known results for polystyrene. The discrepancy could be due to slipping of the samples in the grips and the relatively fast testing speed.

The Feng and Ngan method did not provide significant creep correction to the apparent contact compliance for polystyrene as well as black paint coated samples. However, the application of the Boltzmann Superposition Principle was successful in providing significant correction for bulk polystyrene over a range of temperatures from 80^{o}C up to $T_{g.}$

6 CONCLUSIONS

Indentation testing using commercially available ultra-micro indentation systems could yield accurate and repeatable modulus values for polystyrene at temperatures well below T_g, provided that asperity loading due to surface roughness was not present. The results obtained for temperatures close to T_g were slightly high, compared to three-point bend test results. For paint coatings, two issues were apparent: first, the inherent surface roughness (in micron scale) and second, the low T_g close to ambient temperature, causing creep. However, the method was sufficiently sensitive to yield modulus values which reflected differences in degrees of cure and pigment contents. From the results for the reference polystyrene, it is reasonable to conclude that the method could provide reliable modulus values for paint coatings, provided that creep effects could be eliminated. Thus for this method to become a rapid quality control test method for pigmented paint coatings, it is proposed that spherical indentation at low loads with fast loading rate (5mN @ 2.5mN/s) and a low temperature controlled environment (for example 20^{o}C below T_g) be used, with suitable holding times. It is expected that the asperities would be readily flattened into the paint matrix, and furthermore, standard deviations could be significantly reduced by discarding or rectifying load-indentation depth plots showing asperity loading.

The creep data obtained from the indentation tests (at max hold) could provide another means of obtaining elastic modulus, provided the time to maximum load is sufficiently fast to simulate instantaneous step loading to validate the use of

viscoelastic mechanical models. In addition, mechanical creep models could provide information regarding time-dependent material properties, such as viscosity coefficient and retardation times. The Fischer-Cripps model provided reliable results for the polymeric materials tested, and yielded acceptable results for the black paint coating, whereas the EVEV model and the O&P analysis could not yield reasonable results for this material, because of excessive creep effects in the unloading event. Displacements due to creep effects in the unloading event could be corrected using the Boltzmann superposition principle.

It is expected that the ideal instrument suitable for thermo-mechanical testing of paint coatings should have the basic requirements of load and displacement control, as well as analytical functions to correct for the system compliance and initial penetration [42, 43]. To reduce creep effects of paint coatings during indentation, the instrument should provide:

- Fast loading and unloading rates (user defined).
- Temperature control or be housed in a temperature controlled environment, down to 20^{o}C below the T_g of the sample.
- Holding time at loads defined by the user.

In addition, it should provide:

- Analytical software to compare a set of test and flagged abnormalities in order that data due to excessive surface roughness (asperities loading) can be discarded.
- Analytical routine based on the Oliver & Pharr and Field and Swain methods.
- Option to perform creep or relaxation experiments.

- User input material properties for the indenter or material data library for the indenter such that the sample modulus could be calculated from the reduced modulus.
- Calibration procedure using sample of known properties such that an area function lookup or calibration table could be generated and the contact area corrected [42, 43].

Testing should be carried out using spherical indenter to reduce stress and thus creep in the sample.

REFERENCES

1. J. Lange, A. Luisier, E. Schedin, G. Ekstrand, A. Hult, Development of Scratch Tests for Pre-Painted Metal Sheet and the Influence of Paint Properties on the Scratch Resistance, J. Materials Processing Tech. 86 (1999), 300.

2. D.M Shinozaki, Y. Lu, Micro-Indentation Relaxation Measurements in Polymer Thin Films, J. Electronic Materials 26 (7) (1997) 852.

3. L.I. Majoros, B. Dekeyser, N. Haucourt, P. Castelein, J. Paul, J.M. Kranenburg, E. Rettler, R. Hoogenboom, U. S. Schubert, Preparation of Polyurethane Elastomers (PUEs) in a High-Throughput Workflow, J. Polymer Sci. Part A: Polymer Chemistry 49 (2011), 301.

4. Fundamentals of Nanoindentation and Nanotribology, edited by N.R. Moody, W.W. Gerbervich, S.P. Baker and N. Burnham (Mater. Res. Soc. Symp. Proc. 552, Warrendale. P.A., 1998).

5. Fundamentals of nanoindentation and Nanotribology II, edited by S.P. Baker, R.F. Cook, S.G. Corcoran and N.R. Moody (Mater. Res. Soc. Symp. Proc. 649, Warrendale, P.A. 2001).

6. T.F. Page and S.J. Bull, Measuring and Modelling the Instrumented Indentation (Nanoindentation) Response of Coated Systems, Philosophical Magazine 86 (33- 35) (2006), 5331.

7. S. Bec, A. Tonck and J. Fontaine, Nanoindentation and nanofriction on DLC films, Philosophical Magazine 86 (33-35) (2006), 5465.

8. S. Chen, L. Liu and T. Wang, Investigation of the Mechanical Properties of Thin Films by Nanoindentation, Considering the Effects of Thickness and Different Coating –Substrate Combinations, Surf. & Coat. Tech. 191 (2005), 25.

9. S.H. Chen, L. Liu and T.C. Wang, Small Scale, Grain Size and Substrate Effects in Nano-Indentation Experiment of Film-Substrate Systems, Int. J. Solids & Structures 44 (2007), 4492.

10. T. Chudoba, M. Griepentrog, A. Duck, D. Schneider, F. Richter, Young's Modulus Measurements on Ultra-Thin Coatings, J. Mater. Res. 19 (1) (2004), 301.

11. G. Feng, A.H.W. Ngan, The Effect of Creep on Elastic Modulus Measurement using Nanoindentation, Mat. Res. Soc. Symp. Proc. Vol. 649 (2001), Q7.1.1.

12. G. Feng, A.H.W. Ngan, Effects of Creep and Thermal Drift on Modulus Measurement using Depth-Sensing Indentation, J. Mater. Res. 17 (3) (2002), 660.

13. C. Lukey, Thermoset Coatings, Encyclopaedia Sci. & Tech. (2001) 9209, Elsevier Sci.

14. Zeno W Wicks, Jr., Frank N. Jones and S. Peter Pappas, Organic Coatings Sci. & Tech. Vol. 1: Film Formation, Components, and Appearance, John Wiley & Sons (1992).

15. Zeno W Wicks, Jr., Frank N. Jones and S. Peter Pappas, Organic Coatings Sci. & Tech. Vol. 2: Applications, Properties, and Performance, John Wiley & Sons (1994).

16. Private communications, Bluescope Steel.

17. ASTM D3363-05: Standard Test Method for Film Hardness by Pencil Test. ICS number code 87.040 (paints and vanishes).

18. P. Betz, A. Bartelt, Scratch Resistant Clear Coats: Development of New Testing Methods for Improved Coatings, Progress in Organic Coatings 22 (1993), 27.

19. B.J. Briscoe, P.D. Evans, E. Pelillo, S.K. Sinha, Scratching Maps for Polymers, Wear 200 (1996), 137.

20. W. Shen, L. Mi, B. Jiang, Characterization of Mar/Scratch Resistance of Coatings with a Nano-indenter and a Scanning Probe Microscope, Tribology Int. 39 (2006), 146.

21. B.V. Gregorovich, I. Hazan, Environmental Etch Performance, and Scratch and Mar of Automotive Clearcoats, Prog. Org. Coat. 24 (1994), 131.

22. K.V.S.N. Raju, M Yaseen, Scratch Hardness of Paint Coatings: Effect of Ageing and Film Thickness, Prog. Org. Coat. 21 (1992), 37.

23. L. Lin, G.S. Blackman, R.R. Matheson, A New Approach to Characterize Scratch and Mar Resistance of Automotive Coatings, Prog. Org. Coat. 40 (2000), 85.

24. J. Lange, A. Luisier, A. Hult, Influence of Crosslink Density, Glass Transition Temperature and Additions of Pigment and Wax on the Scratch Resistance of an Epoxy Coating, J. Coatings Tech. 69, 872 (Sept. 1997), 77.

25. P. Bertrand-Lambotte, J. L. Loubet, C. Verpy, S. Pavan, Nano-indentation, Scratching and Atomic Force Microscopy for Evaluating the Mar Resistance of Automotive Clearcoats: Study of Ductile Scratches, Thin Solid Films 398-399 (2001), 306.

26. P. Bertrand-Lambotte, J. L. Loubet, C. Verpy, S. Pavan, Understanding of Automotive Clearcoats Scratch Resistance, Thin Solid Films, 420-421 (2002),

281.

27. S.V. Hainsworth, P.J. Kilgallon, Temperature-Variant Scratch Deformation Response of Automotive Paint Systems, Prog. Org. Coat. 62 (2008), 21.

28. ASTM D1044-78 (1998): Resistance of Transparent Plastics to Surface Abrasion.

29. H. Pelletier, C. Hendibide, A. Riche, Mechanical Characterization of Polymeric Films using Depth-Sensing Instrument: Correlation between Viscoelastic-Plastic Properties and Scratch Resistance, Prog. Org. Coat. 62 (2008), 162.

30. V. Jardret, H. Zahouani, J.L. Loubet, T.G. Mathia, Understanding and Quantification of Elastic and Plastic Deformation During a Scratch Test, Wear 218 (1998), 8.

31. K.L. Johnson, Contact Mechanics, Cambridge, New York: Cambridge University Press, 1985.

32. W.C. Oliver, G.M. Pharr, An Improved Technique for Determining Hardness and Elastic Modulus using Load and Displacement Sensing Indentation, J. Mater.Res.,7 (6) (1992), 1564.

33. W.C. Oliver, G.M. Pharr, Measurement of Hardness and Elastic Modulus by Instrumented Indentation: Advances in Understanding and Refinements to Methodology, J. Mater. Res., 19 (1) (2004), 3.

34. I.N. Sneddon, The Relation between Load and Penetration in the Axisymmetric Boussinesq Problem for a Punch of Arbitrary Profile, Int. J. Engng. Sci., 3 (1965), 47.

35. G.M. Pharr, A. Bolshakov, Understanding Nanoindentation Unloading Curves, J. Mater. Res., 17 (3) (2002), 2660.

36. M. Sakai, Elastic Recovery in the Unloading Process of Pyramidal Microindentation, J. Mater. Res., 18 (7) (2003), 1631.

37. M. F. Doerner, W.D. Nix, A Method for Interpreting the Data from Depth Sensing Indentation Instruments, J. Mater. Res. 1 (4), Jul/Aug (1986), 601.

38. G.M. Pharr, W.C. Oliver, F.R. Brotzen, On the Generality of the Relationship among Contact Stiffness, Contact Area, and Elastic Modulus during Indentation, J. Mater. Res., 7 (3) (1992), 613.

39. J.S. Field, M.V. Swain, A Simple Predictive Model for Spherical Indentation, J. Mater. Res. 8 (2) (1993), 297.

40. T.J. Bell, J.S. Field, M.V. Swain, Precision Hardness & Elastic Modulus Measurements of Thin Films & Cross-sections, Materials Forum (1993) 17, 127.

41. G. Kourtesis, G.M. Renwick, A.C. Fischer-Cripps, M.V. Swain, Mechanical Property Characterization of a Number of Polymers using Uniaxial Compression and Spherical Tipped Indentation Tests, J. Mater. Sci. 32 (1997), 4493.

42. A.C. Fischer-Cripps, A Review of Analysis Method for Sub-Micron Indentation Testing, Vacuum 58 (2000), 569.

43. J. Mencik, M.V. Swain, Errors Associated with Depth-Sensing Microindentation Tests, J. Mater. Res., 10 (6) (1995), 1491.

44. A.E. Giannakopoulos, Elastic and Viscoelastic Indentation of Flat Surfaces by Pyramid Indentation, J. Mechanics and Physics of Solids, 54 (2006), 1305.

45. P. Eaton, F.F. Estarlich, R.J. Ewen, T. G. Nevell, J.R. Smith, J. Tsibouklis, Combined Nanoindentation and Adhesion Force Mapping Using the Atomic Force Microscope: Investigations of a Filled Polysiloxane Coating, Langmuir,

18 (2002), 10011.

46. D. Tranchida, S. Piccarolo, Relating Morphology to Nanoscale Mechanical Properties: from Crystalline to Mesomorphic iPP, Polymer, 46 (2005), 4032.

47. D. Tranchida, S. Piccarolo, M. Soliman, Nanoscale Mechanical Characterization of Polymers by AFM Nanoindentations: Critical Approach to the Elastic Characterization, Macromolecules, 39 (2006), 4547.

48. H. Shulha, A. Kovalev, N. Myshkin, V.V. Tsukruk, Some Aspects of AFM Nanomechanical Probing of Surface Polymer Films, European Polymer J. , 40 (2004), 949.

49. B. Cappella, S.K. Kaliappan, H. Sturm, Using AFM Force-Distance Curves to Study the Glass-to-Rubber Transition of Amorphous Polymers and Their Elastic-Plastic Properties as a Function of Temperature, Macromolecules, 38 (2005), 1874.

50. T.-H. Fang, W.-J. Chang, S.-L. Tsai, Nanomechanical Characterization of Polymer using Atomic Force Microscopy and Nanoindentation, Microelectronics J., 36 (2005), 55.

51. D. Raghavan, X. Gu, T. Nguyen, M. VanLandingham, A. Karim, Mapping Polymer Heterogeneity Using Atomic Force Microscopy Phase Imaging and Nanoscale Indentation, Macromolecules, 33 (2000), 2573.

52. M.R. Vanlandingham, S.H. McKnight, G.R. Palmese, J.R. Elings, X. Huang, T.A. Bogetti, R.F. Eduljee, J.W. Gillespie Jr., Nanoscale Indentation of Polymer Systems Using the Atomic Force Microscope, J. Adhesion, 64 (1997), 31.

53. M.R. VanLandingham, R.R. Dagastine, R.F. Eduljee, R.L. McCullough, J.W. Gillespie Jr., Characterization of Nanoscale Property Variations in Polymer Composite Systems: 1. Experimental Results, Composites: Part A, 30 (1999), 75.

54. V.V. Tsukruk, V.V. Gorbunov, Z. Huang, S.A. Chizhik, Dynamic Microprobing of Viscoelastic Polymer Properties, Polym. Int., 49 (2000), 441.

55. S.A. Chizhik, V.V. Gorbunov, I. Luzinov, N. Fuchigami, V.V. Tsukruk, Surface Force Spectroscopy of Elastomeric Nanoscale Films, Macromol. Symp., 167 (2001), 167.

56. V.V. Tsukruk, Z. Huang, S.A. Chizhik, V.V. Gorbunov, Probing of Micromechanical Properties of Compliant Polymeric Materials, J. Mater. Sci., 33 (1998), 4905.

57. V.V. Tsukruk, A. Sidorenko, V.V. Gorbunov, S.A. Chizhik, Surface Nanomechanical Properties of Polymer Nanocomposite Layers, Langmuir , 17 (2001), 6715.

58. K.D. Yao, W.G. Liu, Z. Lin, X.H. Qiu, In Situ Atomic Force Microscopy Measurement of the Dynamic Variation in the Elastic Modulus of Swollen Chitosan/Gelatine Hybrid Polymer Network Gels in Media of Different pH, Polym. Int., 48 (1999), 794.

59. U.G. Hofmann, C. Rotsch, W.J. Parak, M. Radmacher, Investigating the Cytoskeleton of Chicken Cardiocytes with the Atomic Force Microscope, J. Structural Biology, 119 (1997), 84.

60. Jolanta A. Blach, Gregory S. Watson, W. Ken Busfield, Sverre Myhra, Photo-oxidation Degradation in Polyisoprene: surface Characterization and Analysis by Atomic Force Microscopy, Polymer Int. 51 (2001), 12.

61. C. Reynaud, F. Sommer, C. Quet, N. El Bounia, Tran Minh Duc, Quantitative Determination of Young's Modulus on a Biphase Polymer System using Atomic Force Microscopy, Surf. Interface Anal., 30 (2000), 185.

62. J. Xu, J. Hooker, I. Adhihetty, P. Padmanabhan, W. Chen, Characterization of

Mechanical Properties of Thin Polymer Films using Scanning Probe Microscopy, Mater. Res. Soc. Symposium Proceedings (1998), 552 (Fundamentals of Nanoindentation and Nanotribology), 217.

63. S.A. Chizhik, Z. Huang, V.V. Gorbunov, N.K. Myshkin, V.V. Tsukruk, Micromechanical Properties of Elastic Polymeric Materials As Probed by Scanning Force Microscopy, Langmuir 14 (1998), 2606.

64. K.L. Johnson, K.R. Kendall, A.D. Roberts, Surface Energy and the Contact of Elastic Solids, Proc. R. Soc. London A, 324 (1971), 301.

65. G.J.C. Braithwaite, P.F..Luckham, The Simultaneous Determination of the Forces and Viscoelastic Properties of Adsorbed Polymer Layers, J. Colloid & Interface Sci., 218 (1999), 97.

66. P.M. McGuiggan, D.J. Yarusso, Measurement of the Loss Tangent of a Thin Polymeric Film using the Atomic Force Microscope, J. Mater. Res., 19 (1) (2004), 387.

67. C. Basire, C. Fretigny, Determination of Viscoelastic Moduli at a Submicrometric Scale, Eur. Phys. J. AP, 6 (1999), 323.

68. C. Fretigny, C. Basire, V. Granier, Determination of Complex Modulus by Atomic Force Microscopy, J. Appl. Phys. 82 (1) (1997), 43.

69. E. Gacoin, A. Chateauminois, C. Fretigny, Measurements of the Viscoelastic Moduli of an Acrylate Polymer in Bulk and Film Form using a Contact Method, Polymer, 45 (2004), 3789.

70. T.C. Ovaert, B.R. Kim, J. Wang, Multi-Parameter Models of the Viscoelastic/Plastic Mechanical Properties of Coatings via Combined Nanoindentation and Non-Linear Finite Element Modeling, Prog, Org. Coatings, 47 (2003), 312.

71. H. Lu, B. Wang, J. Ma, G. Huang, H. Viswanathan, Measurement of Creep Compliance of Solid Polymers by Nanoindentation, Mechanics of Time-Dependent Mater., 7 (2003), 189.

72. C.Y. Zhang, Y.W. Zhang, K.Y. Zeng, L. Shen, Nanoindentation of Polymers with a Sharp Indenter, J. Mater. Res., 20 (6) (2005), 1597.

73. C.Y. Zhang, Y.W. Zhang, K.Y. Zeng, Extracting the Mechanical Properties of a Viscoelastic Polymeric Film on a Hard Elastic Substrate, J. Mater. Res., 19 (10) (2004), 3053.

74. M.L. Oyen, R.F. Cook, J.A. Emerson, N.R. Moody, Indentation Responses of Time-Dependent Films on Stiff Substrates, J. Mater. Res., 19 (8) (2004), 2487.

75. P.-L. Larsson, S. Carlsson, Data Interpretation on Microindentation of Viscoelastic Polymers, Polym. Testing, 17 (1998), 49.

76. C.Y. Zhang, Y.W. Zhang, K.Y. Zeng, L. Shen, Characterization of Mechanical Properties of Polymers by Nanoindentation Tests, Philosophical Magazine, 86 (2006), 4487.

77. C.-K. Liu, S. Lee, L.-P. Sung, T. Nguyen, Load-Displacement Relations for Nanoindentation of Viscoelastic Materials, J. App. Physics, 100 (2006), 033503.

78. M.L. Oyen, Analytical Techniques for Indentation of Viscoelastic Materials, Philosophical Magazine, 86 (33-35) (2006), 5625.

79. L. Cheng, X, Xia, L.E. Scriven, W.W. Gerberich, Spherical-Tip Indentation of Viscoelastic Material, Mechanics of Materials, 37 (2005), 213.

80. L. Anand, N.M. Ames, On Modelling the Micro-Indentation Response of an Amorphous Polymer, Int. J. Plasticity, 22 (2006), 1123.

81. A. Sadr, Y. Shimada, H. Lu, J. Tagami, The Viscoelastic Behaviour of Dental

Adhesives: A Nanoindentation Study, Dental Materials, 25 (2009), 13.

82. G. Yang, N. Rao, Z. Yin, D.-M. Zhu, Probing the Viscoelastic Response of Glassy Polymer Films using Atomic Force Microscopy, J. Colloid & Interface Sci., 297 (2006), 104.

83. A.C. Fischer-Cripps, A Simple Phenomenological Approach to Nanoindentation Creep, Mater. Sci. & Eng. A, 385 (2004), 74.

84. S. Yang, Y.-W. Zhang, K. Zeng, Analysis of Nanoindentation Creep for Polymeric Materials, J. Appl. Phys., 95 (7) (2004), 3655.

85. M.L. Oyen, R. F. Cook, Load-displacement Behaviour during Sharp Indentation of Viscous-Elastic-Plastic Materials, J. Mater. Res., 18 (1) (2003), 139.

86. Joel R. Fried, Polymer Sci. & Tech., Prentice Hall PTR (2003), NJ.

87. A. Krupicka, M. Johansson, A. Hult, Viscoelasticity in Polymer Films on Rigid Substrates, Macromol. Mater. Eng., 288 (2003), 108.

88. S. T. Choi, S. R. Lee, Y. Y. Earmme, Flat Indentation of a Viscoelastic Polymer Film on a Rigid Substrate, Acta Materialia, 56 (2008), 5377.

89. L. Shen, W.C. Tjiu, T. Liu, Nanoindentation and Morphological Studies on Injection-molded Nylon-6 Nanocmposites, Polym, 46 (2005), 11969.

90. J.L. Loubet, W.C. Oliver, B.N. Lucas, Measurement of the Loss Tangent of Low-Density Polyethylene with a Nanoindentation Technique, J. Mater. Res., 15 (5) (2000), 1195.

91. P.J. Wei, W.X. Shen, J.F. Lin, Analysis and Modeling for Time-Dependent Behavior of Polymers Exhited in Nanoindentation Tests, J. Non-Crystalline Solids, 354 (2008), 3911.

92. S.N. Dub, M.L. Trunov, Determination of Viscoelastic Material Parameters by Step-loading Nanoindentation, J. Phy.s D: Appl. Phys., 41 (2008), 074024.

93. J.L. Gilbert, I. Merkhan, Rate Effects on the Microindentation-based Mechanical Properties of Oxidised, Crosslinked, and Highly Crystalline Ultrahigh-Molecular-Weight Polyethylene, J. Biomed. Mater. Res. A, 71A (3) (2004), 549.

94. W.N. Findley, J.S. Lai and K. Onaran, Creep and Relaxation of Nonlinear Viscoelastic Materials (Dover, New York, 1975).

95. M Sakai, S. Shimizu, Indentation Rheometry for Glass-Forming Materials, J. Non-Crystalline Solids, 282 (2001), 236.

96. S. Shimizu, T. Yanagimoto, M. Sakai, Pyramidal Indentation Load-Depth Curve of Viscoelastic Materials, J. Mat. Res., 14, (10) (1999), 4075.

97. T. Chudoba, F. Richter, Investigation of Creep Behaviour under Load during Indentation Experiments and its Influence on Hardness and Modulus Results, Surf. & Coat. Tech., 148 (2001), 191.

98. T. Chudoba, N. Schwarzer, F. Richter, Determination of Elastic Properties of Thin Films by Indentation Measurements with a Spherical Indenter, Surface & Coating Tech., 127 (2000), 9.

99. J. Malzbender, J.M.J. den Tooner, A.R. Balkenende, G. de With, Measuring Mechanical Properties of Coatings: a Methodology Applied to Nano-Particle-Filled Sol-Gel Coatings on Glass, Mater. Sci. & Eng. R, 36 (2002), 47.

100. H. Lu, G. Huang, B. Wang, A. Mamedov, S. Gupta, Characterization of the Linear Viscoelastic Behavior of Single-Wall Carbon Nanotube/Polyelectrolyte Multilayer Nanocomposite Film using Nanoindentation, Thin Solid Films, 500 (2006), 197.

101. G. Toikka, G M. Spinks, H.R. Brown, Fine Particle Adhesion Measured at

Elevated Temperatures Using a Dedicated Force Rig, Langmuir, 17 (2001), 6207.

102. J.P. Cleveland, S. Manne, D. Bocek, P.K. Hansma, A Nondestructive Method for Determining the Spring Constant of Cantilevers for Scanning Force Microscopy, Rev. Sci. Instrum., 64 (2) (1993), 403.

103. Siu W. Wai, Geoffrey M. Spinks, Hugh R. Brown, Michael Swain, Surface Roughness: Its Implications and Inference with regards to Ultra Microindentation Measurements of Polymer Mechanical Properties, Polymer Testing 23 (2004), 501.

104. J. Brandrup, E.H. Immergut, E.A. Grulke, Polymer Handbook, Wiley, New York, 1999.

105. Christian Perruchot, John F. Watts, Chris Lowe, Graham Beamson, Characterisation of the Curing Temperature Effects on Polyester Systems by Angle-Resolved XPS (ARXPS), Int. J. Adhesion & Adhesives, 23 (2003), 101.

106. J.F. Rudd, E.F. Gurnec, Photoelastic Properties of Polystyrene in the Glassy State. II. Effect of Temperature, J. Appl. Phys, 28, 10 (1957), 1096.